University of Ferrara
Physics and Earth Science Department

Ph.D. in Physics

Low-operating temperature chemiresistive gas sensors: Fabrication and DFT calculations

Candidate
Krik Soufiane

Supervisor
Prof. Guidi Vincenzo

External supervisor
Ph.D. Gaiardo Andrea

Ph.D. Coordinator
Prof. Luppi Eleonora

XXXIII Cycle – 2017/2021
Scientific/Disciplinary Sector (SDS): FIS/01

This page intentionally left blank

Abstract

Despite advantages highlighted by Metal OXides (MOX) based gas sensors, these devices still show drawbacks in their performances (e.g. selectivity, stability and high operating temperature), so further investigations are necessary. Researchers tried to address these problems in several ways, which includes new synthesis methods for innovative materials based on MOX, such as solid solutions (WO_3-SnO_2, SnO_2-TiO_2), addition of catalysts (Pd, Au, Pt etc.) and doping of MOX by using external atoms or oxygen vacancies. Concerning this last issue, literature presents a lack of studies on how arrangement and number of oxygen vacancies affect the sensing performance and only a few preliminary works highlighted interesting results. Another way to overcome MOX sensor drawbacks is to investigate other kinds of materials, such as metal organic framework or 2D materials, which recently highlighted interesting results. Among the various 2D materials, phosphorene is one of the best candidates for such technological application, since it shows a chemoresistive activity at room temperature.

The purpose of this thesis work was focused on the study of materials addressed to gas sensing application operating at low temperatures, both tuning electrical properties of a well-known metal oxides, i.e. tin oxide (SnO_2), through a control of oxygen vacancies, and investigating a promising 2D material, i.e. black phosphorus.

In the wide palette of MOX, SnO_2 represented the best candidate for the innovative work here proposed since it is the most studied semiconductor for chemiresistive gas sensors production. The goal is to decrease its operating temperature by exploiting the oxygen vacancies. First, a theoretical investigation was done in the framework of Density Functional Theory (DFT) in order to investigate, on the atomic scale, how oxygen vacancies influence the physical and chemical properties of the material. The effect of oxygen vacancies on the structural, electronic and electrical properties of bulk SnO_2 at two different concentrations was studied, then the formation of surface oxygen vacancies was investigated in order to study the adsorption of oxygen molecules from the surrounding atmosphere on the stoichiometric and reduced SnO_2 surface. Then, reduced SnO_{2-x} was synthesized and devices based on the produced material were fabricated and tested. The results showed a high response of the sensors towards low concentrations of nitrogen dioxide NO_2 (500 ppb) at 130 °C instead of 450 °C, the operating temperature of the available SnO_2-based gas sensors. This decrease in the operating temperature produces a decrease in the power consumption of the device, opening up to its possible employment on portable devices like mobile phones. The results were interpreted characterizing the material by mean of X-ray Powder Diffraction (XRD), X-ray Photoelectron Spectroscopy (XPS), Scanning Electron Microscope (SEM) and Ultraviolet–visible spectroscopy (UV-visible) analysis. In the end, the experimental results were compared to the DFT outputs obtained.

As mentioned before, phosphorene is one of the promising 2D materials for gas sensing applications, but it still presents some drawbacks, mainly due to the material degradation over the time. Many investigations were done on decorating phosphorene with metal atoms in order to enhance its performance for different technological applications. Nickel is one of metals proposed for such purpose, but few studies were done on nickel decorated phosphorene for gas sensing applications, especially for gas sensing application. In the innovative work here proposed, DFT calculations were carried out to explain how nickel influences the electronic properties of phosphorene since the decoration with nickel showed better stability of the sensor and high response towards NO_2 at room temperature. The theoretical results explained this behavior by studying the adsorption of oxygen molecules on pristine and nickel loaded phosphorene. The DFT calculations showed that oxygen molecules dissociate on the layer of pristine phosphorene and react with phosphorus atoms (oxidation of the material), while in the presence of the nickel atoms the later play the role of acceptors and interact with the oxygen molecules. Finally, the sensing mechanism towards NO_2 was investigated theoretically by studying the charge transfer occurring at the surface of the material during the adsorption process.

Activity report & list of publications and contributions

The research activity carried out by the PhD student involved all the key aspects regarding the study and the realization of solid-state devices for gas sensing. The work was focused, on one hand, on the production of chemoresistive gas sensors based on reduced Tin dioxide (SnO_2)-based devices for low operating temperature operations and on DFT calculations to deeply understand how oxygen vacancies influence the electronic properties of SnO_2-based gas sensors. On the other hand, a DFT investigation was carried out concerning the possible and innovative use of nickel decorated phosphorene for stable and room temperature NO_2 detection. The influence of nickel on the electronic structure of phosphorene was investigated demonstrating the stability of the material in presence of oxygen molecules and the sensing mechanism towards NO_2 was studied theoretically by means of DFT. In parallel with the work presented in this thesis some other projects have been followed. In particular, during the last two years of the PhD course the candidate participated in the study of sensors with high sensitivity to specific substances and the fabrication and electrical characterization of many type of Metal OXide (MOX)-based gas sensors in the framework of a collaboration between inspection systems division of Sacmi and Sensors Lab of the Department of Physics and Earth Sciences. Articles and proceeding published/under publication during the PhD alongside with national and international conference contributions are listed as follows.

JOURNALS

- Soufiane Krik, Andrea Gaiardo, Matteo Valt, Barbara Fabbri, Cesare Malagù, Giancarlo Pepponi, Pierluigi Bellutti and Vincenzo Guidi. (2021). First-Principles Study of Electronic Conductivity, Structural and Electronic Properties of Oxygen-Vacancy-Defected SnO_2. *Journal of Nanoscience and Nanotechnology*, *21*(4), 2633-2640. https://doi.org/10.1166/jnn.2021.19116
- E. Spagnoli, S. Krik, B. Fabbri, M. Valt, A. Gaiardo, M. Ardit, M. Della Ciana, V. Cristino, S. Caramori, C. Malagù, V. Guidi. (2021). Development and characterization of WO_3 nanoflakes for selective ethanol sensing. Submitted to *Sensors and Actuators, B: Chemical*
- M. Valt, M. Caporali, B. Fabbri, A. Gaiardo, S. Krik, E. Iacob, L. Vanzetti, C. Malagù, M. Serrano-Ruiz, M. Peruzzini and V. Guidi. (2021). Air stable nickel-decorated black phosphorus and its room-temperature chemoresistive gas sensor capabilities. Under submission to *Applied materials and interfaces*
- A. Gaiardo, E. Spagnoli, B. Fabbri, M. Valt, S. Krik, M. Ardit, G. Cruciani) M. Della Ciana, L. Vanzetti, C. Malagù, P. Bellutti, V. Guidi. (2021). $SnTiNbO_x$ chemoresistive gas sensors: influence of the Nb concentration and calcination temperature on the detection of H_2. Under submission to *ACS sensors*

CONFERENCE PROCEEDINGS

- S. Krik, A. Gaiardo, M. Valt, B. Fabbri, C. Malagù, P. Bellutti, V. Guidi, Influence of Oxygen Vacancies in Gas Sensors Based on Tin Dioxide Nanostructure: A First Principles Study, Proceedings 2019, 14(1), 14, https://doi.org/10.3390/proceedings2019014014

- Z. Essalhi, S. Krik, B. Hartiti, A. Gaiardo, A. Lfakir, M. Valt, S. Fadili, B. Fabbri, M. Siadat, V. Guidi, P. Thevenin, Elaboration and Characterization of SnO2 Doped TiO2 Gas Sensors Deposited through Dip and Spin Coating Methods, Proceedings 2019, 14(1), 23, https://doi.org/10.3390/proceedings2019014023
- Soufiane Krik, Andrea Gaiardo, Matteo Valt, Barbara Fabbri, Cesare Malagù, Giancarlo Pepponi, Davide Casotti, Giuseppe Cruciani, Vincenzo Guidi and Pierluigi Bellutti. (2019) Influence of Oxygen Vacancies in Gas Sensors Based on Metal-Oxide Semiconductors: A First-Principles Study. *Sensors and Microsystems, Lecture Notes in Electrical Engineering* 629. https://doi.org/10.1007/978-3-030-37558-4_47
- Andrea Gaiardo, Nadhira Laidani, Hafeez Ullah, Giancarlo Pepponi, Michele Fedrizzi, Vincenzo Guidi, Pierluigi Bellutti, Barbara Fabbri, Cesare Malagù, Giulia Zonta, Nicolò Landini, Soufiane Krik, Ruben Bartali, Francesca Marchetti and Matteo Valt. (2018) A New Method to Prepare Few-Layers of Nanoclusters Decorated Graphene: Nb_2O_5/Graphene and Its Gas Sensing Properties. *Eurosensors-2018* Conference, Graz, Austria. https://doi.org/10.3390/proceedings2131047

ORAL PRESENTATIONS

- Soufiane Krik, Andrea Gaiardo, Matteo Valt, Barbara Fabbri, Cesare Malagù, Pierluigi Bellutti and Vincenzo Guidi. Adsorption of oxygen species on the SnO_2 (110) surface: a Density Functional Theory investigation. Regular talk in the *37th International Symposium on Dynamical Properties of Solids* -DyProSo 2019. 8-12 September 2019
- Soufiane Krik, Andrea Gaiardo, Matteo Valt, Barbara Fabbri, Cesare Malagù, Giancarlo Pepponi, Davide Casotti, Giuseppe Cruciani, Vincenzo Guidi and Pierluigi Bellutti. Influence of Oxygen Vacancies in Gas Sensors Based on Metal-Oxide Semiconductors: A First-Principles Study. The *20th Italian Association of Sensors and Microsystems* -AISEM 2019. 11,12,13 February 2019
- Soufiane Krik, Andrea Gaiardo, Matteo Valt, Barbara Fabbri, Cesare Malagù, Giancarlo Pepponi, Pierluigi Bellutti, Vincenzo Guidi. (2021). First Principles Study on Surface Oxygen Vacancies for Highly Sensitive and Low Operating Temperature SnO_2 Gas Sensors. *The 239th ECS Meeting with the 18th International Meeting on Chemical Sensors*- IMCS 2021. May 30-June 3, 2021 | Digital Meeting. (Speaker: Soufiane krik)
- A. Gaiardo, S. Krik, M. Valt, B. Fabbri, M. Tonezzer, Z. Feng, V. Guidi, and P. Bellutti. (2021). Development of a Sensor Array Based on Pt, Pd, Ag and Au Nanocluster Decorated SnO_2 for Precision Agriculture. *The 239th ECS Meeting with the 18th International Meeting on Chemical Sensors*- IMCS 2021. May 30-June 3, 2021 | Digital Meeting (Speaker: Andrea Gaiardo)
- E. Spagnoli, M. Valt, B. Fabbri, M. Ardit, V. Cristino, M. Della Ciana, A. Gaiardo, S. Krik, G. Zonta, S. Caramori, C. Malagù, and V. Guidi. (2021). WO_3 Nanoparticles and Nanoflakes Based Sensors for Selective Detection of Alcohols. *The 239th ECS Meeting with the 18th International Meeting on Chemical Sensors*- IMCS 2021. May 30-June 3, 2021 | Digital Meeting (speaker: Elena spagnoli)
- Z. Feng, A. Gaiardo, S. Krik, V. Guidi, G. Pepponi, C. Malagù, P. Bellutti, B. Fabbri, M. Valt, and S. Caramori. (2021). Gas Sensing Properties Comparison between SnO_2 and Highly Antimony-Doped SnO_2 materials. *The 239th ECS Meeting with the 18th International Meeting on Chemical Sensors*- IMCS 2021. May 30-June 3, 2021 | Digital Meeting (speaker: zhifu feng)

POSTERS PRESENTATIONS

- Soufiane Krik, Andrea Gaiardo, Matteo Valt, Barbara Fabbri, Cesare Malagù, Giancarlo Pepponi, Pierluigi Bellutti and Vincenzo Guidi. DFT simulations of

materials used as sensing elements for chemoresestive gas sensors. *4th edition of FBK PhD day 2020*. February 21st, 2020

- Soufiane Krik, Andrea Gaiardo, Matteo Valt, Barbara Fabbri, Cesare Malagù, Pierluigi Bellutti and Vincenzo Guidi. Influence of Oxygen Vacancies in Gas Sensors Based on Tin Dioxide Nanostructure: A First-Principles Study. *The 8th GOSPEL Workshop*, 20–21 June 2019. https://doi.org/10.3390/proceedings2019014014
- Zineb Essalhi, Soufiane Krik, Bouchaib Hartiti, Andrea Gaiardo, Abderrazak Lfakir, Matteo Valt, Salah Fadili, Barbara Fabbri, Maryam Siadat, Vincenzo Guidi and Philippe Thevenin. Elaboration and Characterization of SnO2 Doped TiO2 Gas Sensors Deposited through Dip and Spin Coating Methods. The 8th GOSPEL Workshop, 20–21 June 2019. https://doi.org/10.3390/proceedings2019014023

This page intentionally left blank

Table of contents

This page intentionally left blank

Introduction

Present concerns of the environment protection focus on air quality in industries, cities and houses, especially from a pollution point of view [1]. As a result, the field of gas sensors for highly hazardous compounds is an important area of research for health and safety applications. Despite the fact that the current economy has an effect on the statistics, there are numerous applications for gas sensors, of which a few are mentioned [2, 3, 4, 5, 6, 7, 8, 9, 10, 11]:

- Environmental: pollution levels in urban areas, high-traffic public places, and enclosed habitats are detected (basements, parking lots, clean rooms, and aerospace).
- Domestic: carbon monoxide and methane leak detection (gas boilers), butane leak detection (gas cylinders), smoke detection, and so on.
- Industrial: toxic solvent vapor detection (chloroform, acetone, hexane, etc.) or explosive gas detection (hydrogen, propane).
- Research: gas level regulation and monitoring in fields such as hydrogen for energy storage, solvents in chemistry, hydrocarbons in biology, and carbon dioxide, ozone, and fine exhaust particle detection in the atmosphere.
- Automotive: breathalyzer, cabin air quality monitoring, catalytic converter detection, hydrogen battery leak sensors.
- Military: identification of toxic gases like carbon monoxide, phosgene and sarin.

This is not an exhaustive list of applications, but it demonstrates the critical need for a reliable detection technology. The strong desire to maintain a good air quality leads to the establishment of observation networks that monitor and measure the most plentiful polluting and dangerous gases in the atmosphere like nitrogen oxides (NOx), carbon monoxide (CO), and ozone (O_3). These devices, which are basically made up of single sensors or gas sensor arrays, are specifically designed for these applications. The gas sensing field is not immune to the general tendency of device miniaturization and enhancement in sensing capacity.

Metal-oxide semiconductors (MOXS) are the most studied among the various materials used in the field of chemoresistive gas sensors due to their excellent sensitivity, good stability, and low production cost [12]. Despite the significant advantages highlighted by sensors based on this type of materials, these devices still have performance drawbacks (e.g., lack of selectivity, stability, and high operating temperature), highlighting the need for additional research.

Understanding the fundamentals of the reactions and processes that take place on the surface of the sensing material of MOXS-based gas sensors would improve their macroscopic

properties for many applications, particularly in terms of sensitivity and selectivity. The provision of atomic-scale information and design guidance will aid in the optimization of sensors for specific applications. Some advanced atomic-scale experimental characterizations can be carried out, but they do not provide a comprehensive explanation of the microscopic multi-step process taking place in a reaction, because they only provide information on the initial reactants and final products.

Atomic scale calculations based on first principles of Density Functional Theory (DFT) can aid in understanding fundamental mechanisms involved in chemical sensing. DFT calculations are valuable and emerging as versatile tools in the research and development process as computers performance enhance and the accuracy and reliability of electronic structure theory and computational approaches improve. DFT is an effective approach to understand the fundamentals of the interaction between gas molecules and the material surface in gas sensor applications, particularly when it comes to describe changes in geometric and electronic structures in the sensing layers during the interaction with the target gas. Nonetheless, the complex relationship between active sites at the surface, gas molecules and the sensing response results in a difficult interpretation of the atomic scale chemical reaction occurring in the surface of the sensing layer. The structure of the sensing material in terms of crystallography and defects, as well as the presence of various species such as humidity in the atmosphere, must be considered. More specifically, DFT calculations are used to provide a comprehensive description of the atomic-scale chemical reactions taking place on the surface of the sensing film and to investigate the associated changes in the electronic structure of the MOX film. The following information can be investigated by exploiting DFT calculation: the study of bond formation and breaking, determining the stability of the adsorbed species even in the presence of a multi-step reaction, the possible interaction of several adsorbed species, the determination of the interaction energies between the gas molecule and the surface, the determination of adsorption energies, the influence of crystallography and surface topology, the influence of pre-existing surface defects on adsorption energies, activation barrier calculations in adsorption and surface recombination, charge transfer investigation. More specific issues, such as the effect of doping or humidity on sensing performance, can be addressed. DFT can also be used to obtain other properties that can be compared to experimental results, such as spectroscopic data (infrared spectroscopy and x-ray photoelectron spectroscopy), aiding to correlate simulation with experimental results. Nonetheless, DFT calculations cannot describe a realistic detection of a gas molecule because they do not account for the effect of temperature or the competitive dynamic behavior of gas molecules. As a result, developing methods to predict sensor response and control chemical reactions at the nanoscale can aid in the advancement of the detection process of a MOX gas sensor.

The first main axis of this thesis was focused on a theoretical investigation on how oxygen vacancies influence the physical chemical properties of a widely studied material, i.e. SnO_2, and how they can enhance adsorption processes occurring on its surface. Afterwards, synthesis and material characterizations of reduced SnO_2 were performed in order to lower its operating temperature and then the power consumption of the final device. In this part of the work, the sensing performance of the devices produced were also investigated.

The second axis was concentrated on the decoration of monolayer black phosphorus with nickel, first principles calculations were carried out to study the influence of nickel on the properties of monolayer black phosphorus, based on experimental observations that showed good performance of nickel loaded phosphorene as NO_2 gas sensor. Indeed, the produced device showed a fast and stable response over the time towards NO_2 at room temperature and non-degradable material [13].

In the first chapter, it is provided an introduction to the generalities of semiconducting inorganic materials, including the main charge transport methods currently known and a description of their operation principles, as well as the main factors influencing their performance. Furthermore, the limitations of MOXS as chemoresistive gas sensing materials are discussed.

In the second chapter, it is presented an overview on the development of the DFT and on the methods used for computations in this work as well as the codes employed.

In the third chapter, DFT was used to calculate the physico-chemical properties of the three models of reduced SnO_2 in order to study the impact of oxygen vacancies on these properties.

The chapter four is focused on the experimental investigation of the oxygen vacancies influence on the SnO_2 sensing properties. A simple and low-cost sol-gel method was used to synthesize nanostructured SnO_2, and several thermal treatments to reduce the samples synthesized were carried out. In addition, the experimental characterizations of the obtained samples were compared to the theoretical results obtained using DFT.

In chapter five, an investigation on the interactions occurring between the SnO_2 surface and the oxygen molecules from the surrounding atmosphere was done. In addition, the formation of surface oxygen vacancies and then a study of the interaction between the reduced surface and oxygen molecules were carried out.

In the sixth chapter, the results obtained for nickel-decorated phosphorene are reported. It is explained how nickel enhances the sensing performance of monolayer black phosphorus and also a possible explanation of the stability of the material is proposed, as well as investigating the charge transfer occurring on its surface the sensing mechanism proposed by our group based on experimental outputs was confirmed.

Lastly, the principal conclusions of every study carried out in this PhD thesis work are reported.

This page intentionally left blank

This page intentionally left blank

1. Overview on gas sensors and semiconductors

1.1. Gas sensors

In recent years, environmental pollution has been identified as a major public health problem. And because it is the result of human activities, legislators are increasingly imposing and tightening laws in order to minimize its adverse health effects.

Within the European framework, and for local authorities, control instruments have been put in place. In the industrial sector, the control of liquid and gaseous emissions must be ensured. Among these controls, the detection of gaseous species is an essential issue.

Indeed, several techniques can be used to highlight reactions related to the detection of gaseous species, such as electrical measurements, spectroscopic or chromatographic techniques. Techniques based on spectroscopy and chromatography can show the formation or disappearance of gaseous species, whereas those based on electrical measurements are not able to do so. However, for sensor design, electrical measurement devices can be easily integrated into "embedded" systems, whereas spectroscopic measurement devices require more equipment or the use of more expensive technologies. This also illustrates the complexity of the choice of the analysis system, as the measurement means depend on the quantity to be studied. Thus, there exist several large families of gas sensors depending on the type of measurements carried out. These families include electrochemical sensors, sensors based on catalytic combustion and semiconductor sensors with resistance variation. A summary of the characteristics of the different types of detectors is presented in table I.1 [7].

Table I. 1: Comparative study of the characteristics of the major families of sensors [14]

Parameter	Type of gas sensors				
	Semi-conductor	Catalytic combustion	Electro-chemical	Thermal conductive	Infrared absorption
Sensitivity	e	g	g	b	e
Accuracy	g	g	g	g	e
Selectivity	p	b	g	b	e
Response time	e	g	p	g	p
Stability	g	g	b	g	g
Durability	g	g	p	g	e

Maintenance	e	e	g	g	p
Cost	e	e	g	g	p
Suitability to portable instruments	e	g	p	g	b

e: excellent; g: good; p: poor; b: bad.

From Table I.1, it can be concluded that there is no miraculous material to obtain an ideal detector, so necessary compromises to optimize performance must be made. It can be also seen that semiconductor-based detectors have many advantages than other types of detectors. They have a high sensitivity for one of the shortest response times, they are economical and their miniaturization, especially in the field of electronics, allows them to be easily integrated into a complete detection system.

Gas detection was first introduced in the 1960s by Japanese researchers Seiyama [15] and Taguchi [16]. Seiyam et al. studied the change in electrical resistance of ZnO for the detection of reducing gases. Taguchi et al. manufactured the first SnO_2 gas sensor from porous ceramic. Since then, research in the field of gas detection has been developed considerably.

As previously mentioned, several gas analysis techniques are well known and mastered, such as gas chromatography and mass spectrometry [17, 18, 19].

- Gas chromatography: the principle of gas chromatography is based on the separation of a gas mixture via a column. Two phases are involved in this process: the stationary phase and the mobile phase. The components to be analyzed must be soluble in the mobile phase on the one hand and have an affinity for the stationary phase on the other hand, in order to establish a physico-chemical balance. This method allows to measure the quantity of each component present in a gas mixture.
- Mass spectrometry: this is a method widely used in chemical analysis. Under the influence of a magnetic or electric field, it allows a quantitative and qualitative analysis of a gas mixture by bombardment of electrons, ions or photons. Depending on the mass/charge ratio, the identification of the gas is carried out. This analysis is very sensitive and applies to almost all gases with the exception of highly reactive or unstable gases.

These techniques allow a complete and accurate analysis, but they have the disadvantage of being relatively expensive and cumbersome.

Along with these two classical methods, many gas sensors based on chemical or physical principles were developed. Among those based on chemical principles chemeresistive devices that can be based on different kind of materials including MOXS can be listed. These devices showed compatibility with microelectronic technology on the one hand and have many advantages over other methods on the other hand. These advantages lie in their low cost, low power consumption and relatively short response time. This section attempts to identify the status of gas sensors, especially chemical sensors, in gas detection today.

1.1.1. Chemiresistive gas sensor

A chemiresistive gas sensor is a device that transduces modifications in the chemical conditions of the environment into a change in electrical conduction. It is a system able to react in the presence of a gas by changing one or more of its easily measurable properties such as surface conductivity, spectroscopic absorption… etc. The response is therefore due to a chemical interaction between a target gas (adsorbate) and the sensor surface (adsorbent), which results in a change in the physical and/or chemical properties of the sensitive layer.

In general, a gas sensor consists of a receptor and a transducer [20]. The first is composed of a material which, upon interaction with a target gas, induces a change in its properties (electrical conductivity, work function…etc.). The transducer is a device that transform this into an electrical signal (sensor response). Initially, the host material of the sensor receives and reacts with the gas (Figure I. 1). The information resulting from the interaction between the material and the gas will be then transduced into electrical signal. Then, the reception and analysis of the information will be performed using a specific measuring system (Figure I. 1) [4].

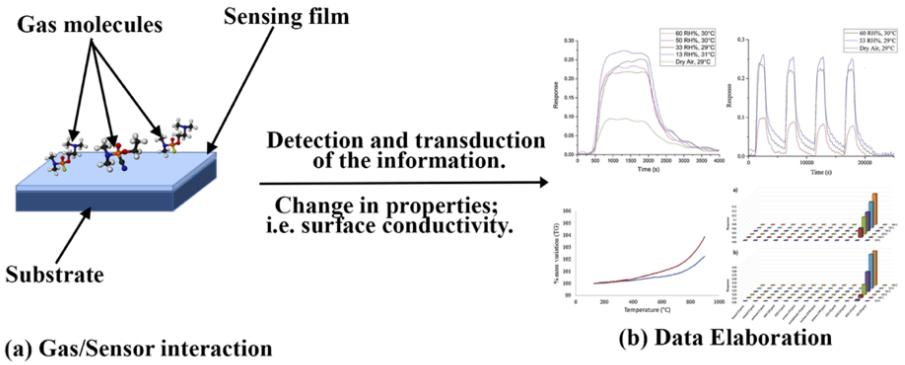

Figure I. 1: Representative diagram of the different stages of gas detection, reprinted with permission from [3].

1.1.2. Sensing performance of chemoresistive gas sensors

The sensitivity, selectivity, stability, repeatability, Limit Of Detection (LOD) and response/recovery time are the essential parameters, among other characteristic quantities describing the performance of a sensor.

Sensitivity is the change in the measured quantity caused by a change in gas concentration. It is defined by the following relationship:

$$Sensitivity\ (X)_p = \left|\frac{\Delta X}{\Delta C}\right|_p \qquad \text{Eq. I. 1}$$

where X is the measured variable (e.g. R for resistance, G for conductance, U for voltage, I for electric current or ϕ for light intensity), C is the gas concentration for a set of parameters p (temperature, pressure, humidity).

In many scientific papers, the term sensitivity is unproperly used to discuss the sensing response, which is the most widely used quantity to investigate the sensing performance of a gas sensor. Indeed, the sensitivity is the slope of the derivative of the calibration curve while the relative response corresponds to the ratio between the quantities measured in air (R_{air}, G_{air}, U_{air}) and in the presence of gas (R_{gas}, G_{air}, U_{gas}). Its expressions are summarized in Figure I. 2 for both cases of oxidizing and reducing gases and for n and p types semiconductors.

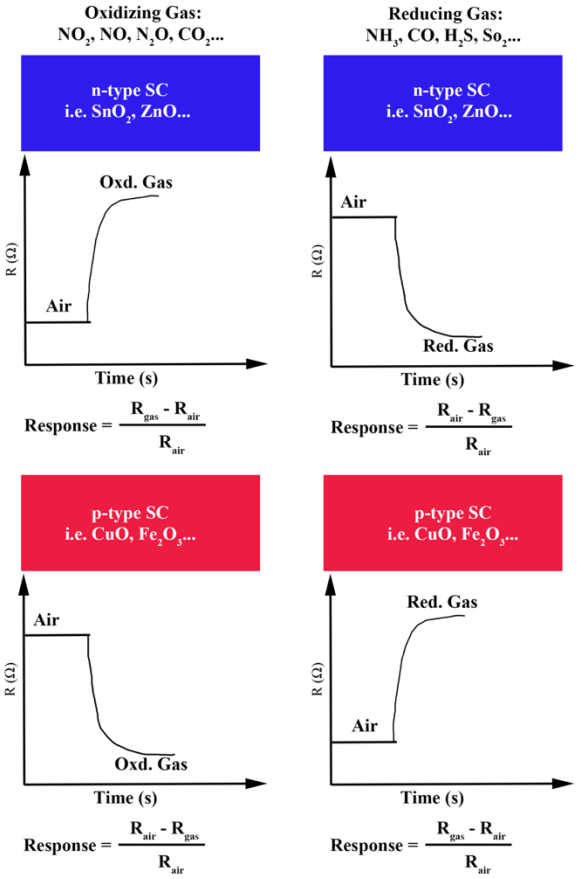

Figure I. 2 expressions of relative response for both cases of oxidizing and reducing gases and for n and p types semiconductors.

The sensor is most sensitive because a slight change in the gas concentration will result in a significant change in the measured resistance. Sensitivity (or relative response) is one of the strengths of metal-oxide sensors whose change in resistance can be measured for concentrations between *ppm* (parts per million) and one hundred *ppb* (parts per billion) [21].

The *selectivity* allow discrimination of a target gas within a gas mixture. It is defined as the ratio of the sensitivities (or relative responses) between two gases for the same concentration:

$$Selectivity_{gas1/gas2} = \frac{Response_{relative(gas1)}}{Response_{relative(gas2)}} \quad \text{Eq. I. 2}$$

The selectivity of metal-oxide sensors appears to be their weak point. In fact, they appear to have small selectivity to some particular gas unless they are treated by semiconductor doping.

The *repeatability*: under identical conditions measured at different times the sensor should give the same response for the same value of stimulus.

The *Limit Of Detection* (LOD): values above the LOD indicate the presence of an analyte, whereas values below the LOD indicate the no analyte is detectable.

Another critical parameter of a sensor is its *response time*, which is the time it takes for the sensor to respond to the presence of a gas.

Conversely, the response time following the removal of the gas is called the *recovery time*. In practice, these characteristic times are weighted by a factor of 0.9, because above 90% the response time no longer changes linearly, this applies to both the presence and removal of gas as illustrated in Figure I. 3.

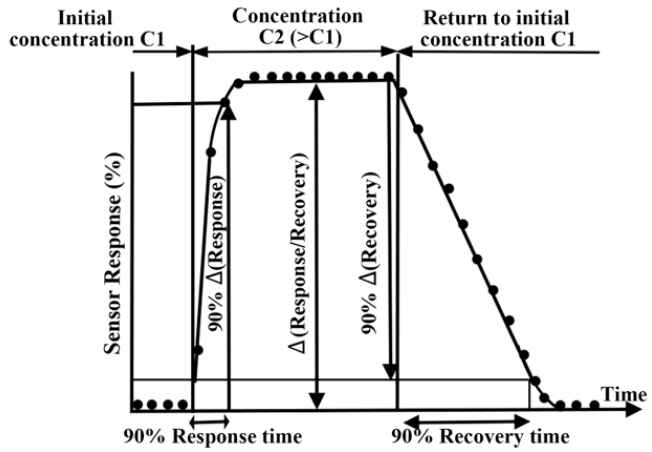

Figure I. 3: Diagram representing the response and recovery times of a semiconductor-based gas sensor. Adapted with permission from [22].

1.2. Semiconducting materials

Materials with resistivity, at room temperature, ranging from 10^{-2} to 10^{9} *Ω.cm* are categorized as semiconductors. Electrical conduction occurs through electrons and holes. A semiconductor can be either pure, in which case it is referred to "intrinsic" or doped with impurities (which control its resistivity), in which case it is named "extrinsic".

As reported by Madou and Morrison [23], within the crystalline structures of matter, electrons have discrete energies that belong to certain sets of values called energy bands. The

low energy bands correspond to electrons participating in the maintenance of the crystalline structure, these are the so-called valence electrons. The high-energy bands correspond to electrons that are almost "free" to detach from the structure and therefore can participate in electrical conduction. An unallowed energy range for electrons (i.e., the band gap) separates the electron bands, which mainly help to determine the properties of a material. Semiconductors behave like insulators at 0 *K*, while by increasing temperatures they exhibit conduction effects because some electrons may have enough energy to move from the valence band (VB) to the conduction band (CB).

At low temperatures, the VB is fully occupied, while the CB is empty. This is because the thermal energy is not high enough to ionize the atoms in the crystal lattice. At higher temperatures, ionization of the atoms can take place, and the ionized atoms yield their electrons to the CB, which partially fills up and participates in electrical conduction. The width of the forbidden band or gap is an important parameter for semiconductors because it represents the energy that must be provided to an electron to move from the VB to the CB.

1.2.1. Charge carrier concentration- Fermi distribution

The distribution of the electrons, for a semiconductor, over the different energy levels is given by the Fermi distribution, which under conditions of thermal equilibrium is written as:

$$f = \frac{1}{1+e^{\frac{E-E_F}{K_bT}}} \qquad \text{Eq. I. 3}$$

where K_b is the Boltzmann constant, T is the absolute temperature and E_F is Fermi level, which corresponds to the energy level where one has the same probability of finding an empty or occupied state (it is a different concept from Fermi energy because the latter is defined as the energy that separates well the empty levels from the filled levels, a useful concept for degenerated semiconductors and metals).

In another way, and on the one hand, the probability of occupation (at equilibrium) of an energy level E by an electron is given by:

$$f_n(E) = \frac{1}{1+e^{\left(\frac{E-E_F}{K_bT}\right)}} \qquad \text{Eq. I. 4}$$

On the other hand, the probability $f_p(E)$ that a level E is occupied by a hole is complementary to the probability $f_n(E)$:

$$f_p(E) = 1 - f_n(E) = \frac{1}{1+e^{\left(\frac{E_F-E}{K_bT}\right)}} \qquad \text{Eq. I. 5}$$

In the case where the difference E-E_F is greater than a few k_bT, equation (I.4) is simplified by noting that the exponential term is significantly greater than 1, hence:

$$f_n(E) \approx \frac{1}{e^{\left(\frac{E-E_F}{K_bT}\right)}} = e^{\left(-\frac{E-E_F}{K_bT}\right)} \qquad \text{Eq. I. 6}$$

This corresponds to Boltzmann's statistics.

In the case where E-E_F is less than a few -k_bT ($\Leftrightarrow$ E_F-E greater than a few k_bT) the following approximation is expressed:

$$f_p(E) \approx \frac{1}{e^{\left(\frac{E_F-E}{K_bT}\right)}} = e^{\left(-\frac{E_F-E}{K_bT}\right)} \qquad \text{Eq. I. 7}$$

For an intrinsic semiconductor, the Fermi level is called intrinsic Fermi level "E_{Fi}" and it is located near the middle of the band gap $E_i = (E_c + E_v)/2$. But in the general case, the Fermi level will depend on the type of dopant and its concentration and, of course, the temperature. What can be said with certainty is that for an n-type semiconductor: $E_F > E_{Fi}$ (which reflects the fact that electrons are more numerous than intrinsic carriers: $n_0 >> n_i$) and for a p-type semiconductor: $E_F < E_{Fi}$.

1.2.2. Intrinsic and extrinsic semiconductors

❖ Intrinsic semiconductors

A semiconductor is called intrinsic when the crystal is not polluted (intentionally or unintentionally) by impurities that can modify the concentration of free carriers. At a temperature different from 0K, the electrons can become "free", i.e. pass from the VB to the CB, and their concentration is noted n. These electrons leave holes in the VB (with a concentration noted p) which are themselves free to move with, moreover, equality between the n and p concentrations. for this particular case, an intrinsic concentration (n_i) is defined which equals the n and p concentrations. In this case the E_F is located very close to the center of the band gap region Figure I. 4(a).

❖ Extrinsic semiconductors

The introduction of certain impurities into a semiconductor material makes it possible to change the number of free carriers, to choose the type of conduction (by electrons or by holes) and to control the conductivity. In this case the E_F can be moved from the middle of the forbidden band (band gap) and the concentration of holes and electrons is different. In some cases, the crystal can be highly doped so that the Fermi energy can move into the CB or into the valence one. In this case, the semiconductor is degenerated, and the Fermi level has almost the same meaning of Fermi energy for metals as it properly distinguishes the empty zones from the filled zones and the semiconductor behaves like a metal.

By considering the extrinsic case, non-degenerated, and based on the movement of E_F, two types can be distinguished:

- n-type semiconductor

The extrinsic semiconductors can be created using the doping methods, which consists of the introduction of foreign atoms to replace the material ones. If they give electrons to the material, they are called donors and a new energy level is created slightly below the CB, which is named donor level (Figure I. 4(b)). In this case, the Fermi level is shifted above the middle of the gap and the electron concentration is much higher than that of holes. Therefore, conduction is by electrons rather than holes. An example for this case is the introduction of atoms from column *V (P for example)* into a crystal from column *IV (Si for example)*.

- p-type semiconductor

If the introduced atoms provide holes to the crystal, they are called acceptors and a new energy level is created slightly above the VB which is named acceptor level (Figure I. 4(c)). In this case, the Fermi level is shifted below the middle of the gap and the holes concentration is much higher than that of electrons. Therefore, conduction is by holes rather than electrons. An example for this case is the introduction of atoms from column *III (B for example)* into a crystal from column *IV (Si for example)*.

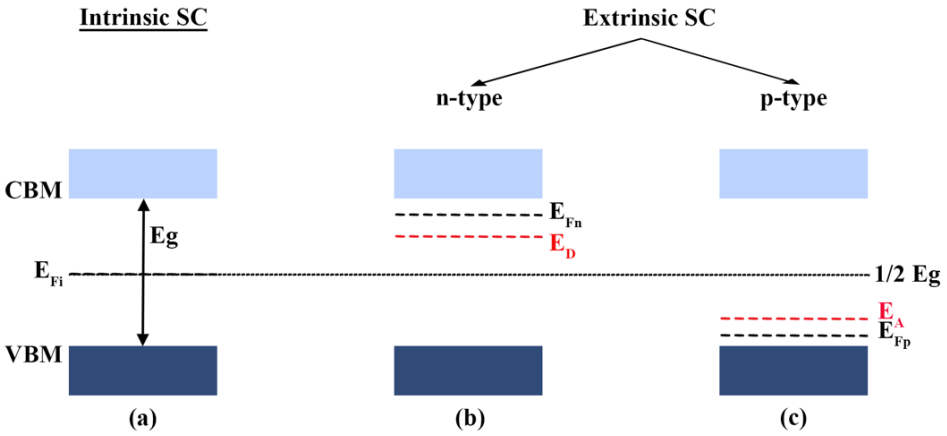

Figure I. 4: Energy band diagram of: (a) Intrinsic semiconductor, (b) n-type semiconductor and (c) p-type semiconductor. The E_D and E_A represent the donors and acceptors levels, respectively.

1.2.3. Poisson equation and depletion approximation

The unidimensional Poisson equation links the electrical potential to the charge density. In this case (depletion approximation, *DA*), it assumes the following form:

$$\frac{d^2\phi}{dx^2} = \frac{qN_i}{\varepsilon_r \varepsilon_0} \qquad \text{Eq. I. 8}$$

where ϕ is the electric potential, depending on the distance x from the surface; N_i is the density of ions in the space charge region; ε_r is the relative dielectric constant of the material and ε_0 is that of vacuum. If the material is homogeneously doped, the density of donors (or acceptors) is independent of x and N_i is constant in the equation I.8. To interpret the functional form of the equation I.8, it is convenient to make a coordinate transformation to

introduce the energy owned by an electron instead of the electric potential. The function V is defined as:

$$V(x) = \phi_b - \phi(x) \qquad \text{Eq. I. 9}$$

where ϕ_b, is the bulk potential of the semiconductor. Substituting the function I.9 in the equation I.8 and then integrating the following is obtained:

$$\frac{dV}{dx} = \frac{qN_i(x-x_0)}{\varepsilon_r\varepsilon_0} \qquad \text{Eq. I. 10}$$

where x_0, is the thickness of the space charge region, determined by the need to totally compensate the layer of surface charge. Imposing the boundary condition for the electric field $\left[\frac{dV}{dx}\right]_{x=x_0} = 0$ at the equation I.10, the semiconductor is discharged for $x \geq x_0$. Inside n-type materials, the number of electrons per unit surface, extracted from the superficial region of thickness x_0 is given by: $N_d x_0 = N_i x_0$. This value should equally be referred to electrons that are migrated towards the surface, so $N_i x_0 = N_s$, in neutrality condition, where Ns is the density of charged surface states. Integrating another time, the equation I.8 and imposing the boundary condition $V = 0$ for $x = x_0$, the following expression is obtained:

$$V(x) = \frac{qN_i(x-x_0)^2}{2\varepsilon_r\varepsilon_0} \qquad \text{Eq. I. 11}$$

Calculating the value of 1.5 at $x = 0$, the so-called Schottky relation is obtained, that expresses the value of the surface barrier V_s (that is the potential V *at* $x = 0$):

$$V_S = \frac{qN_i x_0^2}{2\varepsilon_r\varepsilon_0} \qquad \text{Eq. I. 12}$$

Electrons must have an energy at least equal to qV_s to migrate towards superficial energy levels. Remembering that $N_i x_0 = N_s$, the relation I.12 can also be written in the following form:

$$V_S = \frac{qN_S^2}{2\varepsilon_r\varepsilon_0 N_i} \qquad \text{Eq. I. 13}$$

The relation I.13 is of fundamental importance to quantify the potential difference between the surface and the bulk: the energetic gap, which separates surface-electrons from bulk-electrons as a function of N_s. The entire calculation has been done assuming a "clean" surface (with no adsorbed gas), but in a more general case V_s can also be related with the density of adsorbed oxygen ions (O^{2-} *and* O^-) and of oxygen atoms still present in the atmosphere in a molecular form (O_2), interesting for sensors operating in air.

1.3. Metal-OXides Semiconducting (MOXS) based gas sensors

To satisfy the growth in the demands need, detectors must be effective. The sensor must be sensitive to a small (or even very small) quantity of gas; it must be selective for the gas; the detection process must be reversible and its response/recovery time as short as

possible. Moreover, the device must be easily miniaturized for the industrial production. To date, no material meets all these criteria simultaneously, however, as it is reported in Table I. 1 semiconductor-based gas sensors appear to be very promising candidates and have attracted a great deal of research attention over the last ten years. They are the most investigated since their excellent sensitivity, good stability and low-cost of production [24] [25] [26] [27] [28]. In this thesis, the studies will be focused on nanostructured semiconductor-based gas sensors, knowing that the chosen host material is tin dioxide (SnO_2) due to its broad spectrum of physical and chemical properties. The sensing semiconductor layer (SnO_2) is one of the essential elements constituting the sensor, whish conductivity depends on the environment with which it interacts.

Many metal oxides have been studied and used for gas sensors. Table I.2 presents the main metal oxides marketed and studied in the field of gas sensors. A wide variety of oxides have been studied such as binary oxides, ternary oxides, but also complex oxides.

Table I. 2: Main metallic oxides marketed and studied in the field of gas detection.

Sensors/sensing material		Detected gas
Commercialized	HS129 (SnO_2)	Isobutane, propane, ethanol, hydrogen
	HS131 (SnO_2)	Isobutane, methane, propane
	HS134 (SnO_2)	Carbon monoxide
Studied	SnO_2 [29] [30]	Ethanol, carbon monoxide, nitrogen dioxide
	In_2O_3 [31]	Nitrogen dioxide
	ZnO [32] [33]	Ethanol, methanol, acetone, ammonia, benzene, chlorobenzene, toluene,
	TiO_2 [27] [34]	Carbon monoxide, nitrogen dioxide, oxygen
	WO_3 [35] [36]	Nitrogen dioxide, ammonia
	$SnWO_4$ [37]	Hydrogen sulfide, hydrogen
	$MgxZnyFezO$ [38]	Hydrogen, carbon monoxide, nitrogen oxide

1.3.1. MOXSs based gas sensors design

Sensors based on metal oxides in solid form generally consist of [39, 25, 40, 27]:

- A sensing oxide-semiconductor layer, which interacts directly with the target gas.
- Electrodes to carry out electrical measurements and to monitor the interaction process.
- A heating system (optional) to control and regulate the temperature of the sensing layer.

These different elements are generally distributed according to the diagram in the Figure I. 5. The simple design of such a system makes the metal-oxide sensor a very suitable and economical material for the production of gas sensors.

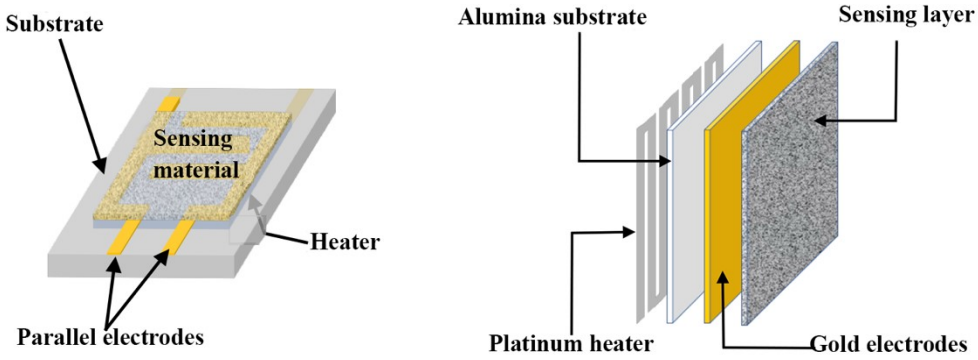

Figure I. 5: Diagram of the different constituent parts of a solid sensor.

The electrodes are used to measure and monitor the change occurring on the surface of the sensing layer when it is interacting with the target gas, i.e. in the case of sensors based on SnO_2 (n-type semiconductor) interacting with a reducing gas, first the sensor is exposed to the atmosphere before the target gas is introduced, oxygen species are adsorbed on the surface of the active element (SnO_2) decreasing its electrical conductivity and then creatin a potential barrier between grains composing the nanostructured SnO_2. When the sensor is exposed the gas (reducing in this case), the gas molecules interact with chemisorbed oxygen species from the surrounding atmosphere and decrease the resistance of film. The geometry and the nature of the material chosen for the electrodes must favor the transfer of a maximum of charges from the sensing layer to the measurement circuit. The most commonly used electrode material is gold (*Au*) for its long-term stability in gaseous atmosphere and under temperature. Although other elements such as platinum (*Pt*) or Aluminum (*Al*) are also used to manufacture the electrodes of gas sensors.

The heater located under the substrate that separate it from the sensing element, allows to control and regulate the temperature of the sensing layer. Indeed, in the thermo-activation mode of sensors, the interaction between the gas and the film like many reactions is thermally activated. In this case, the temperature plays an important role in the gas detection. Therefore, the material used and the geometry of the electrode are also parameters to be taken into account when designing a gas sensor. The use of metals such as platinum (*Pt*), titanium (*Ti*),

nickel/chromium alloy (*Ni/Cr*) guarantees stability over a wide temperature range and also a long service life. Another heating method is to place the measuring cavity into a furnace. Thus, it is not necessary to place a heating system on the substrate.

1.4. Gas/sensor interaction principle

This part deals mainly with the elementary mechanisms of surface physics, related to the operation of a gas sensor.

1.4.1. Surface interactions

In general, there is an effect due to interactions between gases and the semiconductor surface, namely bulk effect, according to which the semiconductor stoichiometry is modified by the presence of a gas or organic steam. A semiconductor in the air undergoes a stoichiometric change because of the interaction between air oxygen and the semiconductor, where the material captures part of the oxygen with consequent alteration of its conductivity. This is at the basis of complex chemical-physical mechanisms linked to the variation in conductivity of the material itself [41].

To pass from grain to grain, electrons must cross the surface potential barrier at the external shell of all grains of the material. The electrical conductivity of semiconductors is proportional to the density of electrons n_s at the surface of grains and close to the superior limit of the potential barrier.

Furthermore, n_s exponentially varies following the surface barrier potential qV_s. Indeed:

$$n_s = N_c e^{-\frac{qV_S + E_C - E_F}{K_b T}} = N_d e^{\frac{qV_S}{K_b T}} \qquad \text{Eq. I. 14}$$

where N_C is the effective density of energetic states near the *CB*. It is so necessary to present a model in order to describe variations of the density n_s due to the adsorption of the atmospheric oxygen on the surface of the semiconductor. For a complete treatment, one must also take into account other atmospheric (reducing or oxidizing gases).

When a surface is exposed to a gaseous medium, it will interact with it. The gas molecules will collide with the surface of the host material through thermal agitation. Three possible cases can be distinguished then:

- "Scattering", the gas molecule hits the surface under an elastic shock, loses very little energy and bounces off the surface.
- "Trapping", the gas molecule loses energy during the collision but retains enough energy to be mobile on the surface.

- "Sticking", the gaseous molecule dissipates a lot of energy and remains immobile on the surface after the collision. The study proposed in this thesis was focused on this phenomenon as it describes the gas-sensor interaction.

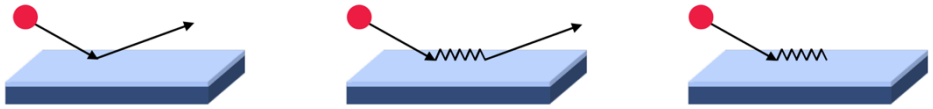

Figure I. 6: possible cases for the adsorption of gas molecules on a surface. (a) scattering, (b) Trapping and (c) Sticking.

1.4.2. Adsorption

The mechanism for attaching a gaseous molecule to the surface of a solid is called adsorption. The gaseous molecule (called adsorbate) is adsorbed on the surface of the solid (called adsorbent) by adsorption sites: metal or oxygen atoms, or vacancy. Depending on the strength of the interaction between the two objects under consideration, there are two types of adsorption: **physisorption and chemisorption**.

- The name **physisorption** means a weak interaction between the gas molecule and the surface of the solid (the host material in this case). Van der Waals-type or electrostatic forces are involved, with adsorption heats from 1 to 20 kJ/mol, but no electronic exchange takes place between the molecule and the surface of the material. This interaction does not allow us to easily characterize the presence of a gas.
- If the interaction between the gas molecule and the surface involves higher energy forces, in addition to the existence of electronic exchanges, then it is an adsorption of the chemical type or "**chemisorption**". This type of interaction is one of the pivots in the gas detection process since the exchange of electrons between the two species will modify the surface electron properties of the host material. Figure I. 7 illustrates the principle of chemisorption, which can be **molecular or dissociative** if the molecule decomposes on the surface of the adsorbent to form ions (also called ionosorption).

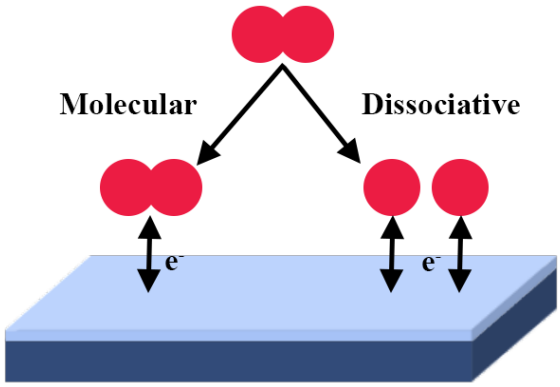

Figure I. 7: Principle of molecular and dissociative chemisorption.

For the oxygen molecule (O_2), as an example, the molecular chemisorption takes place in the O_2^- form, whereas dissociative chemisorption will lead to the formation of O^- ions on the surface of the sensitive layer.

1.4.3. Desorption

The molecule or ion adsorbed on the surface can leave it under certain conditions, this is the phenomenon of desorption. Depending on the interaction envisaged, the energy required to start the adsorbate will be more or less important. Thus, physisorption is easily reversible whereas chemisorption will require a higher energy input (heating and/or pumping) and will be in some cases irreversible, a contamination of the sensor host material can be happen then. Recombination between species adsorbed on the surface and those in the gas phase can also lead to desorption. Surface adsorbed species (atoms, ions or molecules) are in thermal equilibrium and can recombine with each other during their diffusion, and finally they desorb with a sufficient supply of activation energy. This mechanism is called Langmuir-Hinshelwood recombination and it is reported in Figure I. 8.

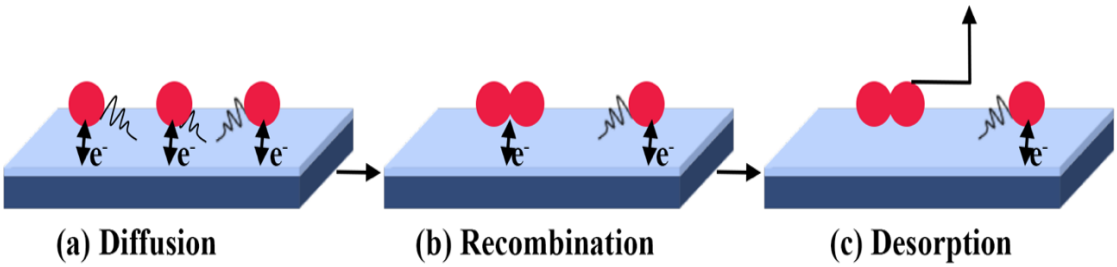

Figure I. 8: Recombination of Langmuir-Hinshelwood.

The second type of recombination observed corresponds to a heterogeneous catalysis mechanism called Eley-Rideal recombination shown in Figure I. 9. In this mechanism, the species in the gas phase will react with species adsorbed on the surface of the host material, due to the balance of exchanges between these two media. The molecule (or ion) in the gas phase will collide with an adsorbed on the surface of the host material leading to a rapid reaction between the two and desorption of the product.

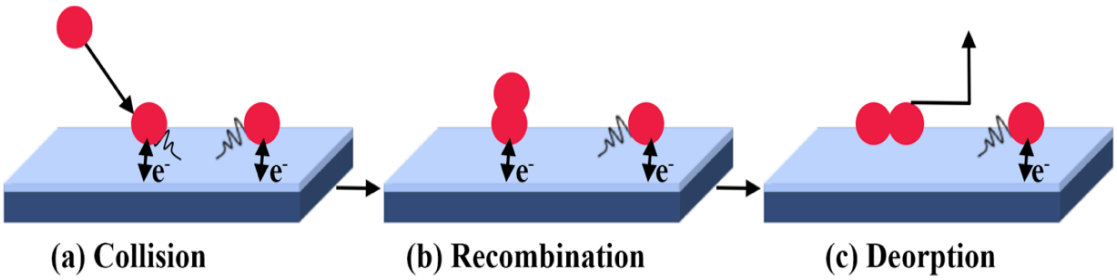

Figure I. 9: Recombination of Eley-Rideal

1.4.4. Oxygen adsorption

The principle of operation of semiconductor oxide sensors is based on changes in conductivity, due to doping, by gas adsorption on the surface of the host material. The reaction mechanism that takes place between the sensor and the target gas is primarily based on the interaction between the last and the oxygen species adsorbed on the surface of the host material [42] [43]. As metal oxides are made up of oxygen vacancies whose concentration depends on the method of production, they will naturally react with the oxygen present in the environment. Oxygen is therefore the precursor of the detection reaction. Adsorbed on the surface, it can exist in several forms depending on the temperature [44] [45], each form having its own reactivity. At room temperature, oxygen is present on the surface in physisorbed form $O_{2,phys}$, but it does not participate in the detection mechanism. At higher temperatures (from T = 160°C), oxygen will be chemically absorbed in the form of $O^-_{2,ads}$. At higher temperatures (T > 300°C), chemisorption will take place in dissociative form O^-_{ads} and O^{2-}_{ads} (unstable form). However, if the temperature has become too high (T > 600°C), the oxygen in the network will then start to migrate to the surface and finally desorb from it (Figure I. 10).

The corresponding chemical balances are [46] [47] [48]

- Physisorption of oxygen:

$$O_{2,gas} \rightarrow O_{2,phys} \rightarrow O_{2,ads}$$

- Chemisorption of oxygen:

$$O_{2,ads} + e^-_{ZnO} \rightarrow O^-_{2,ads}$$

$$O^-_{2,ads} + e^-_{ZnO} \rightarrow 2O^-_{ads}$$

$$O^-_{ads} + e^-_{ZnO} \rightarrow O^{2-}_{ads}$$

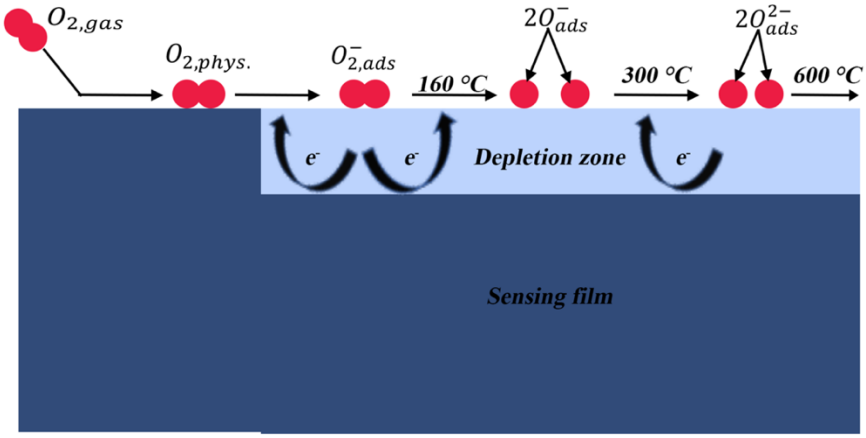

Figure I. 10: Principle of adsorption of oxygen on the surface of the sensor [48].

The adsorbed oxygen, on the sensing layer surface, due to its oxidizing properties, will capture electrons from the CB of the host material. Thus, it will leave an electron-depleted zone on the surface of the sensing layer, the depletion zone. This electronic depletion will have the immediate consequence of decreasing the conductivity (or increasing the resistivity) on the surface. The opposite effect can be observed in sensors using p-type semiconductors as host material.

The oxygen present in the gas phase is always in equilibrium with the oxygen adsorbed on the surface of the host material. As a result, any phenomenon causing a variation in the quantity of oxygen (in the gaseous or adsorbed phase) will lead to a variation in the resistance.

1.4.5. Reducing /oxidizing gas

So far, for detection in air, the target gas interacts with the oxygen adsorbed on the surface of the host material. In general, ahead of semiconductors (n-type and p-type), gases can be classified in two categories according to their oxidizing or reducing nature.

Gases with an oxidizing character, such as ozone (O_3), nitrogen dioxide (NO_2) or chlorine (Cl_2), will capture electrons from the CB of the host material. In the case of detection in air, oxygens are adsorbed on the surface of the host material and the gas will interact with them and trap electrons. The exact mechanisms leading to gas detection are still unknown and several phenomena can make the interpretation of the conductivity variation difficult. Indeed, if oxygen is desorbed, either by a decrease in the oxygen content in the gas phase or by heterogeneous catalysis with the target gas, it will leave behind a vacant site (adsorption site), which will be the seat of competition between several gases likely to adsorb there (Figure I. 11).

In the case of an n-type semiconductor, the conduction is mainly electronic, the reaction with the oxidizing gas will lead to a decrease in the electron density *m* on the surface of the material and thus a decrease in conductance. Namely that for a p-type semiconductor the conduction is based on holes carrier, the gas will first capture the electrons of the CB of

the material (which are in very small quantities) and then those of the VB leaving holes behind. This mechanism will lead to an increase in the concentration of holes and thus an increase in the surface conductivity of the p-type material.

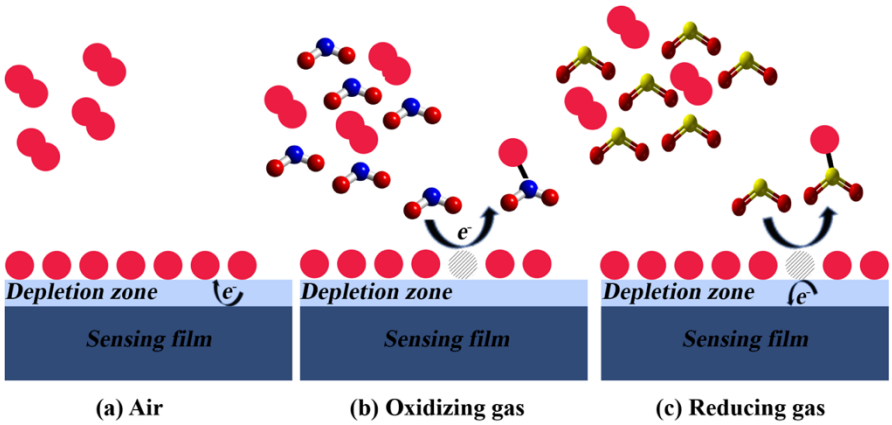

Figure I. 11: Reaction, in the presence of the air, of an oxidizing (b) or reducing (c) gas with the surface of a sensor based on n-type semiconductor.

In the case of reducing gases, the opposite effect is observed, i.e. an increase in the surface conductivity of an n-type material. Reducing gases such as ethanol (C_2H_6O), acetone (C_3H_6O), ammonia (NH_3), carbon monoxide (CO), benzene (C_6H_6) or hydrogen (H_2) will interact with surface adsorbed oxygen and release electrons previously captured by the latter (Figure I. 11(c)). These electrons will then populate the depletion zone and increase the electron density in this region, thus increasing the surface conductivity of the host material.

1.4.6. Influence of humidity and temperature

It is now undeniable that the relative humidity of the environment in which the sensor is placed will influence the surface conductivity of the host material [46] [49]. The water will adsorb on the surface of the material and compete with the ambient oxygen. Water can be adsorbed in the molecular form H_2O at temperatures below 150°C; or in the form of hydroxyl groups HO^- which have a desorption temperature of 250°C.

Once adsorbed, the water will modify the reactivity of the surface and block adsorption sites with, in some cases, an absorption of hydrogen in the sensor network [50].

Studies have shown that in the case of SnO_2, sensitivity to CO is increased in the presence of moisture [40]. Hypothetical mechanisms have been put forward to explain these phenomena, involving a decrease in the number of sites available for oxygen following water adsorption or the creation of HO^- sites that would catalyze the CO decomposition reaction. The presence of moisture therefore does not necessarily have a detrimental effect on the adsorption reactions but greatly complicates their interpretation.

To solve the problem encountered in the presence of water, one needs to work at temperatures higher than those of the desorption of the HO^- groups. In addition, the adsorption

reactions are endothermic, and the heat input will promote these reactions. Higher temperatures will therefore increase the charge transfer, the electrons in the case of an n- type semiconductor directly influencing the surface properties and the sensitivity of the material. The increase in operating temperature leads to an acceleration of the kinetics and a decrease in the characteristic response and recovery times. For a given surface area, each gaseous species will have an optimal operating temperature. It thus appears that the operating temperature is a means of improving gas selectivity. Figure I. 12(a) and (b) show the evolution of the relative response as a function of operating temperature for a sensor based on non-oriented *ZnO* nanorods [47] and a *ZnO* nanorods array [51], respectively, under different gaseous atmospheres. There is clearly a variation in selectivity, for a given gas, depending on the operating temperature.

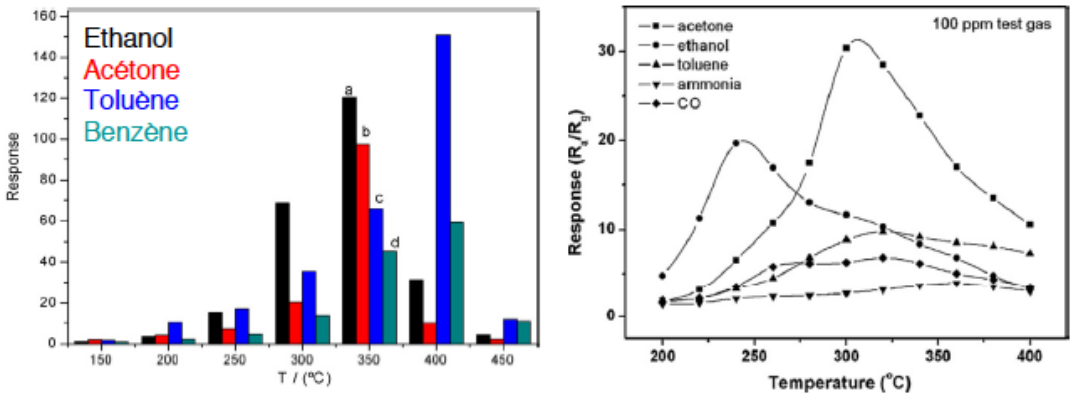

Figure I. 12: Examples of relative responses of sensors under different atmospheres. (Left) Undirected ZnO nanorods, adapted with permission from [47] and ZnO nanowire network (right), reprinted with permission from [51].

Nevertheless, the use of high operating temperatures (> 100°*C*) remains a major disadvantage. Indeed, such temperatures require energy consumption and especially a risk in the presence of fuel vapors and may therefore require the installation of a cooling system to limit the effect of thermal convection.

A lot of effort has been made in this direction in order to lower the operating temperature while maintaining a measurable sensitivity. Thus, Li et al [52] reported the study of the detection properties of indium oxide (In_2O_3) nanowires at room temperature. Geng et al [53] studied the detection of ethanol and acetone vapors by spherical nanostructures composed of multilayers of ZnO at a temperature of 150°*C* and showed a linear evolution of the response to the target gas concentration. In general, most teams that have worked in this field first determining the optimal operating temperature. This may vary depending on the morphology, processing method and electronic properties of the host material. It appears that a large number of the sensors studied show a measurable electrical activity at temperatures below their optimum operating temperatures. For example, Chen et al [54] investigated the detection

properties of ethanol using *ZnO* nanorods arranged in a flower shape. The results show that the response at 140°*C* (S ~ 10.9) is sixteen times lower than at 300°*C* (S ~ 176.8).

In conclusion, although temperature is an important parameter to increase sensitivity and decrease characteristic reaction times through kinetics, temperature can be a disadvantage requiring additional devices.

1.4.7. Influence of doping

The selectivity of semiconductor oxide sensors appears to be their main disadvantage and that in some cases it can be circumvented by means of the operating temperature. However, if the working temperature is fixed for practical and/or safety reasons, improved selectivity is no longer possible.

The most common method used to improve the selectivity of these sensors is doping. The principle consists of adding a small amount of a metal or oxide in the lattice of the considered material. The effect of doping can be multiple: the sensitivity for a given gas is increased while towards others is decreased. There is also an improvement in reaction times and a change in the optimum operating temperature.

Table I. 3: List of dopants for metal oxides reported in the literature.

Material@Dopant	Target gas	Reference
$SnO_2@PdO$	CO	[55]
$SnO_2@CuO$	H_2S	[55]
$SnO_2@La_2O_3$	CO_2	[55]
$SnO_2@TiO_2$	*Ethanol*	[56] [57]
$ZnO@SnO_2$	*Toluene*	[58]
$ZnO@RuO_2$	NH_3, H_2S	[59]
ZnO@Sn	*Ethanol*	[60]
ZnO@Pd	NH_3	[61]
ZnO@Pt	*Ethanol*	[62]
ZnO@Ti	*Ethanol*	[63]
ZnO@Ce	*Ethanol*	[42]

ZnO@Cd	NO_2	[47]
ZnO@Ni	*Acetone*	[64]
ZnO@In	*Acetone*	[65]
ZnO@Au	*Acetone*, NO_2	[66] [28]
ZnO@Co	*Ethanol, CO*	[67]
ZnO@Al	*CO, LPG*	[68] [69]
ZnO@CuO	H_2	[70]
ZnO@Cu	H_2S	[71]

(* LPG = Liquefied Petroleum Gas).

Despite the wide variety of dopants available, it remains difficult to associate a dopant with a specific gas and mixed doping may be necessary to detect a gas within a mixture.

Sun et *al.* [43] have studied the influence of temperature on the response of a sensor based on *ZnO* nanorods (non-oriented), the response obtained in the presence of 100 ppm of ethanol is maximum for a temperature of 330°*C*. The addition of 0.5 mass % silver improves sensitivity and gives a response almost two times higher than the undoped sample, at the same temperature of 330°*C*. In this way, for an equal response, the addition of silver reduced the operating temperature from 330°*C* to 240°*C*. Similarly, Zeng et al [72] observed a four-fold increase in sensitivity per 100 *ppm* toluene at 275°*C* following doping of *ZnO* nanostructures with titanium oxide TiO_2. Nevertheless, selectivity is not improved, and it is not possible to discriminate the presence of toluene among other gases.

Several forms of doping exist, in the lattice of the material constituting the sensor and on the surface of the host material. These two forms of doping can lead to different detection behaviors, Wagh et al [59] performed a doping of thick *ZnO* films with ruthenium (*Ru*) and the results obtained show that the surface-treated films have a much better response than those containing RuO_2 in the lattice.

Despite these improvements, the scientific community is not unanimous about the mechanisms behind these changes in properties. Two mechanisms are proposed [26]:

- The first is a mechanism based on the "spillover" effect of the additive.

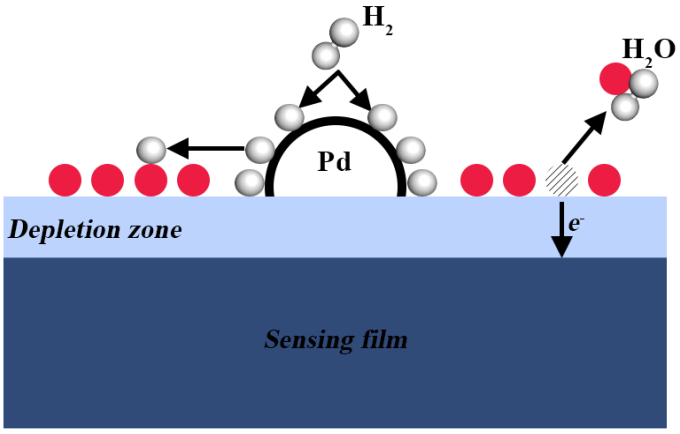

Figure I. 13: Spillover catalytic mechanism: the gas molecules (H2, O2) are dissociated on the surface of the additive and then migrate towards the oxygenated species on the surface before being desorbed. This mechanism does not affect the resistance of the semiconductor.

In this mechanism, the dopant will dissociate molecules such as O_2 or H_2 on its surface and these will then migrate to the sensitive layer; similarly, to the dissociation of H_2 on palladium (*Pd*) particles. This has the consequence of increasing the surface concentration of active species (H_2) and thus increasing the charge transfers between the sensitive layer and the surface oxygen.

- The second mechanism is based on an electron transfer between the dopant and the sensitive material. The surface additive will be oxidized by the oxygen species and in turn will accept electrons from the sensitive layer. Due to the presence of the dopant, the quantity of oxygen species adsorbed on the surface is greater.

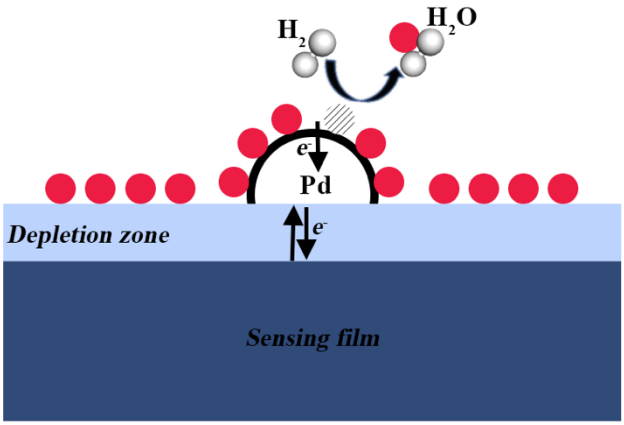

Figure I. 14: Catalytic mechanism of electronic additive-adsorbent interaction: the oxygenated species are adsorbed on the surface of the additive. An electronic exchange appears between the additive and the adsorbed species.

The doping of a sensitive metal-oxide layer appears to be a means of improving the selectivity defects of these and increasing their sensitivities. However, care must be taken not to poison the surface with too much doping.

1.5. Activation of a nanostructured semiconductor

Nanostructured semiconductors usually need to be "activated" to enhance chemoresistive properties. Indeed, without any activation, these materials suffer two main drawbacks that limited their functionality:

- The low number of charge carries which results in a high resistance of the semiconductor.
- Low surface reactivity, which limits the catalytic effect of the semiconductor in a gas-solid interaction.

Principal methods used to activate a nanostructured semiconductor as a chemoresistive gas sensor are an excitation by means of radiation (photo-activation mode) or thermal heating (thermo-activation mode).

1.5.1. Thermo-activation mode and grain size role

Consider a semiconductor film without intergranular resistance. Its variation of surface conductivity is defined as:

$$\Delta\sigma_x = q\mu_c\Delta_n + q\mu_p\Delta p \qquad \text{Eq. I. 15}$$

with σ volumetric conductivity, μ_c and μ_p mobility of electrons and holes, i.e. their velocity rate per unit of electric field, linked to the temperature by the following relation:

$$\mu \, \alpha \, T^{3/2} \qquad \text{Eq. I. 16}$$

where Δp and Δ_n indicate the holes per unit area in the depletion layer and the change in the actual number of electrons. It is assumed, however, that the variation in the number of holes is negligible and that the surface mobility of the electrons coincides with that of the bulk.

The conductance of a crystal width *W*, thickness *t* and length *L* is defined as:

$$G = \sigma W \frac{t}{L} \qquad \text{Eq. I. 17}$$

The dependence of the charge carrier density on temperature is a function of the energy levels of the dominant donors. If the donor levels are close to the CB, donor ions will be completely ionized at room temperature. In this case, as temperature increases, the electron density in the CB remains unchanged. If the donor levels are deeper, the electrons will not be fully excited to the CB at room temperature; instead, above this temperature, the density of the conducting electrons increases exponentially with the temperature.

It is possible to produce defects in the lattice that alter the conductivity at sufficiently high temperatures, irrespective of the depth of the donor levels.

The charge carriers move forced by an electric field imposed by the outside, and by diffusion associated with a concentration gradient. In the one-dimensional case, the current density flow is defined as:

$$J_i = \sigma_i E - \Delta_i z_i e \frac{dc_i}{dx} \quad \text{Eq. I. 18}$$

with E external electric field, Δ_i diffusion coefficient of *i-th* species, z_i the number of electronic charges on the *i-th* particle and c_i the concentration of the *i-th* species.

Considering a semiconductor oxide in presence of gases in the atmosphere, the conductance variation is expressed as the difference between bulk conductance, G_{x_0}, and conductance loss (or gain) due to surface effects, G_0, i.e.,

$$G_{x_0} - G_0 = \Delta_n \frac{W_u}{L} \quad \text{Eq. I. 19}$$

By knowing the conductance at $V_s = 0$ (V_s represents the value of the superficial barrier) and by measuring the variation of the conductance $G_{x_0} - G_0$, it is possible to directly calculate the variation of the actual number of electrons, Δ_n.

Conductivity loss due to surface effects is a small fraction of the bulk conductance, unless the sample is very thin, i.e. with a thickness similar to the depletion layer.

In order to increase the sensitivity to the gas, surface fluctuation variability should be prevalent, increasing the surface/volume ratio. This is achieved by creating a very fine grain superficial morphology, thus creating a strong porosity.

This leads to introducing the conduction mechanisms that provide electrical signals measured by the sensor. The gas sensors used are constituted of a porous layer composed of partially sintered granules of the sensitive material, so the electrons are obliged to cross the surface barrier formed in the intergranular contacts. The porous morphology of the material as described above allows the gas to reach a certain thickness of the surface material and consequently the surface of interaction with the gas is wide.

It cannot be assumed that all intergranular contacts are at the Schottky barrier. It is possible to distinguish two different types of intergranular contacts:

- "open neck" contact: surface states cause a depletion layer extending to the depth (Figure I. 15(a)). In this case conductivity is mostly due to the non-emptied layer at the center of the neck. The conductance is determined by the activation energy of the electrons of the donor states in the bulk and it will be changed by the gaseous atmosphere only by variations in the channel width.
- "closed neck" contact: depletion layers of the two surfaces overlap while leaving a strip through the center with greater resistance (Figure I. 15(b)). This geometry may result from an incomplete sintering that leaves a narrower neck,

or it can be produced by an open neck in which the depletion layer is modified by a gaseous atmosphere variation. In this case, the conductance would be determined by the activation energy of the electrons of the surface states in the CB; the influence of the gaseous atmosphere would be directly on the occupation of superficial states.

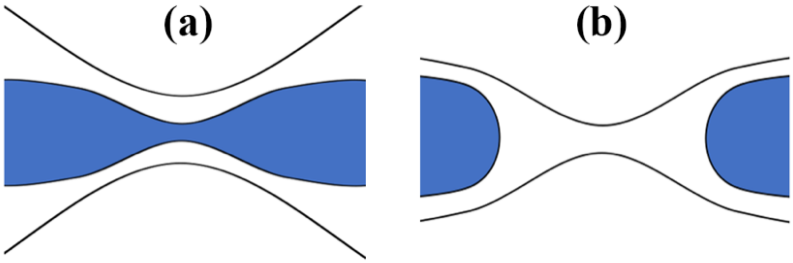

Figure I. 15: a) Open neck and b) closed neck adapted from [23].

Inside the semiconductor grains the behavior is ohmic with the Schottky barrier Contact, but in the contact points, due to surface charge, a Schottky barrier is formed. In this latter type of contact the conductivity will be limited by the charge transport through the barrier resulting:

$$\sigma \approx \mathrm{cst}(t)\, e^{\frac{-q\Delta V_s}{kT}} \qquad \text{Eq. I. 20}$$

This situation represents a limit case of the two previous ones; the activation energy for conductance will be directly related to the surface charge of the species present in the gaseous environment and, therefore, it is a function of the composition of the atmosphere. The exponential factor takes on great importance in polycrystalline materials with many intergranular contacts and consequently a high surface/volume ratio. In the intergranular contacts, the electrical resistance increases because in the area close to the surface there is the depletion layer. It turns out that just intergranular contact will be responsible for most of the resistance provided by the sample since chargers will be forced to cross the V_s potential barrier to switching from one grain to another. To obtain an equation that provides an approximate expression of the conductance of a polycrystalline semiconductor oxide film, G_0 is assumed to be proportionality constant, the function of the bulk and geometric parameters of the device. Thus, G can be expressed as follow:

$$G = G_0 e^{\frac{-q\Delta V_s}{kT}} \qquad \text{Eq. I. 21}$$

The capture of electrons by ion-adsorbed oxygen raises significantly V_S potential barrier, causing a variation in conductance. The activation energy for conductance, qV_S, is influenced by the charge and by the coverage fraction of superficial species and, thus, it is a function of the composition of the atmospheric gases. Given the fundamental role played by surface effects in the operation of gas chemical sensors, it is clearly necessary to realize

polycrystalline semiconductor films in which the grains are as small as possible. Indeed, the small grain size increases the surface/volume ratio, inversely proportional to the radius, making superficial effects dominant over bulk ones.

1.5.2. Photo-activation mode

Therefore, via photoexcitation, it is possible to obtain the promotion of an electron (e^-) to the CB and the consequent formation of a hole (h^+) in the VB. The result is an electrical conduction of the semiconductor (Figure I. 16).

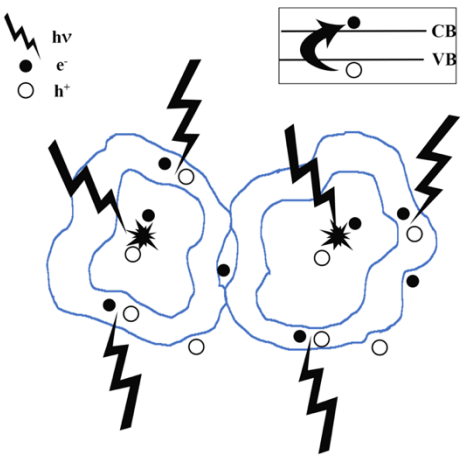

Figure I. 16: Representation of two semiconductor crystallites in contact and the formation of electron-gap pairs after lighting with energy equal to or greater than the band-gap energy (Adapted from [73]).

In this situation, in the presence of a gaseous or liquid phase at the semiconductor interface, a spontaneous adsorption of atmosphere gas molecules occurs according to the energy level (or potential redox) of each adsorbate. The catalytic processes involve these "free" holes and electrons, which can react with species adsorbed by an aqueous solution or air on the surface of the semiconductor.

Once the electron and gap excitation occur, there is a lifetime of the nanosecond order in which photoelectron and photo-hole can transfer their energy to superficial states adsorbed by a liquid or gaseous phase on the surface of the semiconductor. If the semiconductor stays intact and the charge transfer to the adsorbed species on the surface is continuous and exothermic, then it is possible to obtain a process named heterogeneous photocatalysis [74]. There will be a transfer of photoelectrons to accepting molecules (oxidizing gases) and photo-holes towards molecules of electron donating gases (reducing agents), as shown in the following reactions and in Figure I. 16:

$$h\nu + (SC) \rightarrow e^- + h^+$$

$$A_{ads} + e^- \rightarrow A_{ads}^-$$

$$D_{ads} + h^+ \rightarrow D_{ads}^+$$

where *SC* indicates the semiconductor.

Each ion coming that has interacted on the surface can subsequently react with other molecules present in the atmosphere to form intermediate and final compounds of the photocatalytic reaction [75].

The use of photocatalytic reactions offers several advantages over others conventional techniques:

- Reactions can also occur at a low ambient temperature and pressure concentrations.
- The treatment is economical, potentially allowing the use of solar energy.
- Monitoring is also possible for thermo-degradable gases.

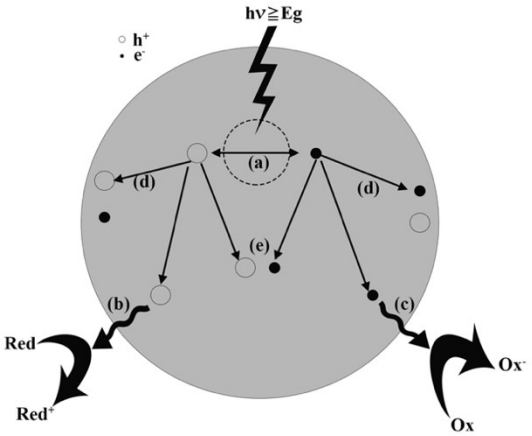

Figure I. 17: Illustration of the phenomenon of photo excitement in a semiconductor nanoparticle. The main processes described are a) formation of the electron/hole pair; b) Oxidation of donor D; c) Reduction of AC; d) and e) recombination of the electron-hole pair respectively on the surface and on the bulk (adapted from [76]).

There is also the possibility of recombination between the CB electrons and holes created by the photoexcitation. This inconvenient phenomenon of recombination is favored by so-called "trap sites", which can be on the surface or on the bulk. In particular, it occurs when surface oxygen vacations and lattice defects provide new localized energy states that are not available in the "perfect" crystal. Furthermore, the surface represents a sudden discontinuity of the crystal, so it also provides a high density of energy states, located precisely in the surface region, which behaves as a trap state for the electrons.

1.6. Thick-film sensors production:

To understand the process of preparation of thick-film sensors is necessary a synthesis of all crucial aspects of the fabrication process. Thick-film technology is a particular form of serigraphy introduced in the field of technology during the 70's in order to construct printed hybrid circuits. It was applied for the construction of electronic components used in various sectors. Thick-film hybrid circuits are famous for their multiple qualities such as compactness, robustness and low-cost production. Thick-film technology is also relevant because it allows to build very precise geometries, so it is useful in the sensor field. In the last years, the

serigraphic technique has highly evolved even if the applied procedures have not substantially changed. However, what makes the thick film technology suitable for the realization of sensors is its low cost combined with the capability to operate also in hostile working conditions. These sensors have the following advantageous characteristics:

- Good sensitivity even at low gas concentration
- Discrete reliability and repeatability of the measurement
- Low energy consumption
- Small dimensions
- Excellent cost-performance ratio
- Ease of automation.

Figure I. 18 shows the main steps needed to fabricate a thick film-based gas sensor.

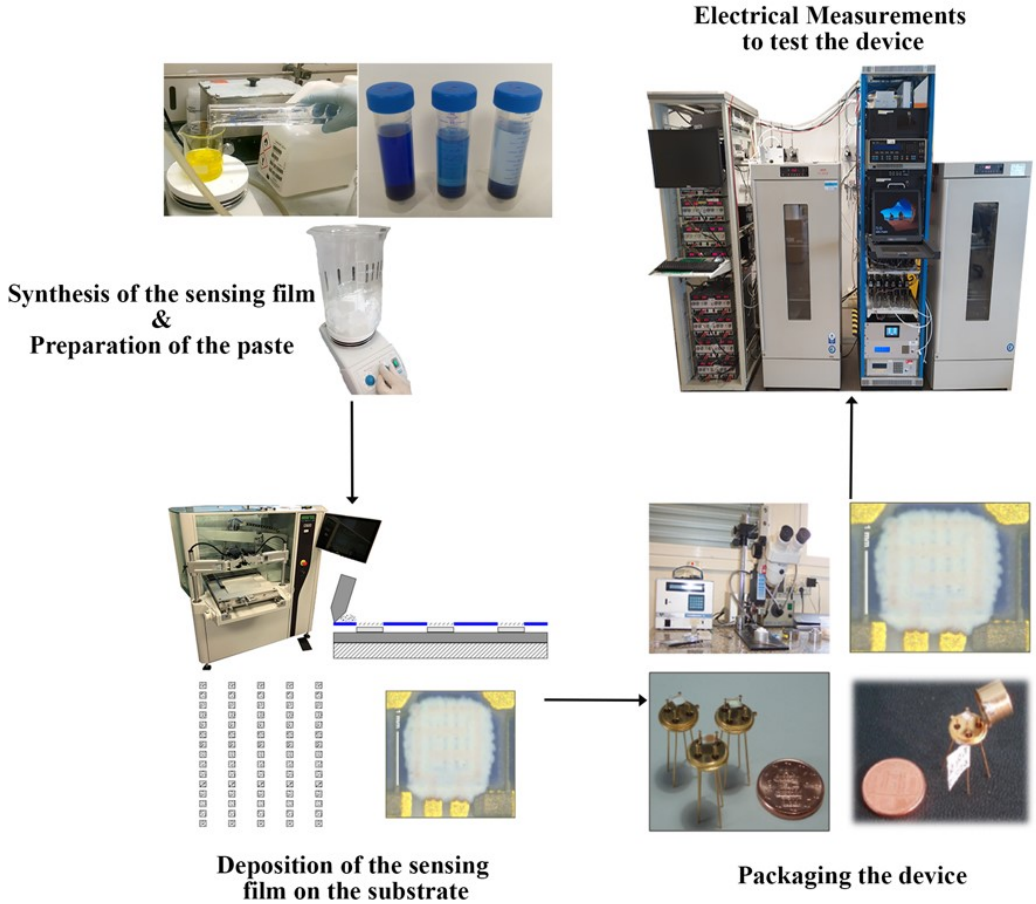

Figure I. 18: Steps for thick film gas sensors production.

1.6.1. Synthesis of sensing film

Metal-oxide semiconductors are developed by various techniques, including the spray pyrolysis technique, Atmospheric Pressure Chemical Vapor Deposition (*APCVD*) and sol-gel are the most used. In this thesis, the sol-gel technique was used to synthesize sensing materials.

1.6.1.1. Sol-gel technique:

The name sol-gel is a contraction of the terms "solution-gelation". The "sol-gel" method is one of the most used technologies for the production of metallic oxide layers, in particular SnO_2 of continuous forms and of good cohesion on substrates, such as silicon. Although it has some disadvantages such as the low annealing temperature which does not allow us to obtain a total crystallization of SnO_2 as well as the presence of foreign elements that are difficult to remove such as $SnCl_4$, but it still present one of the most used method for the synthesis due to its simplicity and low-cost.

Figure I. 19 shows a simplified diagram of the sol-gel technique.

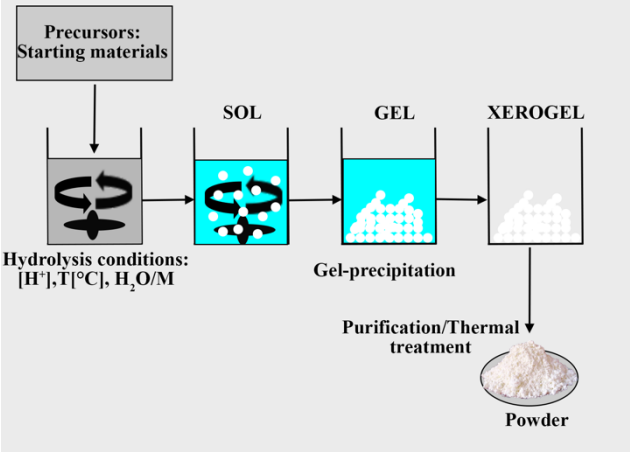

Figure I. 19: Simplified schematic diagram of sol-gel processing.

1.6.2. Material characterization

To obtain high performance thick films, the synthesis of pure nanostructured powders is a very important step. It is of great importance to obtain regular and nanoscale structures, because a large number of atoms on the surface and the efficient Van der Waals, Coulombic and interatomic coupling significantly modify the physical and chemical properties of low-dimensional materials. Nanostructures characterized by small size and high surface-to-volume ratio are the best candidates to improve the detection capability of chemical and biological species [77]. For this reason, a thorough characterization of the resulting products is fundamental to improve the synthesis process and to obtain an optimized sensing material. For this purpose, many techniques were proposed to analyze nanostructured materials, among these techniques: Scanning Electron Microscope – Energy-Dispersive X-ray spectroscopy (SEM-EDX), Transmission Electron Microscopy (TEM), X-ray Photoelectron Spectroscopy (XPS), Atomic Force Microscope (AFM), Infrared spectroscopy (IR), X-ray Powder Diffraction (XRPD), Raman scattering spectroscopy, X-ray Fluorescence spectroscopy (XRF), UV-visible spectroscopy…etc.

In this section, the most common techniques used for characterization of materials in the sensing application that are XRD, XPS, SEM-EDX and TEM are called.

1.6.2.1. X-ray Diffraction

X-ray Powder Diffraction (XRPD) or simply X-ray Diffraction (XRD) is an analytical technique primarily used for phase identification of a crystalline material and can provide information on unit cell dimensions. The analyzed material is finely ground, homogenized, and average bulk composition is determined. X-ray diffraction is based on constructive interference of monochromatic X-rays and a crystalline sample. These X-rays are generated by a cathode ray tube, filtered to produce monochromatic radiation, collimated to concentrate, and directed toward the sample. The interaction of the incident rays with the sample produces constructive interference when conditions satisfy Bragg's Law. This law relates the wavelength of electromagnetic radiation to the diffraction angle and the lattice spacing in a crystalline sample. These diffracted X-rays are then detected, processed and counted. By scanning the sample through a range of 2θ angles, all possible diffraction directions of the lattice should be attained due to the random orientation of the powdered material. Conversion of the diffraction peaks to d-spacings allows identification of the mineral because each mineral has a set of unique d-spacings. Typically, this is achieved by comparison of d-spacings with standard reference patterns [78]. The crystalline form of the sample is a property with important influence in the gas sensing response. For instance, Jiménez et al. reported in their work how different crystal phases of WO_3 show change in sensing properties of this material vs. two target gases, i.e. H_2S and NO_2 [79].

The crystalline structure of SnO_2 samples was characterized using using a PANalytical X'Pert PRO diffractometer (PANalytical B.V., Almelo, Netherlands) instrument located in the Interdepartmental Center for Large Instruments (CIGS) at the University of Modena and Reggio Emilia (UNIMORE). The diffractometer is equipped with a Cu X-ray tube operating at a voltage of 40 kV and a current of 40 mA. An X'Celerator detector was used, which based on RTMS (Real Time Multi Strip Technology) and optimized for Cu $K_{1,2}$ radiation. The data were collected in 10 – 90 °2θ range. The X'Pert HighScore Plus version 2.0 program by PANalytical B.V., coupled with the Powder Diffraction File database (PDF), was used for phase identifications. Profex v. 4.2.1 was used to calculate the cell parameters and the average crystallite size by Rietveld and Le Bail approach [J. Appl. Cryst. (2015). 48, 1573–1580]. The line profile fitting was carried out with the fundamental parameters approach [J. Appl. Cryst. (2015). 48, 1573–1580].

Also, the X-Ray Diffractometer APD 2000 located at FBK was used for structural analysis in this work. In Table 1.4 the main characteristics of the instrument are reported.

Table I. 4: main characteristics of the X-Ray Diffractometer APD 2000 located at FBK.

Instrument	Italstructures
Radiation	Cu Ka 0,15418 nm

Detector	Scintillation counter, NaI (Tl) crystal
Generator	Constant 2KS Italstructures
Bragg-Brentano	Powder analysis
Goebel Mirror	Thin films analysis (20 nm)
Analysis area	mm^2
Detection limit	As a liquid solution in deuterated solvents

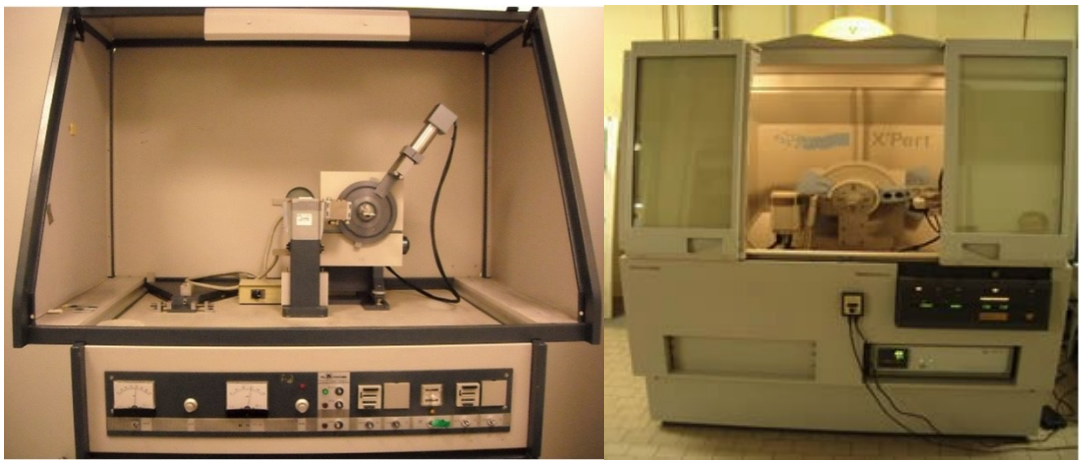

Figure I. 20: X-Ray Diffractometer APD 2000 located at FBK (left) and PANalytical X'Pert PRO diffractometer located at the UNIMORE (right).

1.6.2.2. X-ray Photoelectron Spectroscopy

X-ray Photoelectron Spectroscopy (XPS) is a quantitative spectroscopic technique that allows measurements of the empirical formula, the elemental composition at the parts per thousand range, chemical state and electronic state of the elements that exist within a material. XPS spectra are obtained by irradiating a material with a beam of X-rays while simultaneously measuring the kinetic energy and number of electrons that escape from the top 0 to 10 nm of the material being analyzed. XPS requires usually high or ultra-high vacuum conditions [80].

The XPS can be used to analyze the surface chemistry of a material in its as-received state, or after some treatments. Contrarily, the other analysis techniques proposed in this work, XPS analysis is specific to detect the change in the composition of about the firsts 10 nm of a nano-powder sample. Regarding chemoresistive gas sensors, the processes of greater interest that need a XPS surface analysis to verify the material composition or stability are: exposure to heat to study the changes due to heating; exposure to reactive gases or solutions; exposure to ultraviolet light; decoration of the semiconductor with other nanoparticles (e.g. noble metal nanoparticles) [81].

Elemental identification is possible (except for H and He) for core level photoemission (5-1 at%, the typical detection limit for most elements). Relative elements abundance can be calculated in semi-quantitative or quantitative mode. Information on chemical bonds is derived either from core level shifts or from changes in the VB electronic structure [82].

XPS spectra were recorded using a Kratos AXIS Ultra^{DLD} spectrometer located at Bruno Kessler Foundation (FBK) in Trento-Italy, equipped with an x-ray mono ($Al\ K\alpha$) analysis beam. The Beam Energy was set to 1486.6 eV with an emission angle of 90°. The samples, in powder form, were deposited on a double-sided carbon-based tape fixed on silicon substrates. These substrates were attached to the specimen holder with metal clamps. For each sample, a survey was acquired (in the energy range -2, 1300 eV) to identify the elements present on the sample surface. Then, the core levels O1s, Sn3d and C1s were acquired, with better energy resolution and the VB (-1, 35 eV) at intermediate resolution.

Figure I. 21: Kratos AXIS UltraDLD spectrometer located at FBK.

1.6.2.3. Scanning Electron Microscope – Energy-Dispersive X-ray spectroscopy

A Scanning Electron Microscope (SEM) generates images of a sample by scanning the surface with a focused electron beam. The electrons interact with sample atoms, producing various signals that contain information about the sample surface topography and composition. The electron beam is scanned in a raster scan pattern, and the beam position is linked with the detected signal to produce an image. The last versions of SEM, provided with the least technological development, can achieve resolution better than 1 nanometre.

The most common SEM mode is the detection of secondary electrons emitted by atoms excited by the electron beam. The number of secondary electrons that can be detected depends, among other things, on specimen topography. By scanning the sample and collecting the secondary electrons that are emitted using a special detector, an image displaying the topography of the surface is created. Samples can be observed in high vacuum in conventional SEM, or in low vacuum or wet conditions in variable pressure or environmental SEM, and at a wide range of cryogenic or elevated temperatures by means of specialized instruments [83]. Moreover, the SEM instruments are typically coupled with the Energy-Dispersive X-ray spectroscopy (EDS or EDX), an analytical technique used for the elemental analysis or chemical characterization of a sample.

The study of powder morphology is very important in the chemoresistive gas sensing field. Indeed, it is an evidence in scientific literature that different morphology of the same semiconductor, e.g. nanorods, nanobeads or nanowire, shows great differences in sensing properties. These variations are mainly due to two causes, i.e. different grain size that results in a variation of the semiconductor surface available for interaction with the gaseous molecules, and a percentage change of the depletion layer in the presence of the same gas concentration between two different morphologies. [83].

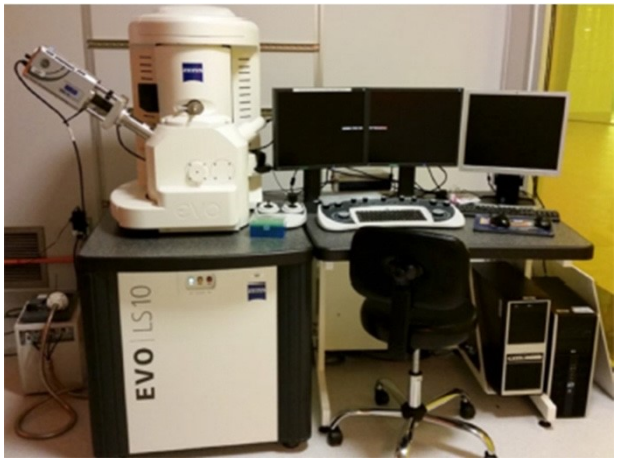

Figure I. 22: SEM instrument located at CNR-Bologna.

1.6.2.4. Transmission Electron Microscopy - Selected Area (Electron) Diffraction

Transmission Electron Microscopy (TEM) allows having an additional morphological information of powders studied in this work. TEM is a microscopy technique in which a beam of electrons is transmitted through a sample to form an image. The specimen is most often an ultrathin section less than 100 nm thick or a suspension on a grid. An image is formed from the interaction of the accelerated electrons with the sample as the beam is transmitted through the specimen. The image is then magnified and focused onto an imaging device, such as a fluorescent screen, a layer of photographic film, or a sensor such as a charge-coupled device.

Transmission electron microscopes are capable of imaging at a significantly higher resolution than other microscope types, owing to the smaller de Broglie wavelength of electrons. This enables the instrument to capture fine details, even as small as a single column of atoms, which is thousands of times smaller than a resolvable object seen in a light microscope.

At lower magnifications, TEM image contrast is due to differential absorption of electrons by the material due to differences in composition or thickness of the material. At higher magnifications, complex wave interactions modulate the intensity of the image, requiring expert analysis of observed images. Alternate modes of use allow for the TEM to observe modulations in chemical identity, crystal orientation, electronic structure and sample induced electron phase shift as well as the regular absorption-based imaging. By using TEM

it is also possible to perform the Selected Area (Electron) Diffraction (SAED), a crystallography technique that information about crystallinity of specific nanometric areas. This is possible because the wavelength of high-energy electrons is a few thousandths of a nanometer, and the spacing between atoms in a solid is about a hundred times larger, the atoms act as a diffraction grating to the electrons, which are diffracted. Some fraction of them will be scattered to specific angles, determined by the crystal structure of the sample, while others continue to pass through the sample without deflection [84]. It is possible to calculate the interplanar distance by means of the formula:

$$d = \lambda \frac{L}{R}$$

where λ is the wavelength of electrons, L is the camera length, R the radius of the diffraction rings and d the interplanar distance.

Figure I. 23: TEM instrument located at CNR Bologna.

1.6.3. Deposition of the material

To be interfaced with the control electronics and to be placed on the substrate, the active material of the sensor must be mixed with other substances in order to obtain a printable paste, which its principal components are:

- The active material (semiconductor oxide)
- The fried
- Organic vehicles.

The active material consists of a nanometric powder of semiconducting nanostructures with an average dimension smaller than 100 *nm*, which must be chosen depending on the type of gas to be detected with the sensor. So, the first step consists of the preparation in the laboratory of the powder. The second step consists of the preparation of the ink, a powder suspension in one or more organic vehicles suitably dosed. Then, to the preparation must be added the fried in small percentages in weight depending on the powder used. The fried is a powder formed by a mixture of glassy oxides based on silica (SiO_2) charged with alkaline earth

oxides or with oxides of the *IV* group, to modify its behavior with temperature. Its function is to fix particles between them and to anchor the paste to the substrate. The first aspect is of fundamental importance in order to form a uniform network of particles and also to obtain intergranular Schottky barriers; the second aspect is practical and is essential so that the film does not detach from the substrate. Organic vehicles are generally made by organic solvents in which are dissolved resins and surfactants in order to optimize the dispersion of solid particles inside the medium and to regulate the viscoelastic behavior for an ideal printing. The organic vehicle is completely removed in the following thermal processes.

The printing of the paste, in the Sensors and Semiconductors laboratory at the University of Ferrara (SSL-UNIFE), on the substrate is carried out with a screen-printing machine (Figure I. 24).

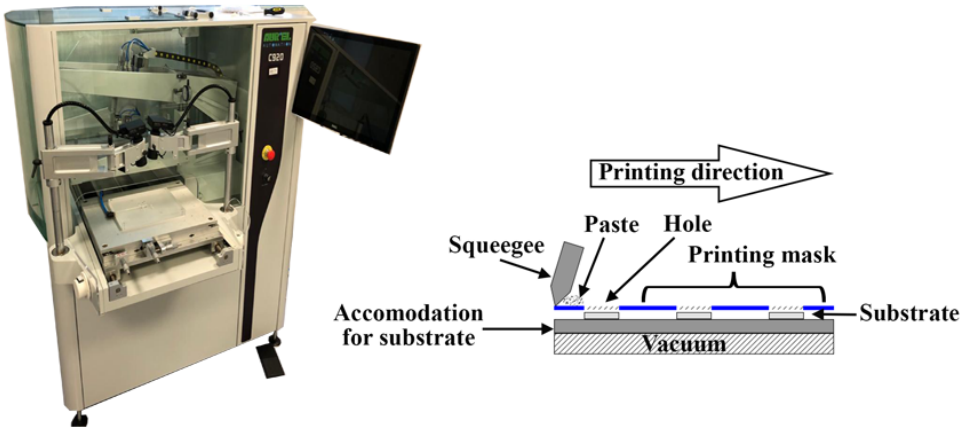

Figure I. 24: Screen printing instrument used in SSL UNIFE (left), lateral simplified section of the machine (right).

The essential components of a screen-printing machine are:

- Printing mask, which shows the geometry of the design to be printed
- Squeegee, a spatula which, exerting pressure, allows the paste to cross the screen and to settle on the substrate, reproducing the design with high quality.

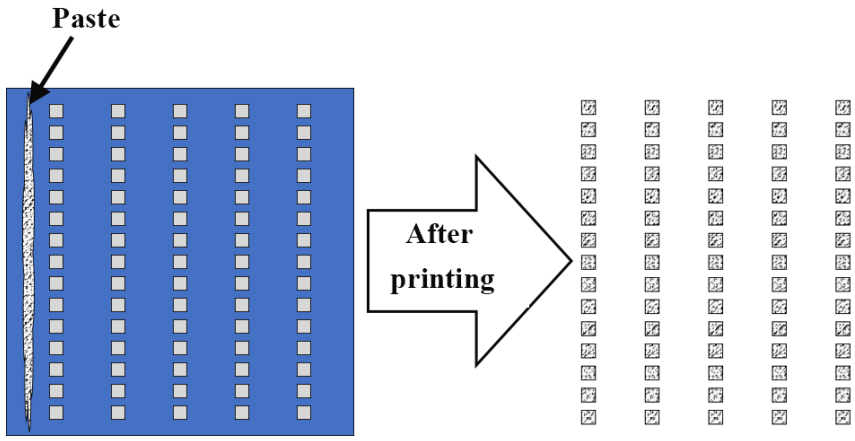

Figure I. 25: Illustration of the squeegee passage on the screen after the application of the photosensitive emulsion and of the paste.

A typical screen consists of a network of finely twisted steel wires (of 100 μm), stretched over a frame of aluminum. As shown in (Figure I. 25), between cables there is an empty space; to characterize a printing screen a specific unit of measure, named mesh should be defined. The mesh number corresponds to the number of wires per linear inch that can be calibrated as a function of the required application. The cable network is covered by an UV-sensitive emulsion, on which is impressed photographically the design to be printed. Moreover, the screen presents some areas in which the emulsion is absent, through which the paste can be printed on the substrate. So, the function of the printing screen is to define the design and to calibrate the quantity of paste. The paste must be a pseudo-plastic fluid, which varies its viscosity as a function of the applied stress. The squeegees must be resistant to solvents involved in the process and present in the paste. They are two: the first one forces the paste through the screen, the second one works in the opposite direction and reports the paste in the initial position for a new print.

1.6.4. Drying and Firing

Once printed, the ink undergoes two different thermal treatments that are the drying and the firing in order to improve the cohesion among the nanostructures in the sensing layer, and also an enhancement in the cohesion of the last with the substrate. In addition, the drying is a low-temperature treatment, around 100-150 °*C* that serves to eliminate the most volatile organic solvents and to avoid the draining of the printed ink. It can be done in a common airy hotplate or in an infrared oven.

The firing is a high-temperature process (up to 850 °*C*) made in a muffle furnace or in an infrared oven. It serves to eliminate all organic additives used to obtain the ink and to leave on the substrate only the film composed by the functional material and by the small percentages of fried. During these two processes, the temperature must be rigorously controlled in order to limit the formation of cracks on the handwork, that may prejudice conductive phenomena through the material.

1.6.5. Packaging of the sensor

The sensor must be assembled by means of a technique named bonding, which consists in the connection of the sensor to a support, using four pins. These pins are welded, by thermo-compression, to the heater and to the contacts of the plate on which the film is deposited.

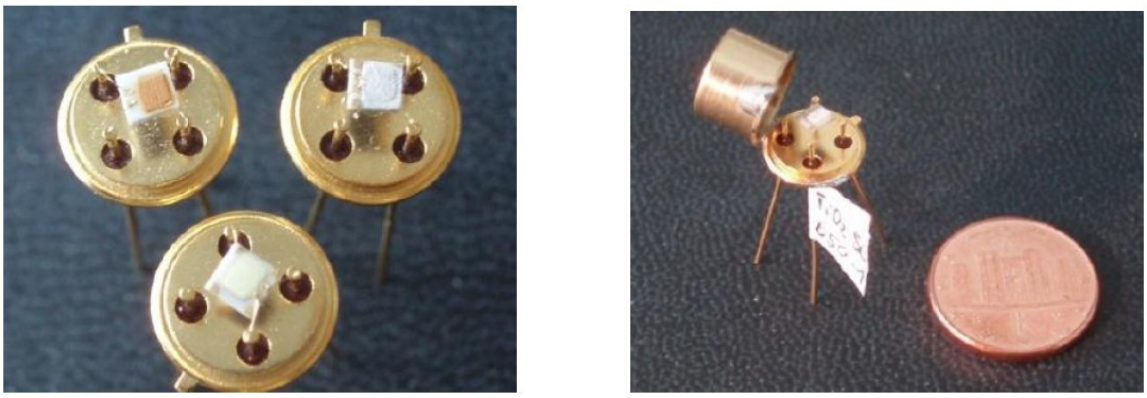

Figure I. 26: Bonded sensors (left) and comparison between a sensor and a 1cent money (right).

This connection, powered by golden wires (99:99%) with a diameter of 0.06*mm*, is carried out via the apparatus shown in Figure I. 26.

Figure I. 27: Instrument for the packaging of sensors used in SSL (UNIFE).

1.6.6. Experimental setup for gas sensing measurements

In the sensors and semiconductors laboratory at the university of Ferrara, the experimental setup for gas sensing measurements (electrical characterization) consists mainly of:

- Gas source
- Mixing system
- Gas chamber
- Data acquisition system

These components are reported in Figure I. 28 and it is also showed how they are interfaced with each other in order to study sensing responses of gas sensors used, depending on the type and concentration of the gas mixture introduced into the gas-sensing chamber.

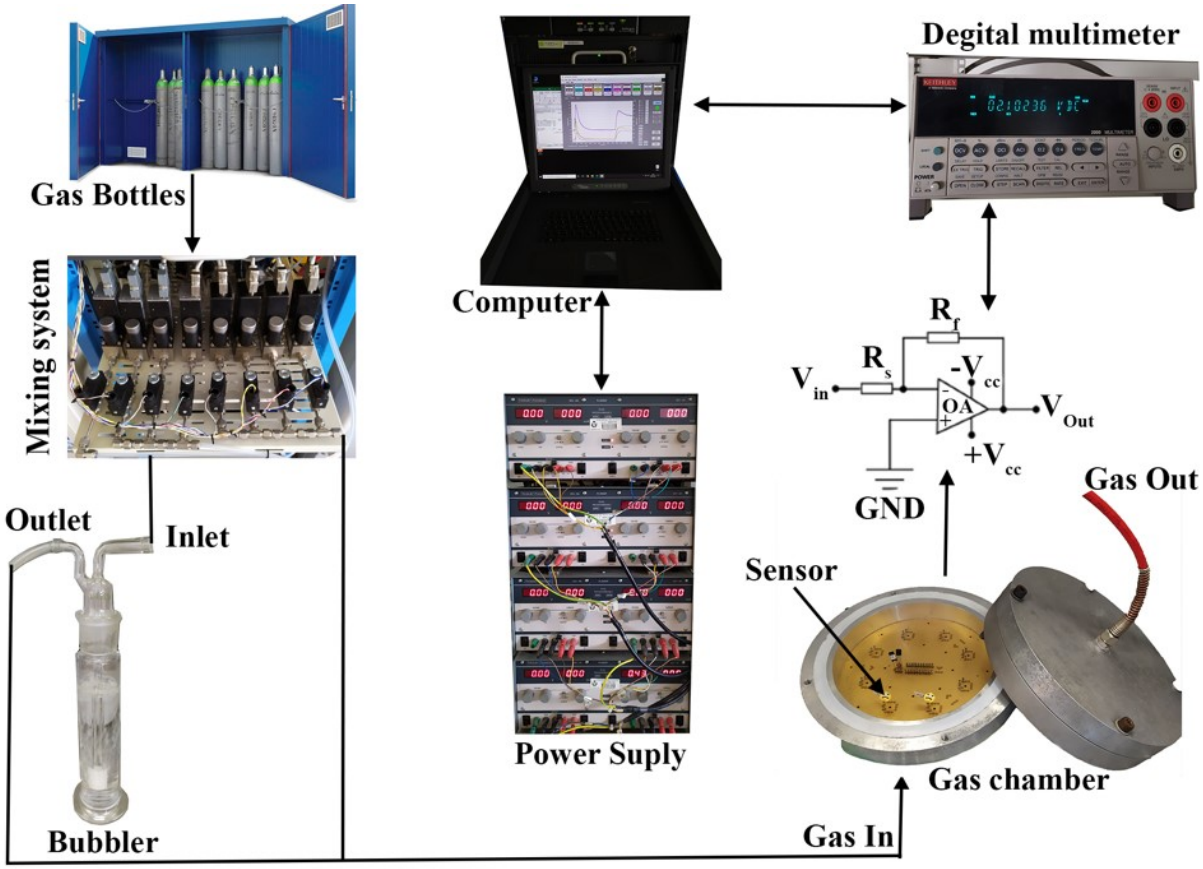

Figure I. 28: Experimental setup for gas sensing measurements used in the SSL at the UNIFE.

In the following paragraphs a detailed discussion of the individual components reported in the Figure I. 28 is given.

1.6.6.1. Flow meters for gas mixing

Masse-flow meters (Mixing system) are necessary to set the gas flow that one needs to measure. The target gas to be studied is usually contained in gas certified cylinders (gas source). The role of the flow meters is to set the flow and then send it to the gas chamber, where the sensors are placed, through Teflon tubes that connect the mixing system and the gas chamber.

The desired flow can be calculated using the following relation:

$$F(sccm) = \frac{F_{tot}(sccm).C(x)}{C_c(x)} \qquad \text{Eq. I. 22}$$

where F_{tot} depends on the design of the gas chamber, it is the total flux that one can inject in the chamber (chamber volume). In the sensors and semiconductors laboratory at

UNIFE, 500 standard cubic centimeters per minute ($sccm$) is used; $C(x)$is the gas concentration to be measured, usually its unit is part per million (ppm); $C_c(x)$ is the gas concentration in the bottle given by the seller company.

1.6.6.2. Gas sensing chamber

The test chamber used in this study (Sensors and Semiconductors Laboratory) for the electrical characterization of chemoresistive gas sensors, has a cylindrical shape (Figure I. 29). and it is made of Aluminum and hermetically isolated by a cap through screws.

Eight sensors can be tested, humidity and temperature sensors can be monitored in the chamber. The sensor support has four connections that are used to give a voltage to the two electrical circuits of the substrate (the heater and the electrodes).

It is important to specify, on the one hand, that the gas should be distributed uniformly inside the chamber in order to arrive at the sensors surface at the same time, hence the diffuser around which the sensors are positioned is placed in the center of the chamber. on the other hand, it is also necessary to mention that temperature and relative humidity inside the gas-sensing chamber should be regularly controlled, thus humidity and temperature sensors should be placed inside the chamber. In our case, a commercial HIH-4000 Honeywell humidity sensor along with a commercial temperature sensor are employed (Figure I. 29).

It is known that for each kind of sensor (the material used), there is a specific operating temperature. In order to perform electrical measurements with a stable baseline, the sensors are kept at their working temperature for 24 hours for each measurement.

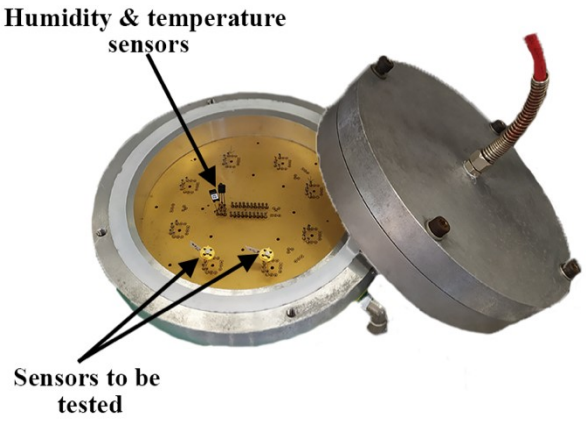

Figure I. 29: Gas chamber used in the SSL at the UNIFE.

1.6.6.3. Electronic system to monitor sensor signals

The sensor to be tested is inserted in an electrical circuit shown in Figure I. 30 and it is represented by R_S (Sensor resistance), in this way the change in the conductance of the sensor can be detected. This circuit is based on an operational amplifier (OA) where the input signal is connected to the negative entry of the amplifier while the positive one is connected to the

ground (*GND*). The V_{in} and V_{out} voltage values are respectively connected to the ends of the sensor resistor R_S and the applied load resistor R_f, therefore:

$$\frac{V_{Out}}{R_f} = -\frac{V_{In}}{R_s} \quad \text{Eq. I. 23}$$

Then the gain is given by:

$$\frac{V_{Out}}{V_{In}} = -\frac{R_f}{R_s} \Rightarrow V_{Out} = -R_f . V_{In} \frac{1}{R_s} \quad \text{Eq. I. 24}$$

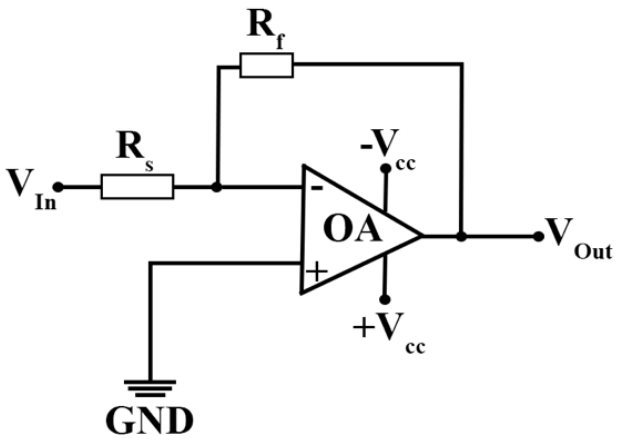

Figure I. 30: electrical circuit used to read the sensor signal.

In this electronic system and by setting V_{in} to -5V, due to the virtual short circuit at the *OA* inputs, the inverting input terminal is at the same potential as the non-inverting input terminal. In this way, the sensor is subjected to a steady potential difference of 5V until the *OA* works away from saturation. As the values of V_{in} and R_f are known and constant, the output voltage V_{out} is then proportional to the conductance G:

$$V_{Out} = K . G \quad \text{Eq. I. 25}$$

where $K = -R_f V_{in}$

If $V_{out}(air)$ *and* $V_{out}(gas)$ are the potentials measured when the sensor is subjected to the air and the gas, respectively. The response expression assumes a simple form, independently of the circuit parameters and it is given as follow:

$$\frac{G(gas)}{G(air)} = \frac{V_{Out}(gas)}{V_{Out}(air)} \quad \text{Eq. I. 26}$$

The gas response for an n-type semiconductor is defined for both reducing and oxidizing gases as follow:

$$R = \begin{cases} \frac{G(gas)-G(air)}{G(air)} & for\ reducing\ gases \\ \frac{G(air)-G(gas)}{G(gas)} & for\ oxidizing\ gases \end{cases} \quad \text{Eq. I. 27}$$

Actually, the sensor consists of two circuits; the one explained in the previous part was the electrodes circuit that is used to measure the change in the sensor conductance. The

second one is used to heat the sensor in order to thermally activate its sensing film, this circuit is called the heater and it is represented in Figure I. 31.

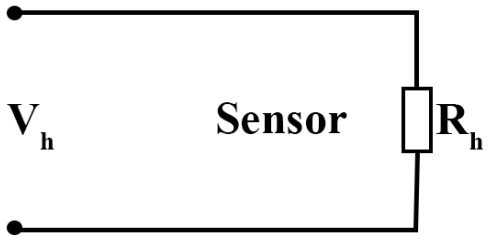

Figure I. 31: representation of the heater circuit used to thermally activate the sensing film.

The heating element is a platinum coil in which the resistance linearly rises with the heat. The temperature and resistance are related by the following formula:

$$R_h = R_0(1 + \alpha T + \beta T^2) \qquad \text{Eq. I. 28}$$

Where R_h is the heater resistance, T is temperature and R_0 is the resistance at 0°C. α and β are two constant characteristics of the material and they depend on the type of material used and the deposition characteristics. Using this relation, one can measure the heater resistance at room temperature and then calculates the constant R_0.

Then knowing R0 and choosing the desired working temperature that one would like to set; it is possible to calculate the heater resistance (Rh) and make the sensor work under the working temperature by applying a voltage Vh to the circuit. Consequently, one can control and directly modify Rh and so the temperature of sensors (modifying the applied voltage (Vh)).

2. Computational method: Ab-initio approaches

The non-relativistic quantum description of a molecular or crystalline system is based on Schrödinger's equation. A mandatory introduction to this theory begins with the presentation of the exact Schrödinger equation (multi-body equation), which will be simplified later by various approximations so that it can be solved. The treatment of this "multi-body problem" in quantum mechanics consists in searching for the solutions of the Schrödinger equation. Unfortunately, the electrons and nuclei that make up materials constitute a strongly interacting multibody system and this makes the solution of the Schrödinger equation extremely difficult.

2.1. Schrödinger equation

In quantum theory, a system consisting of N_e electrons in interactions of $\overrightarrow{r_1}$ ... ..$\overrightarrow{r_{N_e}}$ space coordinates, and N_n nuclei of charge Z and $\overrightarrow{R_1}$ ... ..$\overrightarrow{R_{N_n}}$ space coordinates, is described by the wave function ψ , which satisfies the following time-independent Schrödinger equation:

$$H\psi = E\psi \quad \text{Eq. II. 1}$$

where H is the Hamiltonian of the system, whose eigenvalues refer to the values of the observable total energy E.

The Hamiltonian of the system is given by the following expression:

$$H = T_{el} + T_n + V_{el-el} + V_{el-n} + V_{n-n} \quad \text{Eq. II. 2}$$

where

$$T_{el} = \frac{-\hbar^2}{2m_e}\sum_{i=1}^{N_e}\overrightarrow{\nabla_i}^2 \quad \text{Eq. II. 3}$$

$$T_n = -\frac{\hbar^2}{2M_n}\sum_{a=1}^{N_n}\overrightarrow{\nabla_a}^2 \quad \text{Eq. II. 4}$$

are respectively the kinetic energies of electrons and nuclei

and

$$V_{el-el} = \frac{1}{4\pi\varepsilon_0}\sum_{\substack{i=1\\ j>i}}^{N_e}\frac{e^2}{|\overrightarrow{r_i}-\overrightarrow{r_j}|} \quad \text{Eq. II. 5}$$

$$V_{el-n} = \frac{1}{4\pi\varepsilon_0}\sum_{a=1}^{N_n}\sum_{i=1}^{N_e}\frac{Z_a e^2}{|\overrightarrow{r_i}-\overrightarrow{R_a}|} \quad \text{Eq. II. 6}$$

$$V_{n-n} = \frac{1}{4\pi\varepsilon_0}\sum_{\substack{a=1\\ b>a}}^{N_n}\frac{Z_a Z_b e^2}{|\overrightarrow{R_a}-\overrightarrow{R_b}|} \quad \text{Eq. II. 7}$$

are the energies of electron-electron, electron-nucleus and nucleus-nucleus interactions.

In the Hamiltonian expression of the system, the movements of the electrons and nuclei are coupled and their respective coordinates cannot be treated separately. In case of a system having (N_e + N_n) bodies interacting with ($3N_e$+$3N_n$) degrees of freedom, for which the

analytical and rigorous resolution of the corresponding Schrödinger equation is impossible, some approximations are needed.

In the continuation of this work, in order to simplify the notations, the following atomic units will be adopted:

$$e = \hbar = m_e = 1$$

2.2. Fundamental approximations

2.2.1. Approximation of Born-Oppenheimer

In 1927, Born and Oppenheimer [85] proposed to solve Schrödinger's equation by separating the wave function ψ into two parts, an electronic part and a nuclear one. This approximation is based on the difference in inertia of electrons and nuclei ($m_e \ll M_n$). Therefore, the speed of nuclei is negligible compared to that of electrons (stationary nuclei).

The Hamiltonian of the system becomes:

$$H = H_n + H_e \quad \text{Eq. II. 8}$$

where:

H_n and H_e are the nuclear and electronic Hamiltonian, respectively, which are given by:

$$H_n = -\frac{1}{2}\sum_{a=1}^{N_n}\overrightarrow{\nabla_a}^2 + \sum_{\substack{a=1 \\ b>a}}^{N_n}\frac{Z_a Z_b e^2}{|\overrightarrow{R_a}-\overrightarrow{R_b}|} \quad \text{Eq. II. 9}$$

$$H_e = -\frac{1}{2}\sum_{i=1}^{N_e}\overrightarrow{\nabla_i}^2 + \sum_{\substack{i=1 \\ j>i}}^{N_e}\frac{e^2}{|\overrightarrow{r_i}-\overrightarrow{r_j}|} - \sum_{a=1}^{N_n}\sum_{i=1}^{N_e}\frac{Z_a e^2}{|\overrightarrow{r_i}-\overrightarrow{R_a}|} \quad \text{Eq. II. 10}$$

The motion of the electrons is decoupled from that of the nuclei, and Schrödinger's equation splits into two equations:

Electronic Schrödinger equation,

$$H_e\phi\left(\overrightarrow{r_1}\dots\overrightarrow{r_{N_e}}\right) = E_e\phi\left(\overrightarrow{r_1}\dots\overrightarrow{r_{N_e}}\right) \quad \text{Eq. II. 11}$$

Nuclear Schrödinger equation,

$$H_n\varphi\left(\overrightarrow{R_1}\dots\overrightarrow{R_{N_n}}\right) = E_n\varphi\left(\overrightarrow{R_1}\dots\overrightarrow{R_{N_n}}\right) \quad \text{Eq. II. 12}$$

The wave function $\psi(\overrightarrow{r_1}\dots\overrightarrow{r_{N_e}},\overrightarrow{R_1}\dots\overrightarrow{R_{N_n}})$ of the system can be written as the product of two wave functions:

$$\psi(\overrightarrow{r_1}\dots\overrightarrow{r_{N_e}},\overrightarrow{R_1}\dots\overrightarrow{R_{N_n}}) = \phi\left(\overrightarrow{r_1}\dots\overrightarrow{r_{N_e}}\right)\varphi\left(\overrightarrow{R_1}\dots\overrightarrow{R_{N_n}}\right) \quad \text{Eq. II. 13}$$

where ϕ and φ are the electronic and nuclear wave function, respectively.

Since, in this approximation, the nuclei are considered immobile, the problem is reduced to solving the electronic Schrödinger equation:

$$\left\{-\frac{1}{2}\sum_{i=1}^{N_e}\overrightarrow{\nabla_i}^2+\sum_{\substack{i=1\\j>i}}^{N_e}\frac{e^2}{|\overrightarrow{r_i}-\overrightarrow{r_j}|}-\sum_{a=1}^{N_n}\sum_{i=1}^{N_e}\frac{Z_a e^2}{|\overrightarrow{r_i}-\overrightarrow{R_a}|}\right\}\phi(\overrightarrow{r_1}\dots\overrightarrow{r_{N_e}})=E_e\phi(\overrightarrow{r_1}\dots\overrightarrow{r_{N_e}})$$

Eq. II. 14

The term associated with electron-electron interaction makes the resolution of this equation impossible.

2.2.2. Hartree Approximation

In 1928 it is introduced by Hartree [86] the idea to substitute the interacting N_e electrons system into an independent N_e electrons system, where the principle of the mean-field can be applied: each electron evolves in the effective potential generated by the nuclei and the other electrons. The electron wave function of the system is thus the direct product of the $\phi(\overrightarrow{r_1})$ mono-electronic wave functions.

$$\phi(\overrightarrow{r_i})=\prod_{i=1}^{N_e}\psi_i(\overrightarrow{r_i})\quad\text{Eq. II. 15}$$

The electronic Hamiltonian of the system is therefore written as the sum of the one-electron Hamiltonians:

$$H_e=\sum_{i=1}^{N_e}\left\{-\frac{1}{2}\overrightarrow{\nabla_i}^2+\sum_{j>i}^{N_e}\frac{1}{|\overrightarrow{r_i}-\overrightarrow{r_j}|}-\sum_{a=1}^{N_n}\frac{Z_a}{|\overrightarrow{r_i}-\overrightarrow{R_a}|}\right\}\quad\text{Eq. II. 16}$$

The Schrödinger's equation with a single electron can be solved, instead of solving it with N_e electrons:

$$\left\{-\frac{1}{2}\overrightarrow{\nabla_i}^2+\sum_{j>i}^{N_e}\frac{1}{|\overrightarrow{r_i}-\overrightarrow{r_j}|}-\sum_{a=1}^{N_n}\frac{Z_a}{|\overrightarrow{r_i}-\overrightarrow{R_a}|}\right\}\phi_i(\vec{r})=\varepsilon_i\phi_i(\vec{r})\quad\text{Eq. II. 17}$$

where

$$\left\{-\frac{1}{2}\overrightarrow{\nabla_i}^2+U_i(\vec{r})+V_H^i(\vec{r})\right\}\phi_i(\vec{r})=\varepsilon_i\phi_i(\vec{r})\quad\text{Eq. II. 18}$$

where

$U_i(\vec{r})$, is the external potential of the nuclei, $V_H^i(\vec{r})$ is the mean field of the other electrons called the Hartree potential, that are given by the following expressions:

$$U_i(\vec{r})=-\sum_{a=1}^{N_n}\frac{Z_a}{|\overrightarrow{r_i}-\overrightarrow{R_a}|}\quad\text{Eq. II. 19}$$

$$V_H^i(\vec{r})=\int\frac{\rho_i(\overrightarrow{r'})}{|\vec{r}-\overrightarrow{r'}|}\overrightarrow{dr'}\quad\text{Eq. II. 20}$$

and $\rho_i(\vec{r})$ is the electronic density given by:

$$\rho_i(\vec{r})=\sum_{\substack{j=1\\i\neq j}}^{N_e}\left|\phi_j(\vec{r})\right|^2\quad\text{Eq. II. 21}$$

Since $\rho_i(\vec{r})$, $V_H^i(\vec{r})$ and $\phi_j(\vec{r})$ are interdependent, they cannot be simultaneously calculated (there is no direct method to calculate them).

The wave function given by equation (II.15) does not consider the indistinguishability of electrons nor Pauli's exclusion principle. Pauli showed that for fermions, a spin-orbital must be antisymmetric with respect to an odd permutation of space and spin coordinates.

2.2.3. Hartree-Fock approximation

In 1930, Fock [87] added another idea when he noticed that Hartree's equations neglected a very important term, the exchange term due to the antisymmetric form of the total wave function.

The idea is to rewrite the electronic wave function of the system as a Slater determinant of the mono-electronic wave functions:

$$\phi_e(\overrightarrow{r_1\sigma_1}.....\overrightarrow{r_{N_e}\sigma_{N_e}}) = \frac{1}{\sqrt{N!}}\begin{vmatrix} \psi_1(\overrightarrow{r_1\sigma_1}) & ... & \psi_1(\overrightarrow{r_{N_e}\sigma_{N_e}}) \\ \vdots & \vdots & \vdots \\ \psi_{N_e}(\overrightarrow{r_1\sigma_1}) & ... & \psi_{N_e}(\overrightarrow{r_{N_e}\sigma_{N_e}}) \end{vmatrix} \quad \text{Eq. II. 22}$$

where $\vec{r}$ and $\vec{\sigma}$ are the space and spin variables respectively.

At this stage, Hartree and Fock managed to correct the antisymmetric problem with respect to a permutation of two electrons noticed by Pauli.

Their equations are written in the following form:

$$\left\{-\frac{1}{2}\overrightarrow{\nabla_i}^2 + U_i(\vec{r}) + V_H^i(\vec{r}) + V_x(\vec{r})\right\}\phi_i(\vec{r}) = \varepsilon_i\phi_i(\vec{r}) \quad \text{Eq. II. 23}$$

$V_x(\vec{r})$ is the non-linear and non-local exchange potential added by Fock which is given by its action on a wave function as follows:

$$V_x(\vec{r})\,\phi_i(\vec{r}) = \sum_{j\neq i}^{N_e}\int \overrightarrow{dr'}\frac{\phi_j^*(r')\phi_i(\vec{r})}{|\vec{r}-\vec{r'}|}\phi_j(\vec{r}) \quad \text{Eq. II. 24}$$

Even at this stage of approximation, the numerical resolution of the Hartree-Fock equations remains complicated, because of the non-local term of the exchange potential introduced by Fock.

2.3. Density Functional Theory

The Density Functional Theory [88] expresses ground state properties such as total energy, equilibrium positions and magnetic moments in terms of electronic density $\rho(r)$. The bases of this theory were formulated by Hohenberg, Kohn and Sham [88] [89] [90]. Generally speaking, Hohenberg and Kohn's theorem shows that the total energy of a gas of electrons subjected to any external potential is a unique function of the density of the gas. One can thus obtain the ground state of the system by minimizing the energy relative to the density. The

basic principles can be expressed according to Hohenberg and Kohn by considering a system of interacting electrons subjected to an external potential $V_{ext}(\vec{r})$. The Hamiltonian is then:

$$H = T + V_{ee} + \sum_{i=1}^{N_e} V_{ext}(\vec{r_i}) \quad \text{Eq. II. 25}$$

where T and V_{ee} are the kinetic energy and electron-electron interaction terms, respectively.

In this case, the ground state energy of a system with many interacting electrons placed in an external potential $V_{ext}(\vec{r})$ is a unique functional of $\rho(\vec{r})$:

$$E[\rho] = \int V_{ext}(\vec{r})\rho(\vec{r})d^3r + F[\rho(\vec{r})] \quad \text{Eq. II. 26}$$

where $F[\rho(\vec{r})]$ is a universal functional of the electron density $(\vec{r})$, which contains the kinetic and Coulombic contributions of the energy. The functional $F[\rho(\vec{r})]$ is independent from $V_{ext}(\vec{r})$and it is not exactly known. The term $\int V_{ext}(\vec{r})\rho(\vec{r})d^3r$ represents kernel-electron interactions.

The problem is therefore to determine $F[\rho]$, which is defined as follows:

$$F[\rho(\vec{r})] = T_s[\rho(\vec{r})] + E_H[\rho(\vec{r})] + E_{xc}[\rho(\vec{r})] \quad \text{Eq. II. 27}$$

where:

- $T_s[\rho(\vec{r})]$ is the kinetic energy of non-interacting electron gas,
- $E_H[\rho(\vec{r})]$ is the classic Coulomb interaction energy,
- $E_{xc}[\rho(\vec{r})]$ is the exchange and correlation energy that describes all contributions of *N*-body that are not taken into account in Hartree's approximation. This term is not analytically known. One method to solve this problem is to use the Kohn-Sham formulation and the local density (*LDA*) or generalized gradient (*GGA*) approximations explained in the following paragraphs.

2.3.1. Kohn and Sham equations

Kohn and Sham [90] wrote the energy of the ground state of a system interacting in an external potential V_{ext}in the following form:

$$E[\rho(\vec{r})] = T_s[\rho(\vec{r})] + \int V_{ext}\,\rho(\vec{r})d^3r + \int \frac{\rho(\vec{r})\rho(\vec{r'})}{|\vec{r}-\vec{r'}|} d^3r d^3r' + E_{xc}[\rho(\vec{r})] \quad \text{Eq. II. 28}$$

The last three terms of this equation contain the effective potential given by the equation below:

$$V_{eff}(\vec{r}) = V_{ext}(\vec{r}) + V_H[\rho(\vec{r})] + V_{xc}[\rho(\vec{r})] \quad \text{Eq. II. 29}$$

where:

$V_H[\rho(\vec{r})] = \frac{1}{2}\int \frac{\rho(\vec{r'})}{|\vec{r}-\vec{r'}|} d^3r'$, is the Hartree potential of the electrons

$V_{xc}[\rho(\vec{r})] = \frac{\partial E_{xc}[\rho(\vec{r})]}{\partial \rho(\vec{r})}$, is the exchange and correlation potential.

The Kohn and Sham equations are obtained then when the electron density as the superposition of mono-electronic contributions can be expressed in the form:

$$\rho(\vec{r}) = \sum_{i=1}^{N_e} |\phi_i(\vec{r})|^2 \quad \text{Eq. II. 30}$$

And the equation to solve the problem and find the density $\rho(\vec{r})$that will minimize the energy is given by:

$$H_{KS}\phi_i(\vec{r}) = \left[-\frac{1}{2}\nabla^2 + V_{eff}(\vec{r})\right]\phi_i(\vec{r}) = \varepsilon_i^{KS}\phi_i(\vec{r}) \quad \text{Eq. II. 31}$$

ε_i^{KS} and $\phi_i(\vec{r})$ being respectively eigenvalues and mono-electronic eigenvector functions (known as Kohn-Sham functions).

The expression of the total energy of the ground state of the system is given in the following form:

$$E[\rho(\vec{r})] = \sum_{i=1}^{N_e} \varepsilon_i + \int V_{ext}\,\rho(\vec{r})d^3r + E_H[\rho(\vec{r})] + E_{xc}[\rho(\vec{r})] \quad \text{Eq. II. 32}$$

Equation (II.31) can be considered as a one-particle Schrödinger equation where the external potential has been replaced by the effective potential defined in equation (II.29). All the energy terms and their associated potential presented in this equation can be evaluated, with the exception of the exchange and correlation term. In general, it is not possible to evaluate this term and, therefore, some approximations are necessary.

2.3.2. Approximations for the exchange-correlation function

2.3.2.1. Local Density Approximation (LDA)

The simplest approximation to calculate the exchange and correlation term is the Local Density Approximation [91], or *LDA*. This approximation assumes that the density changes relatively slowly. Therefore, it replaces the exchange and correlation potential at each point in space with that of a uniform gas of interacting electrons. The Local Density Approximation for the exchange and correlation energy is written as follows:

$$E_{xc}^{LDA}[\rho(\vec{r})] = \int \rho(\vec{r})\varepsilon_{xc}^{hom}[\rho(\vec{r})]d^3r \quad \text{Eq. II. 33}$$

where ε_{xc}^{hom}, is the exchange and correlation energy of a homogeneous gas of electrons of constant density.

The *LDA* is often an efficient approximation, even when the density fluctuates significantly. However, while this method generally gives fairly good molecular properties

(geometry), it leads to poor energy data such as binding energies that are too strong, which can result in too short atomic distances. Thus, the lattice parameters are often underestimated [92].

2.3.2.2. Generalized Gradient Approximation (GGA)

The most natural way to improve the *LDA* is to take into account the inhomogeneity of electron density by introducing density gradient dependent terms into the exchange and correlation energy. This improvement is the Generalized Gradient Approximation [93] or *GGA*. In this approximation, the term E_{xc} is written as a function of electron density and its gradient in the following form [94]:

$$E_{xc}^{GGA}[\rho(\vec{r})] = \int \rho(\vec{r}) f_{xc}[\rho(\vec{r}), \nabla\rho(\vec{r})] d^3r \quad \text{Eq. II. 34}$$

where $f_{xc}[\rho(\vec{r}), \nabla\rho(\vec{r})]$, is a function of local density and density gradient.

The generalized gradient approximation has been developed to significantly improve the quality of the *LDA* results, as it gives good results for the binding energies and cell parameters. This has changed the attitude of chemists towards the use of *DFT-GGA* calculations to study the physical-chemical properties of large molecules [95] instead of the traditional Hartree-Fock (*HF*), plus a treatment of correlation effects.

However, the improvement compared to *LDA* is not always systematic because *GGA* sometimes overcorrects *LDA* [96] [97]. Hence the appearance of different parameterizations of the exchange and correlation function [98] [99], e.g. the *GGA* version proposed by Becke [100] Perdew and Wang [101] or *MPW* (Modified Perdew Wang) [102], also the exchange functions *B88*(Backc88) [103], Perdew86 [104], or *PBE* (Perdew Burkc- Ernzerhof) [105] can be cited.

2.4. Calculation methods

To solve the Kohn-Sham equations and then to calculate band structures, there are several methods which are classified into three main types depending on whether they require experimental results or fundamental data:

- Empirical methods, for which calculations require experimental results,
- Semi-empirical methods, for which calculations require both experimental results and fundamental data,
- Ab-initio methods for which calculations require only fundamental data.

In recent years, researchers have developed methods based on theoretical concepts called first-principle methods, including many groups of methods for the resolution of the Schrödinger equation based on the *DFT*. The most used three methods are:

- based on a linear combination of atomic orbitals (*LCAO*) [106] [107], usable, for example, for the "*d*" bands of transition metals,

- derived from orthogonalized plane waves (*OPW*) [107] [108] better adapted to the CB of "*s-p*" character of simple metals,
- augmented plane wave (*APW*) methods [109] and the Green's function method of Korringa, Kohn and Rostoker (*KKR*) [110] [111] applicable to a wider variety of materials.

Table II.1 shows other methods for the resolution of the Schrödinger equation based on DFT and some examples of software implementing these methods numerically. The first column contains the names of the different codes. These names are mostly acronyms and the meanings of these acronyms as well as other information concerning a particular software can be found on the corresponding web site.

The second column indicates the licenses under which each of these codes is available: GPL (General Public License), free, academic or commercial.

The third column gives the method used by each code: in real space which is based on finite difference and finite element methods or use of Kohn-Sham wave function development following basic functions. The main basic functions used are plane waves (Plane waves: PW), Gaussian waves (GTO: Gaussian Type Orbitals) which are types of functions introduced by S.F. Boys in 1950 and that are particularly used in quantum chemistry, atomic orbitals (AO: Atomic Orbitals), wavelets which have been used for about ten years and the LAPW (Linearized Augmented Plane Waves) method. Some codes such as GPAW and SAMSON combine several types of methods. The fourth column gives the programming language with which the corresponding software has been developed. There are four main languages: fortran, C, C++ and Python.

Table II. 1: Most used codes implementing DFT methods numerically

Code	Licence	Basis	Language
ABINIT	Free, GPL	PW	Fortran
BigDFT	Free, GPL	wavelet	Fortran
CASTEP	Academic, commercial	PW	Fortran
CONQUEST	Academic	Grid, Spline	Fortran
CPMD	Academic	PW	Fortran

CP2K	Free, GPl	PW, Hybrid GTO	Fortran
CRYSTAL	Academic, commercial	GTO	Fortran
DIRAC	Academic	GTO	Fortran, C
EPW6	Free, GPL	PW	Fortran
ErgoSCF	Free, GPL	GTO	C++
FLEUR	Free	FP-(L)APW+lo	Fortran
GAMESS	Academic	GTO	Fortran
Gaussian	commercial	GTO	Fortran
GPAW	Free, GPL	PW, Grid, LCAO	Python, C
HORTON	Free, GPL	GTO	Python, C++
JDFTx	Free, GPL	PW	C++
Octopus	Free, GPL	Grid	Fortran, C
Quantum ESPRESSO	Free, GPL	PW	Fortran
SAMSON	Free	Multiple	C++, Python
Siam Quantum	Free, GPL	GTO	C
SIESTA	Free, GPL	LCAO	Fortran
VASP	Academic, commercial	PW	Fortran
WIEN2k	commercial	FP-(L)APW+lo	Fortran, C

All these methods can be classified in 3 main classes:

- Localized basis sets (atom-centered functions)

- Delocalized basis sets (Plan Waves)
- Mixed basis sets could also be considered. Linear Augmented Plane Waves (LAPW) developed by Andersen [112] could be classified in this category.

In this thesis, both PW as implemented in Quantum Espresso code and LAPW implemented in the wien2k were used.

2.4.1. Plane waves basis and Pseudo-potential (PWPP)

To solve the Kohn-Sham equations in this case, the development of wave functions on a $e^{i(\vec{K}+\vec{G}).\vec{r}}$ plane wave basis is used. The standard way to choose the plane wave basis is to consider all plane waves whose kinetic energy is below a certain limit, the cut-off energy (E_{cut}):

$$\overrightarrow{K^2} + \overrightarrow{G^2} \leq E_{cut} \quad \textit{Eq. II. 35}$$

where the cut-off energy is determined for the studied system, with $\vec{G}$ the vector of the reciprocal lattice which is given by the following expression:

$$\vec{G} = M_x\overrightarrow{b_x} + M_y\overrightarrow{b_y} + M_z\overrightarrow{b_z} \quad \textit{Eq. II. 36}$$

In solids, the wave function is defined on the grid of $\vec{K}$-vectors used to describe the reciprocal space. For periodic systems, if the Bravais grating is used for the spatial representation of atoms, the periodicity is translated for any potential by:

$$V(\vec{r} + \vec{R}) = V(\vec{r}) \quad \textit{Eq. II. 37}$$

$\vec{R}$ is the Bravais grating vector given by:

$$\vec{R} = N_x\overrightarrow{a_x} + N_y\overrightarrow{a_y} + N_z\overrightarrow{a_z} \text{ with } \overrightarrow{a_i}\overrightarrow{b_j} = 2\pi\delta_{ij} \quad \text{Eq. II. 38}$$

The cut-off energy will be an adjustable parameter in the calculations that will have to be optimized to make it possible to reconcile a reasonable calculation time and a good estimation of the total energy of the system.

Plane wave basis have the advantage of being complete, i.e. they are mathematically equivalent to the basis of real atomic orbitals when E_{cut} tends towards infinity. The main advantage of this type of basis is in the resolution of Kohn-Sham's equations. By taking the Fourier transform of the Kohn-Sham equations, convolutions of relatively complex mathematical forms in real space become much simpler products to manipulate in reciprocal space, which allows a fast processing. On the other hand, the optimization of such bases is very simple: only one parameter has to be adjusted to improve the convergence of the total energy. However, as soon as the number of *N* atoms in a system increases, the computation time quickly becomes excessive. Typically, the computational time to solve Kohn-Sham

equations evolve as N^{2-3}. Consequently, the size of current systems calculated using such bases rarely exceeds 150 or 200 atoms.

❖ The pseudopotentials

The electrons of an atom can be divided into two groups: core electrons and valence electrons. Core electrons are the electrons from the electronic layers with the lowest energy. Very localized, they are strongly bound to the nucleus of the atom. They are consequently little affected by the chemical environment of the atom and participate little or not at all in the chemical bonds or the cohesion of the solid. On the other hand, they are responsible for most of the computational costs. In the pseudopotential approximation, the coulombian potential of the nucleus and the core electrons is fixed (it is the frozen-core approximation) and replaced by an effective potential that acts on the valence electrons. The pseudopotentials are constructed by taking into account the physics of the core electrons and consequently by solving Kohn-Sham's equations for core electrons. There are several types of pseudopotentials used in numerical computations, each with its own characteristics. For example, the norm-conserved pseudopotentials introduced by Hamman et al. and then generalized by the Troullier and Martins method, or the ultra-soft pseudopotentials introduced by Vanderbilt and the dual-space pseudopotentials introduced by Goedecker et al. In this work, ultra-soft pseudopotentials imposed by the Quantum Espresso code were used.

Norm-conserved pseudopotentials

This family corresponds to pseudo-potentials known as conserved normals (the corresponding pseudo wave function is normalized). These modern pseudo-potentials are constructed according to a method proposed by Hamann, Schluter and Chiang and systematized by Bachelet et al.

These pseudo-potentials are obtained from a DFT calculation for the free atom without the need for spectroscopic terms. This is why they are called "ab initio" pseudo-potential models. It will be retained that it is the pseudo wave function that is parameterized from the outset and that the pseudo-potential is ultimately obtained by inversion of the radial Schrödinger equation. Refinements to the method were introduced later [Vanderbilt, 1990; Troullier and Martin, 1991].

Ultra-soft pseudopotentials

In practice, the generation of a pseudopotential with conservation of the norm having a low kinetic cut-off energy is not always possible, especially for elements such as atoms of the first lines of the periodic table and elements with *d* or *f* electrons. Transition metals, alkalis and alkaline earths, for which the explicit treatment of the intermediate (semi-core states) as valence states is generally indispensable, lead to pseudopotentials that are hard and have a low transferability. The solution to this problem was proposed by Vanderbilt thanks to the so-called

ultrasoft pseudopotentials, for which the conservation constraint of the standard is removed, and then generalized by Bloch through the approach of Projector Augmented Waves (PAW) in 1990. Vanderbilt has introduced a new approach in which the pseudo wave functions are constrained to be equal to the functions of all-electron waves beyond, as in the concept of conservation of the standard, but are as soft as possible inside. In order to allow this last point, the conservation of the norm is abandoned. Large r_c values can then be used, and consequently, the plane wave cut-off radius needed for calculations can be considerably reduced.

The use of ultrasoft pseudopotentials makes it possible to reduce the number of plane waves necessary for calculations and consequently to preserve a reasonable calculation time.

2.4.2. The Full-Potential Linearized Augmented Plane Wave Method (FP-LAPW)

The *LAPW* (linearized augmented plane wave) method, developed by Andersen [112], is basically an improvement of the augmented plane wave (*APW*) method developed by Slater [109] [113]. A new technique for solving the Poisson equation [114] has been added to the *LAPW* method so that molecular adsorption on surfaces can be treated. The *LAPW* method, which ensures the continuity of the potential on the surface of the muffin-tin sphere, develops the potential in the following form:

$$V(r) = \begin{cases} \sum_{lm} V_{lm}(r) Y_{lm}(r) & inside\ the\ sphere \\ \sum_K V_K e^{iKr} & outside\ the\ sphere \end{cases} \qquad \text{Eq. II. 39}$$

This is the origin of the name of the *FP-LAPW* method "full-potential *LAPW*". Thus, before describing the *FP-LAPW* method, the basics of the *APW* method will be recalled.

❖ APW method

Slater explains the *APW* (Augmented Plane Wave) method in his paper [113]. In the vicinity of an atomic nucleus, the potential and the wave functions are of the Muffin-Tin (*MT*) form with spherical symmetry inside the *MT* sphere of radius R_α. Between atoms the potential and wave functions can be considered as smooth. Consequently, the wave functions of the crystal are developed in different bases according to the region considered: radial solutions of the Schrödinger equation inside the *MT* sphere and plane waves in the interstitial region (*Figure II. 1*).

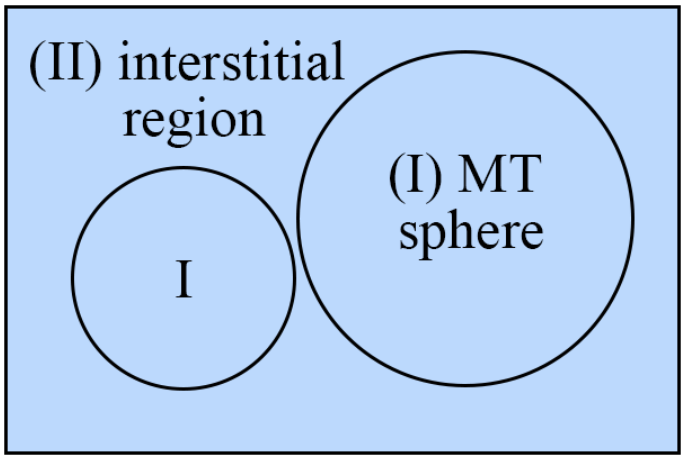

Figure II. 1: Unit cell repartition into atomic spheres (I) and into an interstitial region (II).

Then, the wave function $\phi(r)$ is of the form:

$$\phi(r) = \begin{cases} \sum_{lm} A_{lm} U_l(r) Y_{lm}(r)\,;\ r < R_\alpha \\ \frac{1}{\Omega^{1/2}} \sum_k C_k e^{i(k+K)r}\,;\ r > R_\alpha \end{cases} \quad \text{Eq. II. 40}$$

where R_α represents the radius of the sphere *MT*, Ω the volume of the cell, C_k and A_{lm} the coefficients of the development in spherical harmonics Y_{lm}.

The function $U_l(r)$ is a regular solution of Schrödinger's equation for the radial part which is written as:

$$\left(-\frac{d^2}{dr^2} + \frac{l(l+1)}{r^2} + V(r) - E_l\right) r U_l(r) = 0 \quad \text{Eq. II. 41}$$

$V(r)$ represents the Muffin-Tin potential and E_l the linearization energy. The radial functions defined by the equation (II.37) are orthogonal to any core state. This orthogonality disappears at the limit of the sphere [112] as shown by the following Schrödinger equation:

$$(E_2 - E_1) r U_1 U_2 = U_2 \frac{d^2 r U_1}{dr^2} - U_1 \frac{d^2 r U_2}{dr^2} \quad \text{Eq. II. 42}$$

where U_1 and U_2 are radial solutions for E_1 and E_2 energies. The recovery is constructed using equation (II.38) and integrating it in parts.

Slater justifies the particular choice of these functions by noting that plane waves are solutions of the Schrödinger equation when the potential is constant. As for radial functions, they are solutions in the case of a spherical potential, when E_l is an eigenvalue.

This approximation is very good for materials with a face-centered cubic structure and becomes progressively less satisfactory as the symmetry of the material decreases.

To ensure the continuity of the function $\phi(r)$ on the surface of the MT sphere, the A_{lm} coefficients must be developed according to the C_k coefficients of the plane waves existing in the interstitial regions. Thus, after some algebraic calculations, the A_{lm} coefficients can be expressed as follow:

$$A_{lm} = \frac{4\pi i^l}{\Omega^{1/2} U_l(R_\alpha)} \sum_k C_k j_l(|K+g|R_\alpha) Y_{lm}^*(k+K) \quad \text{Eq. II. 43}$$

The origin is taken at the center of the sphere, and the A_{lm} coefficients are determined from those of the plane waves C_k. The E_l energy parameters are called the variational coefficients of the *APW* method. The individual functions, labeled by k become compatible with the radial functions in spheres, and augmented plane waves (*APWs*) are then obtained.

The *APWs* functions are solutions of Schrödinger's equation in spheres, but only for E_l energy. Consequently, the$E_l$energy must be equal to that of the k-index band. This means that the energy bands (for a K-point) cannot be obtained by a simple diagonalization, and that it is necessary to treat the secular determinant as a function of energy.

The *APW* method presents some difficulties related to the function $U_l(R_\alpha)$ which appears in the denominator of equation (II.39). Indeed, depending on the value of the parameter E_l, the value of $U_\alpha(R_\alpha)$ can become zero on the surface of the *MT* sphere, leading to a separation of the radial functions from the plane wave functions. In order to overcome this problem, several modifications to the *APW* method have been made, notably those proposed by Koelling [115] and Andersen [112]. The modification consists in representing the wave function $\phi(r)$ inside spheres by a linear combination of the radial functions $U_l(R_\alpha)$ and their derivatives with respect to the energy $\dot{U}(r)$, thus giving rise to the *FP-LAPW* method.

❖ The FP-LAPW method

In the *FP-LAPW* method, the basic functions in *MT* spheres are linear combinations of the radial functions $U_l(R_\alpha)Y_{lm}(r)$ and their derivatives $\dot{U}Y_{lm}(r)$ with respect to energy. The U_l functions are defined as in the *APW* method and the function $\dot{U}(r)Y_{lm}(r)$ must satisfy the following condition:

$$\left(-\frac{d^2}{dr^2} + \frac{l(l+1)}{r^2} + V(r) - E_l\right) r\dot{U}_l(r) = rU_l(r) \quad \text{Eq. II. 44}$$

In the non-relativistic case, these radial functions U_l and $\dot{U}_l$ ensure, on the surface of the *MT* sphere, the continuity with the plane waves from the outside. Then, the wave functions thus augmented become the basic functions (*LAPWs*) of the *FP-LAPW* method:

$$\phi(r) = \begin{cases} \sum_{lm}\left[A_{lm}U_l(r) + B_{lm}\dot{U}_l(r)\right]Y_{lm}(r)\,;\; r < R_\alpha \\ \frac{1}{\Omega^{1/2}}\sum_k C_k e^{i(k+K)r}\,;\; r > R_\alpha \end{cases} \quad \text{Eq. II. 45}$$

where the coefficients B_{lm} correspond to the function $\dot{U}_l$ are of the same nature as the coefficients A_{lm}. *LAPWs* functions are plane waves only in the interstitial zones as in the *APW* method. Inside spheres, *LAPWs* functions are better adapted than *APWs* functions. Indeed, if E_l differs slightly from the band energy E, a linear combination will reproduce the radial function better than the *APWs* functions. Therefore, the E_l function can be developed according to its derivative $\dot{U}_l$ and the E_l energy.

$$U_l(E,r) = U_l(E_l,r) + (E - E_l)\dot{U}_l(E,r) + 0((E - E_l)^2) \quad \text{Eq. II. 46}$$

where $0((E - E_l)^2)$ represents the root mean square error.

The *FP-LAPW* method thus ensures the continuity of the wave function on the surface of the *MT* sphere. But, with this procedure, the calculations lose in precision, compared to the *APW* method which reproduces the wave functions very correctly, whereas the *FP-LAPW* method leads to an error on the wave functions of the order of $(E - E_l)^2$ and another on the band energies of the order of $(E - E_l)^4$. In spite of this order of error, the *LAPWs* functions form a good basis which allows, with a single E_l, to obtain all the VBs in a large energy region. When this is not possible, the energy region can usually be divided into two parts, which is a simplification compared to the *APW* method. In general, if U_l is equal to zero at the surface of the sphere, its derivative $\dot{U}_l$ will be different from zero. Therefore, the problem of continuity at the surface of the sphere *MT* will not occur in the *FL-LAPW* method.

Takeda and Kubler [116] have proposed a generalization of the *LAPW* method in which *N* radial functions and their (*N-1*) derivatives are used. Each radial function has its own U_{li} parameter so that the error due to linearization is avoided. The standard *FP-LAPW* method is used for *N=2* and U_{l1} close to U_{l2}, while for *N>2* the errors can be reduced. Unfortunately, the use of high-order derivatives to ensure convergence requires much more computational time than in the standard *FP-LAPW* method. Singh [117] has modified this approach by adding local orbitals at the base without increasing the cutoff energy of plane waves.

2.5. Overview on codes used in this work

The ab-initio computation methods, based on the density functional theory, are implemented by several computer codes of which we mention: Wien2k [118], Quantum espresso [119], VASP (The Vienna Ab initio Simulation Package) [120] [121], SIESTA (Spanish Initiative for Electronic Simulations with Thousands of Atoms) [122] [123] ...

In this thesis both Quantum espresso (or PWSCF) and Wien2k codes were used that are based on the Plane Waves and the Full-Potential Linearized Augmented Plane Wave (*FP-LAPW*) method, respectively. In the following paragraphs, an overview on both codes is listed where a general description and the calculation procedure are given.

2.5.1. Wien2k code

- ❖ General description of the code

The Wien2k simulation code was developed at the Institute of Materials Chemistry (*IMC*) at the Technical University of Vienna and published by P. Blaha and his contributors in Journal of Chemical Physics in 2020 and runs on a UNIX (or LINUX) platform.

In the years that followed, the code underwent several modifications and revisions and each version of the code was named according to the year of publication (WIEN93, WIEN95 and WIEN97). The version that appeared in 2000 was called Wien2k.

The Wien2k package is based on the linearized augmented plane wave methods within the theory of density functionalism. It is composed of two parts:

- Independent programs written in Fortran90
- C-shell scripts that link the Fortran programs.

The version of Wien2k used in this work was the Wien2k_19.1, which was released on June 13, 2019 and which uses FP-LAPW methods. This version of Wien2k has a graphical interface called "w2web" (which means Wien to web).

The Wien2k calculation code is widely used in condensed matter physics as well as in quantum chemistry. It can be used to calculate the physical-chemical properties of materials such as:

- Electronic properties: band structure, density of state and electronic density,
- The total energy (to do the optimization of structures and geometrical relaxation),
- Magnetic properties (magnetic moment) and spin polarizations,
- X-ray emission and absorption spectra,
- Optical properties (refractive index, reflection index...),
- Thermodynamic properties (enthalpy...) …

❖ Calculation procedure

There are two main steps to do calculations using Wien2k code. *Figure II. 2* represents schematically the flowchart of the code. A brief explanation of each step and the programs that make it up is given below (Detailed explanation and description of the calculation procedure can be found in the user guide of the code [122]).

▪ Initialization

It consists of executing a series of small auxiliary programs that will produce inputs for the main programs. The different initialization programs, included in the Wien2k_19.1 version, are:

- *NN*: is a subroutine that calculates the distances between the nearest neighbors up to a specified limit (defined by a distance factor *F*, usually taken equal to 2) and thus helps to determine the value of the radius of the atomic sphere. In addition, it controls the overlapping of atomic spheres. The output file of this subroutine is called: case.outputnn.
- *SGROUP:* determines the space group and the point group of the given structure. The output file is called: case.struct_sgroup.

- *SYMMETRY:* generates the symmetry operations of the space group from the file case.struct, as well as the point group of the different atomic sites. It also generates the *LM* expansion for the spherical harmonics (in the file case.in2.st), as well as the local rotation matrices (in the file case.struct_st).
- *LSTART:* produces the electron densities of the free atoms and determines how the different orbitals are treated in band structure calculations (i.e.: as band states (valence states + half-core states) or core states, with or without the local orbitals, ...). In addition, this subroutine requires to specify the exchange-correlation potential (*LDA* or *GGA*) and the cut-off energy (*cut-off*) that separates the core states from the valence states (usually taken equal to -6 Ry).
- *KGEN:* generates a *k*-point mesh in the Irreducible Brillouin Zone (*IBZ*). One must specify the number of *k*-points in the whole Brillouin (*BZ*).
- *DSTART:* produces an initial density for the *SCF* (Self Consistent Field) cycle by superimposing the atomic densities generated by the *LSTART* subprogram.

▪ SCF calculation

After the creation of all the necessary input files, the *SCF* calculation is carried out, which consists in achieving the convergence of the energy, the density and the potential. The *SCF* cycle is used to execute the following subprograms:

- *LAPW0* (Potential): generates the potential from the density. It generates the *scf* file "case.scf0".
- *LAPW1* (Bands): calculates the VBs. This calculation is done through the calculation of the eigenvalues of the energies and the eigenvectors by the diagonalization method of the matrix. The results are saved in the file case.vector. It also generates the *scf* file "case.scf1". It is this subroutine that consumes most of the calculation time (about 75 %).
- *LAPW2* (Density): calculates the valence densities from the eigenvectors, as well as the Fermi energy. It generates the *scf* file "case.scf2".
- *LCORE*: determines the energies and states of the core. It generates the *scf* file "case.scfc".
- *MIXER*: adds the initial and final density to use the total density as the initial density for the next iteration. It generates the *scf* file "case.scfm".

After the end of the first iteration and the start of the second iteration of the *scf* cycle, the total *scf* file "case.scf" is generated which contains the basic information such as: total energy, volume, density, etc.

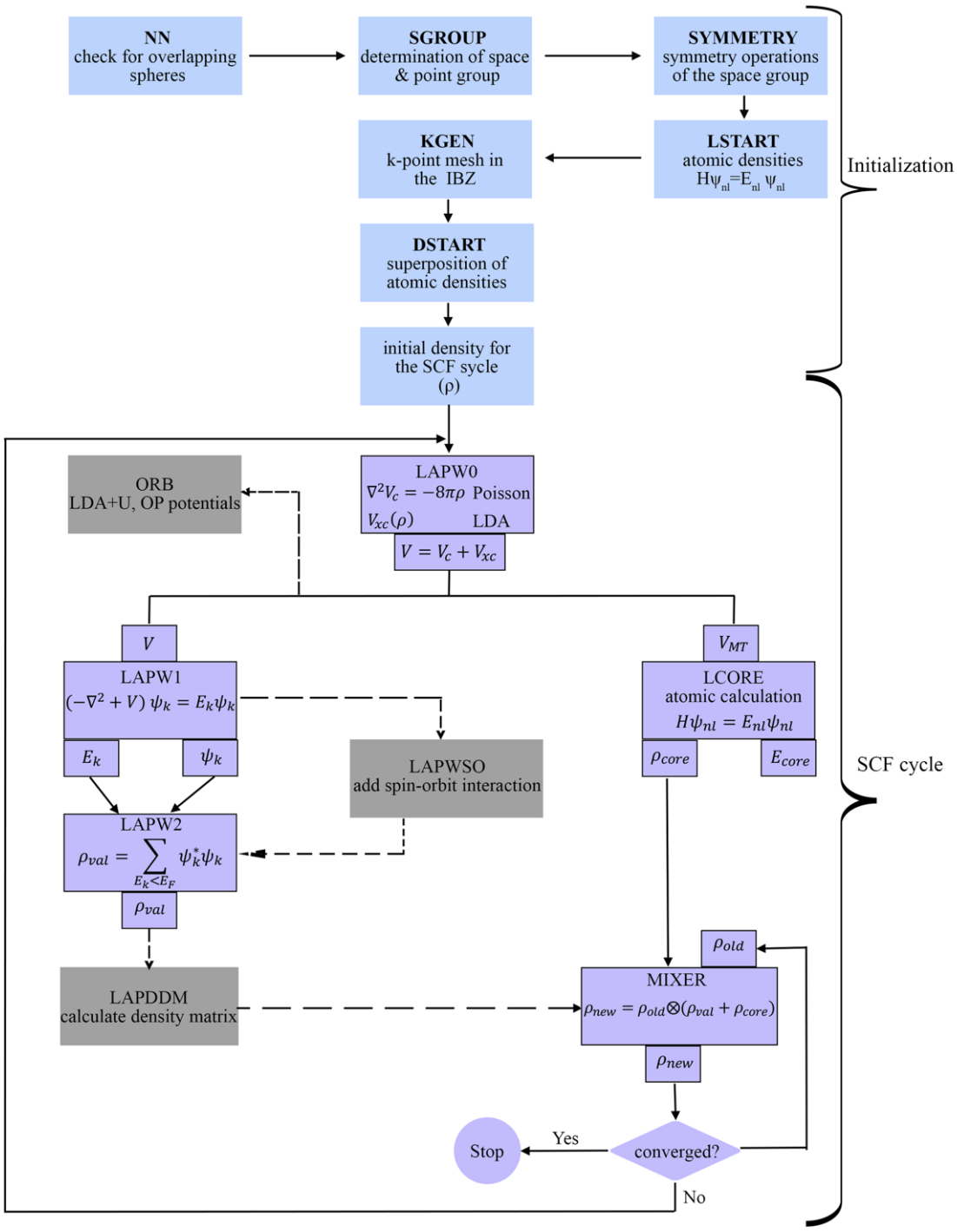

Figure II. 2: Flow chart of Wien2k code.

2.5.2. Quantum espresso

Quantum ESPRESSO is a suite of calculation codes for electronic structures and material modelling. It is based on the density functional theory, a basis of plane waves and pseudo-potentials.

This suite of codes is built around the use of periodic boundary conditions to deal with crystalline systems. Finite systems are also processed using super-cells.

Quantum ESPRESSO can be used for both metals and insulators. Atomic cores can be represented by norm-conserving pseudo-potentials (NCPPs), Ultrasoft (USPPs). Several

exchange-correlation functions are available (LDA, GGA, or more advanced Hubbard U corrections, meta-GGA and hybrid functions).

❖ ***What can PWscf do***

The PWscf performs many types of self-consistent calculations of the properties of electronic structures within the framework of the DFT, using a basic set of plane waves (PW) and pseudopotentials (PP). In particular, some of the basic simulations that can be performed with Quantum ESPRESSO are cited and they include:

- ground state energy and electron orbits (Kohn-Sham), atomic forces, constraints
- structural optimization, also with variable cell
- molecular dynamics at the Born-Oppenheimer surface, also with variable cell
- macroscopic polarization and finite electric fields by modern polarization theory (Berry phases)
- the modern theory of orbital magnetization
- calculation of the free energy zone at the fixed cell by meta-dynamics, if patched with PLUMED
- efficient screening medium method (ECM)
- the self- consistent continuous solvation model (SCCS), if patched with ENVIRON.

All of the above works for both insulators and metals, in any crystal structure, for many exchange correlation (XC) functions (including spin polarization, DFT + U, meta-GGA, non-local and hybrid functions), for the norm conserved (Hamann -Schluter-Chiang) PP (NCPP) in separable form or Ultrasoft (Vanderbilt) PP (USPP) or Projector Augmented Waves (PAW) method. Non-collinear magnetism and spin-orbite interactions are also used. An implementation of finite electric fields with a sawtooth potential in a supercell is also available.

The self-consistent calculations are performed using the Pwscf algorithm; this implements an iterative approach to achieve convergence, using at each step a diagonalization technique, within the framework of the pseudo-potential and plane wave method.

The algorithm implements the pseudo-potentials with conserved standard and ultrasoft but also the PAW (projector augmented waves) method. For the exchange-correlation potential, PWscf can use both GGA and LDA, including spin polarization and treatment of non-collinear magnetism, such as magnetism induced by relativistic effects (spin-orbit interaction) or in the presence of complex magnetic interactions (e.g. the presence of frustration). Convergence is obtained using Broyden's method, the sampling of the Brillouin Zone (BZ) by taking special directions for the K-points, provided in the input file, or calculated from a uniform starting grid. Crystal symmetries are automatically detected and exploited to

simplify and reduce calculation costs. Structural optimization (relaxation) can be performed using the Broyden_Fletcher_Goldfarb_Shanno (BFGS) algorithm, and may involve atomic coordinates, shape and size of the primitive cell.

3. Impact of oxygen vacancies on the physical chemical properties of SnO_2: DFT investigation

Parts of this section were published in [124].

Nowadays, the use of computational Density Functional Theory (DFT) to compute the chemical and physical properties of nanostructured materials and heterogeneous interactions (solid-gas) has nowadays turned out to be crucial, both to study the properties of technologically advanced nanomaterials and to go beyond the limits of experimental characterizations. The objective of this part of the work is to study the impact of the concentration of oxygen vacancies inside tin dioxide (SnO_2) on its physical and chemical properties. SnO_2 is a typical *n*-type semiconductor material with a large bandgap of 3.6 eV [77] [125]. SnO_2 has been the focus of many researchers because of its wide range of physical and chemical properties. It has been used in several domains such as optoelectronic devices, electrocatalysis, ceramics and gas sensors [126] [127] [128]. In fact, it is the most investigated semiconductor as a sensing material for the production of chemoresistive gas sensors [129]. Therefore, it represents the best candidate for the innovative work proposed here.

In this section, *DFT* was used to calculate the physico-chemical properties of the considered material and to study the impact of oxygen vacancies on these properties. For this purpose, two defective samples were constructed, namely Sn_6O_{11} and Sn_6O_{10} which are equivalent to $SnO_{1.83}$ and $SnO_{1.67}$, respectively. These samples were generated on the basis of the SnO_2 rutile unit cell and by creating a *1*1*3* supercell. *GGA* parameterized *PBE* (Perdew-Burke-Ernzerhof) [105] was used for the relaxation of the structures used in this part of the work, and *GGA_PBE* for solids (*GGA-PBEsol*) [130] was used for the optimization of structural properties. This approximation demonstrated, in addition to the *LDA*, its capacity to accurately describe the structural properties of materials. Nevertheless, their applications underestimate the bandgap energy of materials compared to experimental results [131] [132]. In order to improve the results regarding the band gap energy, the modified Becke-Johnson exchange potential model of Tran-Blaha (*TB-mBJ*) [133] has been applied. This approximation proved its ability to predict the bandgap of materials [134]. A series of first principles studies has been performed using the *FP-LAPW* (Full Potential Linearized Augmented Plane Wave) method [135] in the framework of *DFT* as being implemented in the Wien2k code [118]. It is the most efficient method to solve the Khon Sham equation [90].

3.1. Computational details & models

One of the most accurate methods for computing the electronic structure of materials is the *FP-LAPW* method in the context of *DFT* [136]. In most cases, Self-Consistent Field (*SCF*) cycles have been performed using *GGA* and *LDA* approximations to solve the Khon and

Sham equation in order to calculate the electronic structure of materials. In this work, *SCF* cycles were first carried out using *GGA-PBE* approximation for structural relaxation and *GGA_PBEsol* approximation for structural properties computations, and then *TB-mBJ* calculations were executed to obtain the electronic and electrical properties. For the latter, the transport theory of Boltzman was used [137] as implemented in the BoltzTrap2 software package [138].

The rutile unit cell of SnO_2 (Figure III. 1) used in this work has the space group P42/mnm (*N°. 136*), with the initial cell parameters *a=b= 4.7367* and *c= 3.1855* [139]. The tin atoms are positioned in *(0,0,0), (1/2, 1/2, 1/2,)* and those of oxygen are in ± *(u, u, 0);* ± *(1/2+u,1/2-u,1/2)* with the internal parameter *u=0,3070*. This structurewas used for the determination of the stoichiometric property of SnO_2. For the *SCF* cycles, *2.08* and *1.79* were used as muffin-tin radius values for *Sn* and *O*, respectively.

A *(1*1*3)* supercell was created to investigate the impact of oxygen vacancies, which resulted in a material containing a total of 18 atoms: 6 of tin and 12 of oxygen. Then, two different numbers of oxygen atoms were removed in order to study various reduced samples with varying concentrations of oxygen vacancies ($SnO_{1.83}$ and $SnO_{1.67}$). All structures employed in the calculations of this work were relaxed using the *GGA* parameterized *PBE* (*GGA_PBE*) [105] by minimizing the forces acting on each atom to achieve values below *1 mRy / a.u*.

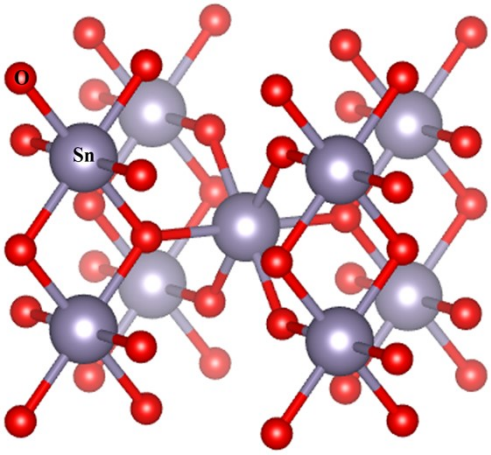

Figure III. 1: Rutile unit cell of SnO2 used in this work.

❖ Optimization of K-mesh and R*Kmax

It is necessary to optimize certain parameters that will be used for the main *SCF* cycles before the calculation of any type of properties. On the one hand, the sampling of the Brillouin zone was carried out according to the Monkhorst-Pack scheme [140] and the number of *K*-points was optimized to obtain a good convergence in the calculations. The optimization process was performed by varying the number of *K*-points and calculating the total energy of the system. Figure III. 2-a illustrates the variation of the total energy with respect to the number

of *K*-points in the first Brillouin zone. On the other hand, the *R*Kmax* is the number of plane waves in a Fourier expansion of the potential in the interstitial region (*RMT* × *Kmax*). It has also been optimized for a good convergence of the total energy using the same procedure used for *K*-points (Figure III. 2-b).

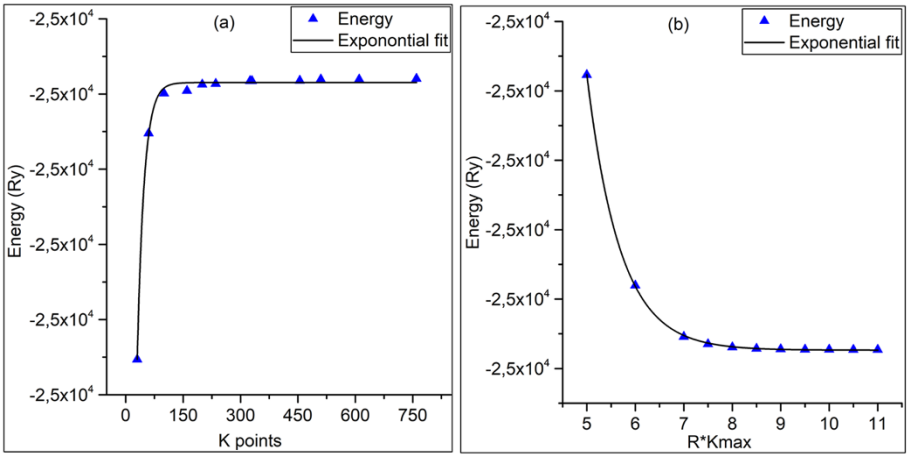

Figure III. 2: optimization of to the number of K-points in the first Brillouin zone and number of plane waves in a Fourier expansion of the potential in the interstitial region.

3.2. Results & discussion

3.2.1. Optimization of stoichiometric SnO_2

This work requires an optimization of the stoichiometric structure of SnO_2 which will be the starting point to investigate the impact of oxygen vacancies. To this end, the produced structure based on the literature was relaxed, and then the structural and electronic properties of SnO_2 were calculated.

The structural stability of SnO_2 was studied by the *FP-LAPW* method by computing the total energies as a function of the structural parameters, using the *GGA_PBEsol* exchange and correlation potential. This structure is characterized by various structural parameters: the cell parameters a and c, the ratio c/a, and the internal parameter u which is referred to the relative position of the anion O^- and the cation Sn^+ in the *c* axis. Table III. 1 presents the structural parameters calculated in this work and those identified in the literature. The volume and lattice parameters *a* and *c* are optimized by adjusting the total energy to the Murnaghan equation of state [141] (Figure III. 3-a, b). On the one hand, concerning the lattice parameters, the results obtained by *DFT* calculations applying the *GGA_PBEsol* approximation are in good agreement with those of SnO_2 synthesized by the sol-gel method (see part 3.1.) and also with those reported in the literature (experimental and simulated results) [139] [142] [143].

On the other hand, an underestimation of the bulk modulus *B* and the pressure derivative *B'* can be noticed, which can be justified taking into account that the *GGA-PPEsol* approximation does not give good results regarding this kind of properties [144]. However, comparing the value of the calculated compressibility modulus with the experimental one, the obtained value is close to the experimental one, even if it is quite underestimated: the

calculated value in our work is *197.5, 3.8%* less than the experimental one (*205 GPa)*. Slight difference was obtained between our results and those reported by Monica Calatayud et *al.* [145] (using PW method with GGA approximation) and E.L Peltzer y Blanca [146]. The difference may be due to the different codes used (i.e. the method and the exchange-correlation potentials) and the choice of the parameters used for the simulation such as the number of K-points in the first Brillouin zone, the radius muffin-tin (RMT) and the number of plane waves in a Fourier expansion of the potential in the interstitial region (R*Kmax).

Table III. 1: Structural parameters calculated in this work compared to those identified in the literature.

Parameters		*A (Å)*	*c (Å)*	*c/a*	*u*	*B (GPa)*	*B'*
Simulated	Present work (GGA-PBEsol)	4.7636	3.2126	0.674	0.3055	197.5	4.73
	Literature (LDA) [143]	4.699	3.165	0.674	0.340	244.7	4.44
Experimental	This work	*4.7380*	*3.1861*	0.672	N/A	N/A	N/A
	Literature [139]	4.7367	3.1855	0.672	0.3070	205	7.4

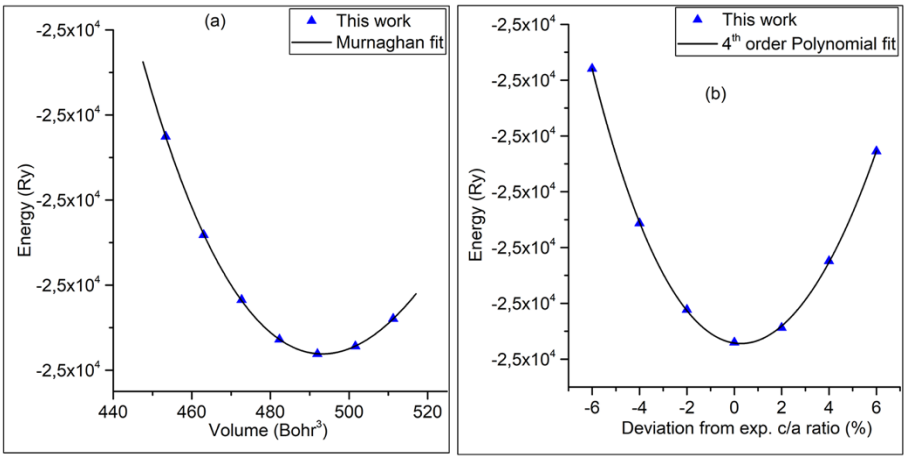

Figure III. 3: optimization of the volume and lattice parameters a and c by adjusting the total energy to the Murnaghan equation of state.

First, it is necessary to have a good understanding of the properties of bulk SnO_2 in order to study the impact of oxygen vacancy on the electronic properties of SnO_2-based materials. To this end, the total (*TDOS*) and partial (*PDOS*) densities of the electronic states of SnO_2 were calculated. The *GGA_PBE* approximation was used and, to improve the results, the *TB-mBJ* exchange-correlation potential was adapted.

The calculated *TDOS* and *PDOS* for stoichiometric SnO_2 are shown in Figure III. 4. It can be seen in Figure III. 4-a that stoichiometric SnO_2 is a semiconductor and that its electronic structure has a non-metallic character with a bandgap of about *3.558 eV* calculated by the approximation *GGA_PBE* combined with the potential *TB_mBJ*. Therefore, the value obtained

is in accordance with the experimental one (*3.6 eV)* [147] and also with other simulated results calculated based on *LDA+U* [148]. Looking at the *PDOS* graph (Figure III. 4), the VB of SnO_2 is mainly composed of *O-2p* states and some *5p* states of *Sn*, while the CB was mainly from *O-2p* to *Sn-5s* states.

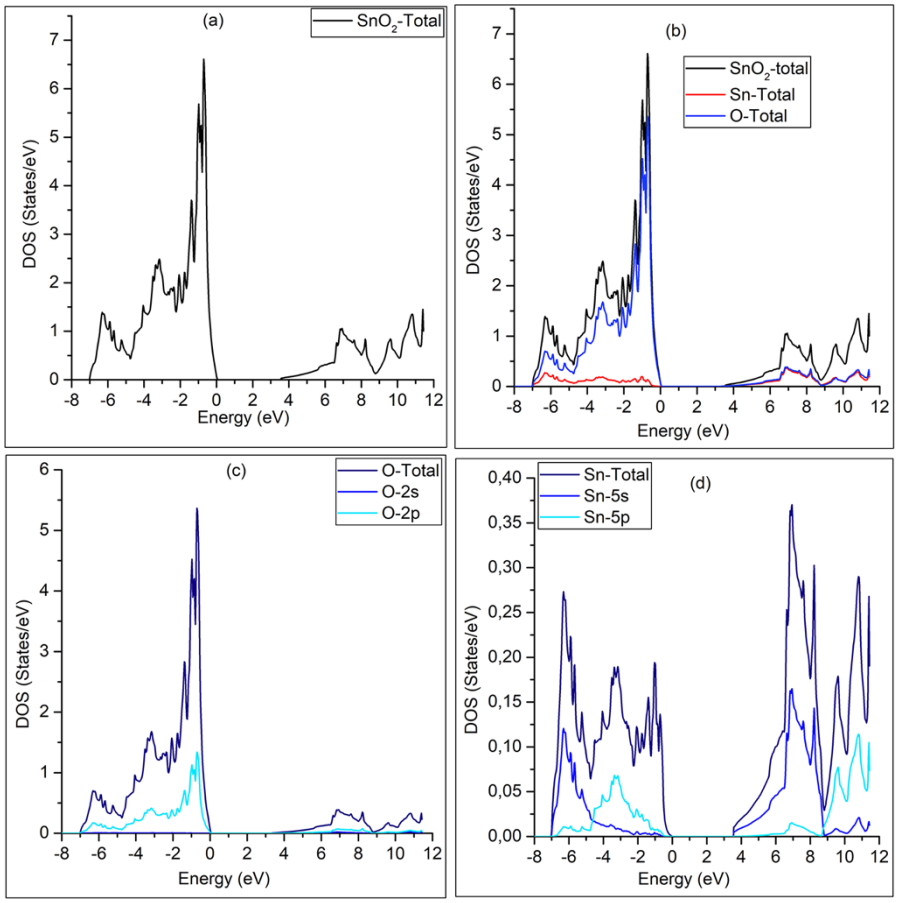

Figure III. 4: Calculated total and partial DOS for stoichiometric SnO2

3.2.2. Influence of oxygen vacancies

Notwithstanding the significant advantages demonstrated by *MOXS*-based gas sensors in general and SnO_2-based gas sensors in particular, these devices still show some shortcomings in terms of performance (e.g. selectivity, stability and high operating temperature). Researchers have attempted to solve these issues in several ways, including new methods for the synthesis of innovative materials, e.g. solid solutions composed of different metal oxides (WO_3-SnO_2, SnO_2-TiO_2...) [149] [150], and the production of metal oxides with controlled oxygen vacancies concentrations [151]. However, the literature presents a lack of studies on how the arrangement and number of oxygen vacancies affect the sensing performance, and only a few preliminary works have shown some valuable results [151] [152] [153] [154]. In fact, the main role of oxygen vacancies in modifying the sensing performance cited in the literature is based on a modification of the amount of oxygen species adsorbed on the surface or, alternatively, on the baseline resistance [151], i.e. oxygen vacancies act as donors that modify the conductivity of the sensing material [155] [156]. In fact, oxygen

vacancies are one of the most defects that can be formed in MOX. They can be created experimentally by specific treatments, for example heat treatment in a reducing environment, electron and high-energy ion bombardment, doping with metallic or non-metallic ions and heat treatment in an oxygen-depleted state [156].

In this part of the work, a first-principles study of electronic conductivity, structural and electronic properties of Oxygen-vacancy-defected SnO_2 have been done. Figure III. 5 illustrates the structures used in this investigation that are cleaved from the optimized rutile SnO_2 unit cell discussed in part 3.2.1.

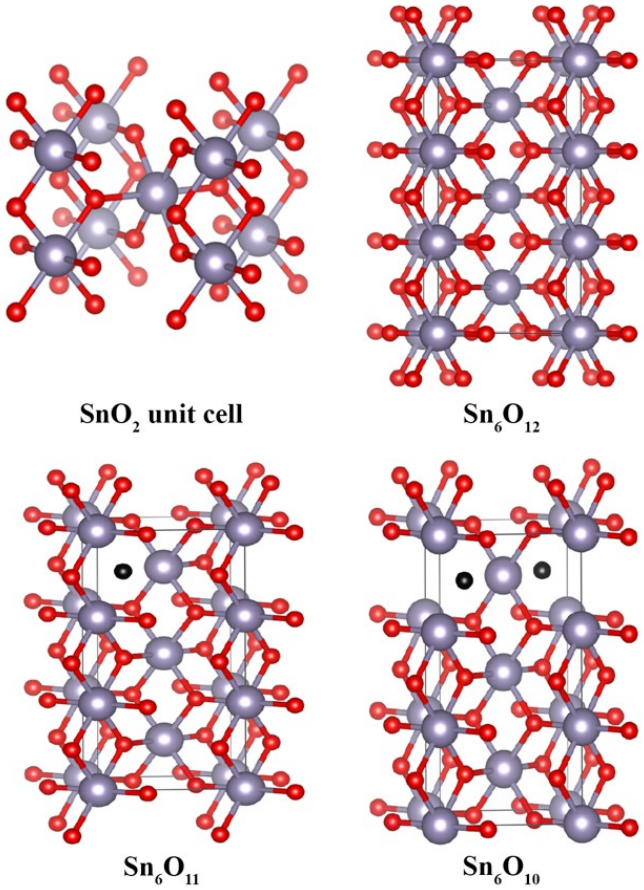

Figure III. 5: Models used to investigate the Oxygen-vacancy-defected bulk SnO2.

3.2.2.1. Structural properties

For the prediction of structural properties, the *GGA-PBEsol* approximation was used. The lattice parameters of Sn_6O_{12}, Sn_6O_{11} and Sn_6O_{10} computed in this work are listed in Table III. 2. The influence of oxygen vacancies on the SnO_2 structure can be seen clearly from this table: the higher their concentration, the longer the lattice parameter *a*, while shorter the *c* parameter. This behavior can be explained by taking into account the charge of the oxygen and tin atoms as well as the oxygen vacancies. Oxygen vacancies have a positive charge, which will attract oxygen atoms around the vacancy, causing a contraction of the lattice parameter c. In addition, oxygen deficiencies will exclude tin atoms around the oxygen vacancy, causing an expansion of the lattice parameter *a*. The modification of the structure of SnO_2 will lead to

a change in its physico-chemical properties which involves a modification of the sensing performance.

Table III. 2: Volume and lattice parameters of Sn_6O_{12}, Sn_6O_{11} and Sn_6O_{10} computed in this work.

	a (Å)	*c (Å)*	Volume *($Å^3$)*
Sn_6O_{12}	4.7621	9.6439	218.7011
Sn_6O_{11}	4.7805	9.5699	218.7011
Sn_6O_{10}	4.7780	9.5800	218.7011

3.2.2.2. Density of state

To calculate the electronic and electrical properties, which are very important for the gas sensing application, the *TB-mBJ* exchange correlation potential has been applied. Figure III. 4 (a, b, c and d) presents the total and partial densities of states of stoichiometric SnO_2.The valence band maximum (*VBM*) has been set to 0, the occupied states below the Fermi energy correspond to the VB, while the unoccupied states above the Fermi energy correspond to the CB. As shown in Figure III. 4-a and Figure III. 4-b, the VBs are mainly composed of *O*-type atoms and, from Figure III. 4-c, it can be seen that the *O-2p* character is the most dominant. Analyzing Figure III. 4-d, it can be concluded that the VBs are mainly of *O-2p* character with a slight hybridization with *Sn-5p* and *Sn-5s* states. The bandwidth of the VB is about *7.05 eV*. Above the Fermi level, the group of lowest CBs may be due to the hybridization of the *O-2p*, *Sn-5s* and *Sn-5p* states. The calculated bandgap of stoichiometric SnO_2 by application of *TB_mBJ* is *3.558 eV*, which is very close to the experimental value of *3.6 eV* and higher than other calculated values identified in the literature (*0.9 eV* using *PBE* [157], *0.832 eV* applying *GGA* and *2.76 eV* using *mBJ* [158]). The *DOS* calculated in this work is consistent with the literature [159] [160] [161].

To study the impact of oxygen vacancies concentration on the density of states of SnO_2, a supercell (1*1*3) was created, which gave us a material containing a total of 18 atoms: 6 of tin and 12 of oxygen, noted Sn_6O_{12}. The *TB_mBJ* was used as an exchange correlation potential for the calculation of all the supercells studied in this part of the work. Figure III. 6(a-f) represents the total and partial density of states for Sn_6O_{12}, Sn_6O_{11} and Sn_6O_{10}, I which the *VBM* was set to 0. For defective SnO_2 with one oxygen vacancy (Sn_6O_{11}), an additional impurity peak was clearly found near the VB, compared to the stoichiometric SnO_2 (Figure III. 6-a and IV-6b, peak 1). This peak can be linked to the appearance of a new energy level. The existence of tail states of the CB below the minimum of the CB can also be observed for Sn_6O_{11}, as shown in Figure III. 6-b and Figure III. 6-e. These states result in a broadening of the VB and a narrowing of the band gap in Sn_6O_{11}. An important point to be noted is that *DFT*

studies suggest that impurity level formation is responsible for the increase of the VBM and possibly narrowing of the band gap in oxygen-deficient MOXS [162] [163] [164]. Moreover, in the case of Sn_6O_{11} and Sn_6O_{10}, the VBs are mainly of *O-2p* character with a very small hybridization with the *Sn-5p* and *Sn-5s* states (Figure III. 6-e-f). It can be stated that oxygen vacancies do not influence the dominant states at the top of the VB (Figure III. 6-d, e and f) but it is also clear that the hybridization of *O-2p*, *Sn-5s* and *Sn-5p* states close to the minimum of the conduction band (CBM) becomes more important with the creation of oxygen vacancies, which can be explained by the exchange of electrons between the oxygen vacancy and the different host sites [165]. Consequently, under the effect of temperature, electrons will be excited by the vacancy, which will lead to a single or double ionization of the same vacancy [165]. These electrons can be captured by different host sites, and the most probable may be, in this case, the Sn^{4+}, which will be reduced to Sn^{2+}. Thus, there will be a level of electron donor in accordance with the representative energy diagram given by Christophe Pijolat [165].

Rising the number of oxygen vacancies from one to two atoms per supercell (Sn_6O_{10}), a second peak appeared (Figure III. 6-c, peak 2) near the minimum of the CB, furthermore the impurity states become more delocalized and overlap at the VBM (peak 1 of Figure III. 6-c).

The relocation of the donor level can promote the excitation of electrons from the dopant level to the CB of the semiconductor. Therefore, it can also improve the reactivity of the surface of the sensing material, by increasing the adsorption rate of oxygen molecules from the surrounding atmosphere onto the semiconductor surface, which is on the basis of the MOXS sensing mechanism [25] [166].

In addition, the density of the states in the impurity level, after the increase of the concentration of oxygen vacancies, is reduced (peak 2 Figure III. 6-c). This phenomenon has been demonstrated experimentally by Maffeïs et al [167], i.e. for small particles, there is a greater density of states and thin peaks in the region of the band gap. The sensing performance as a function of grain size is presented in [168]. The improvement of the detection response can be explained by a detinning of the Fermi level [169].

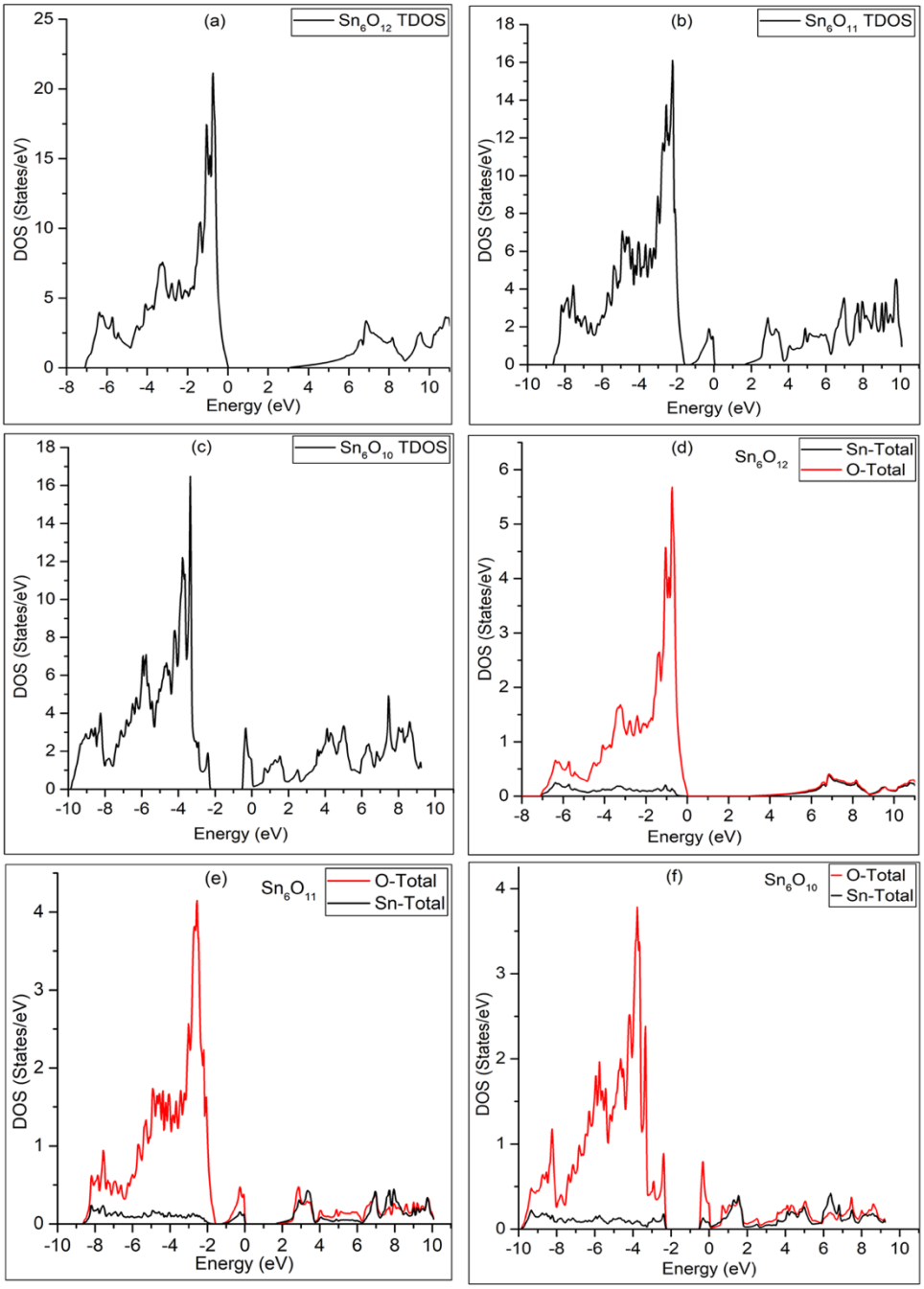

Figure III. 6: Total and partial density of the states calculated for Sn6O12, Sn6O11 and Sn6O10

3.2.2.3. Electrical conductivity

For the purposes of investigating the mechanisms of electrical conductivity, the logarithm of electrical conductivity (*log(σ)*) should be plotted as a function of *1000/T*. Figure III. 7-a represents the relationship between *log(σ/ τ)* and *1000/T* for SnO_2 with different oxygen vacancies concentrations in the range of temperature going from *280K to 510K* (τ is the relaxation time of SnO_2). In addition, the behavior of the electrical conductivity of different SnO_2 samples as a function of temperature in a range varying from *280K to 510K* is shown in Figure III. 7-b. From this Figure, it can be seen that the electrical conductivity increases with rising temperature, which is the common behavior of semiconductors. Indeed, the rise in

temperature results in an increase in the number of electron-hole pairs, which causes an increase of the electrical conductivity [170]. The same Figure also shows that the electrical conductivity demonstrates an increase with the rise of the oxygen defects concentration, which is also confirmed by other experimental works [171]. When oxygen defects are somehow created in the SnO_2 lattice, it is obvious that they play a role as impurity states that generate more electron-hole pairs, thus increasing the electrical conductivity. For gas sensing applications, increasing the concentration of the oxygen vacancies can improve the SnO_2 sensing performance, since their higher concentration results in a higher concentration of adsorption sites for O_2 molecules, thus ensuring a higher activity of the sensing material surface [172]. This increase in surface activity, as well as the increase in semiconductor conductivity, may allow a reduction of the operating temperature of the sensing material, and a lower power consumption of the gas sensor [151] can be achieved. In addition, an unpinning of the Fermi, due to the narrowing of the density of the states in the impurity level, can contribute to improve the sensitivity of the material [169].

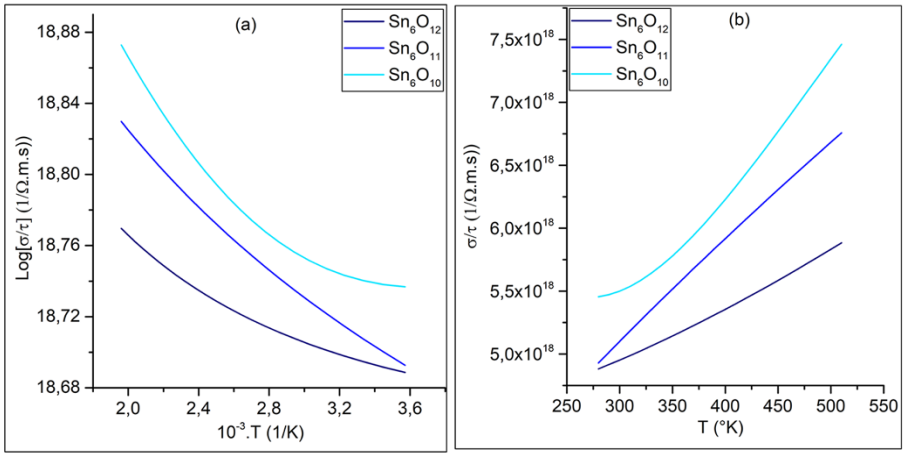

Figure III. 7: Variation of the electrical conductivity of the various samples.

3.3. Conclusions

In this section, the effect of oxygen vacancies on the structural, electronic and electrical properties of SnO_2 at two different concentrations ($SnO_{1.83}$, $SnO_{1.67}$) was investigated. Cell parameters, total and partial densities of states and electrical conductivity of these samples were computed theoretically using *DFT* simulations. The results indicated that by increasing the concentration of oxygen vacancies inside SnO_2, the impurity states approach the CB, thus increasing the probability that electrons promote the transition process from the donor level to the CB. This results in an increase of the electrical conductivity and, more importantly for sensing properties, greater availability of electrons to participate in reactions at the surface of the active material, with a beneficial impact also on the catalytic performance of SnO_2. The overall effect is a reduction in the temperature required for sensing material thermal activation, which means lower power consumption. In conclusion, by exploiting oxygen vacancies, it is

possible to mitigate one of the main limiting factors of the MOX gas sensor: the high working temperature and the resulting high energy consumption.

4. Synthesis, material and electrical characterization combined with DFT calculations of reduced SnO_{2-x}

In this part of the thesis, an experimental investigation was done in order to understand how oxygen vacancies influence the sensing performance of SnO_2 gas sensors. This study was compared and confirmed theoretically using Density Function Theory. For this purpose, a simple and low-cost sol-gel method to synthesize tin dioxide samples was used. To reduce the samples synthesized, the stoichiometric SnO_2 was reduced at different temperatures in a reducing atmosphere (3% of H_2). The experimental characterizations of the obtained samples were compared to the theoretical results obtained in section 3.

4.1. Synthesis

For gas sensors application and also for other applications such as solar cells [173] , several researches were conducted on tin dioxide synthesized by means of sol-gel method to obtain nanostructured SnO_2. Sol-gel techniques are used for two main purposes:

- producing powders for thick film deposition by means of screen printing.
- producing gels for thin films deposition by mean of "Dip-Coating" or "Spin-Coating".

The range of initial precursors that can be used is relatively wide: tin-based metal salts, usually $SnCl_2$ or $SnCl_4$ [174] [175] [176] [177] [178] [179] [180] and tin alkoxides such as tin (IV) ethoxide $Sn(OC_2H_5)_4$, tin (IV) propoxide $Sn(OC_3H_7)_4$ [181], tin (IV) butoxide $Sn(OC_4H_9)_2$ [182] or tin (II) ethyl-2-hexanoate: $Sn(OOCCH(C_2H_5)\ C_4H_9)_2$ were used so far.

In this work, Tin (II) 2-ethylhexanoate was used for which numerous syntheses are proposed in the literature [183] [184]. 1g of Tin (II) 2-ethylhexanoate was added to a hydroalcoholic solution composed of 2-propanol and deionized water (ratio used = 30/70) The mixture was placed in an ice bath and stirred magnetically at room temperature for about 3 hours. The reaction product was left to settle for one night and then filtered and dried. The resulting powder was calcined at 400°C in air for 2 hours (sample P1), to produce the stoichiometric SnO_2. Finally, several reducing treatments at different temperatures were carried out to create oxygen vacancies on sample P1. The resulting samples were noted SnO_2-P2, P3 and P4 and the description of each individual thermal treatment is shown in Table IV. 1.

Table IV. 1: Description of individual thermal treatment for synthesized samples.

Sample	Atmosphere	Temperature (°C)
SnO_2-P1	Treatment in air	400

SnO_2-P2	SnO_2-P1 + Reducing treatment in H_2	300
SnO_2-P3		400
SnO_2-P4		600

The reducing treatments were carried out under a constant flux of H_2/N_2 (3%/97%) for 15 minutes, followed by a vacuum treatment at the same temperature useful to stabilize the oxygen vacancies created [185]. In the following table is reported a summary of the process steps applied to the powders P2-P4.

Sample	Step	Time (minutes)	Temperature (°C)	Atmosphere
SnO_2-P2	1	15	300	H_2 (3%)
	2	30		Vacuum
SnO_2-P3	1	15	400	H_2 (3%)
	2	30		Vacuum
SnO_2-P4	1	15	600	H_2 (3%)
	2	30		Vacuum

4.2. Results & discussion

4.2.1. Material characterizations

The morphology of the powder is an important factor in the chemeresistive gas sensing field. Indeed, it is shown in literature that different morphologies of the same semiconductor, e.g. nanoparticles, nanorods, or nanowires…, show great differences in sensing properties. These variations are mainly due to two causes, i.e. different grain size that results in a variation of the semiconductor surface available for interaction with the gaseous molecules, and a percentage change of the depletion layer in the presence of the same gas concentration between two different morphologies. [83]. The morphology of the samples was analyzed by scanning electron microscopy (SEM), and the images collected are reported in Figure IV. 1. All the samples showed spherical particles. The calculated grains sizes were 29.43, 11.36, 16.88 and 14.53 nm for the SnO_2-P1, SnO_2-P2, SnO_2-P3 and SnO_2-P4 samples, respectively.

Going from the air to H_2 atmosphere and increasing the temperature a strong decrease in the grain size was recorded. Moreover, the grain size decreased more when the temperature increased, this may be due to the increase of the concentration of oxygen vacancies in the

sample with the increase of the temperature. Our findings are in agreement with reported results for SnO_{2-x} and WO_{3-x}, i.e. the creation of oxygen vacancies results in a decrease of the gain size of the samples [186, 187].

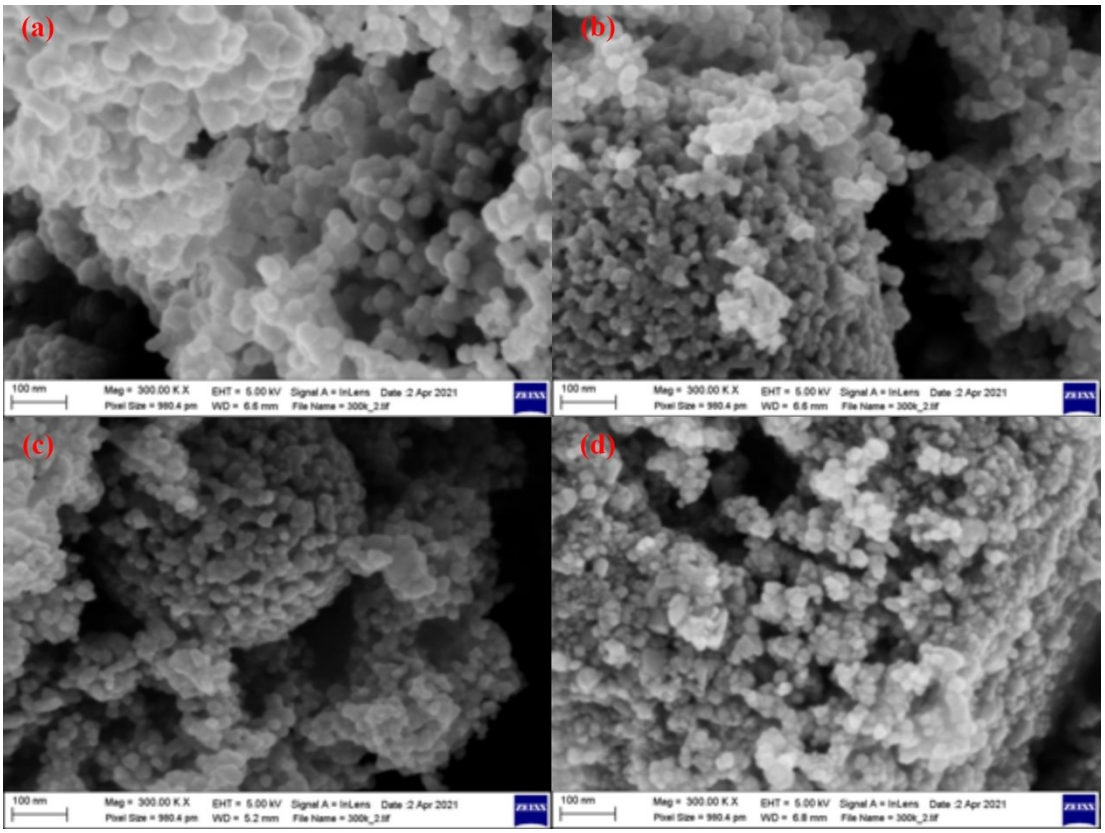

Figure IV. 1: SEM images of (a) SnO_2-P1, (b) SnO_2-P2, (c) SnO_2-P3 and (d) SnO_2-P4.

XPS analyses were performed on the samples to investigate the elemental composition of nanoparticle surface and to identify the oxygen vacancies created by the heat treatments. The spectra collected also highlighted the presence of C in all the samples analyzed, probably from the carbon tape used as powder support in the XPS characterizations. Considering the oxidized sample (SnO_2-P1) and the reduced one at 600 °C (SnO_2-P4), an increase in the Sn/O ratio can be seen, that is to say the concentration of oxygen vacancies is increased with the increase of the heating temperature.

Table IV. 2: Elemental composition in the obtained samples.

Sample	O (%)	Sn (%)	C (%)	Sn/O
SnO_2-P1	56.6	29.9	13.5	0.53
SnO_2-P2	46.1	22.4	31.6	0.48
SnO_2-P3	55.7	30.4	13.9	0.54
SnO_2-P4	48.8	26.7	24.6	0.55

Figure IV. 2 shows the Sn-3$d_{3/2}$ and Sn-3$d_{5/2}$ components. On the one hand, different intensities were recorded for all the data which may be attributed to the different roughness and surface contamination of the samples. The observed core level binding energies agree well with previous measurements. [34] The spin-orbit separation of 3d5/2 and 3d3/2 is 8.37, 8.40, 8.49 and 8.38 eV for the SnO_2-P1, SnO_2-P2, SnO_2-P3 and SnO_2-P4 samples, respectively. A small shift of both components was recorded for all samples, even for SnO_2-P2 was too small, but for the reduced samples was quite important. By considering the oxidized sample (SnO_2-P1) and the most reduced one (SnO_2-P4), the shift was about 0.31 and 0.32 eV for Sn-d3/2 and Sn-d5/2 respectively, which is in good agreement with recently reported values [187]. The trend obtained in the peak shifts describes the trend of the concentration of surface oxygen vacancies in the samples, i.e. the sample SnO_2-P4 contains the higher concentration (Table IV. 2:) and the peaks attributed to this sample were moved more than the others also the grains size in this case was lower (16 nm). Indeed, by comparing the sample treated in hydrogen at the higher temperature with the oxidized one in air, a significant shift of the peaks was obtained. Furthermore, a small additional component (see Figure IV. 2) appearing at a binding energy of about 484 eV can be observed, which could be attributed to the elemental tin Sn^0 [188].

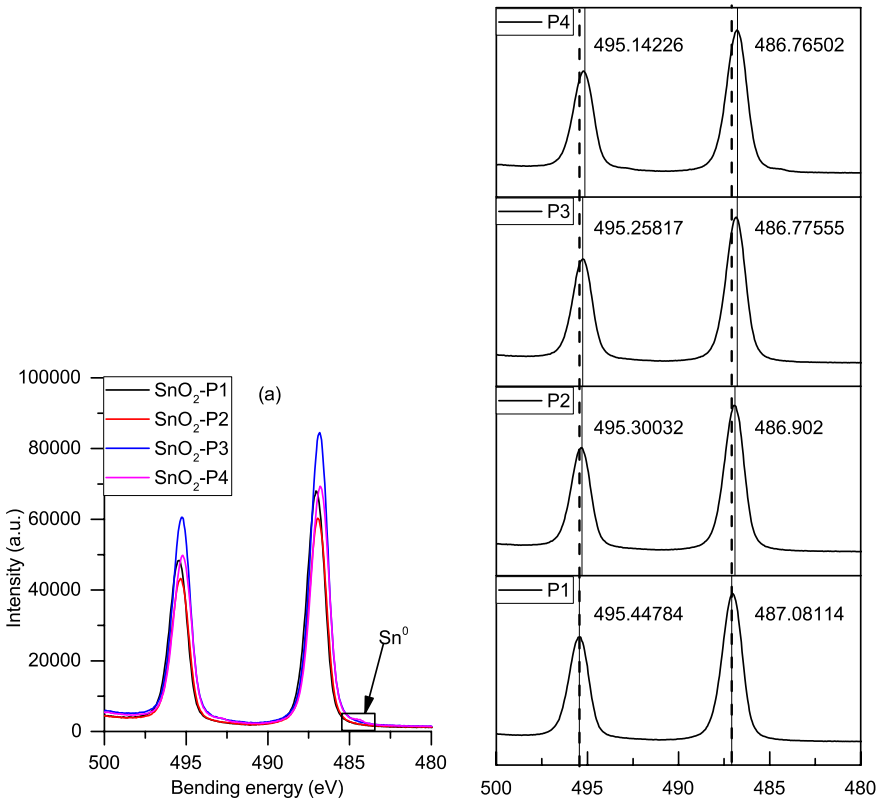

Figure IV. 2: XPS spectrum of the Sn-3$d_{3/2}$ and Sn-3$d_{5/2}$ components for all samples.

Sn valence band appears at lower energy than the Sn4d peaks (Figure IV. 3), the VB appears at low energies, since electrons in this band are the first to be ejected. It is possible to determine the position of the Fermi level with respect to the VBM of SnO_2: the energy

separating the Fermi level and the top of the VB is obtained by extrapolating the slope of the highest intensity peak of the VB [189]. By knowing the width of the band gap, it is possible to have an estimation of the position of the Fermi level in the band gap. In tin dioxide, the O-2p states are the dominant states in the VB, while the CB is composed of hybridizations of O-2p and Sn-5p states [124]. The shallow core level Sn-4d was found to be approximately at the bending energy of -22.3 eV for all samples. The contributions of the O-2s appear quite wide, and these emissions are considered a second region of the VB because they are based on the hybridization between states coming from O-2s and Sn-4d. This is concluded by projecting the density of states on the atomic orbitals, as reported in Figure IV. 3. The characteristic three-peak structure was shown in the VB spectra of the samples, as illustrated in the inset of Figure. The increase of the intensity of the bands can be seen by zooming in on band gap region (inset in Figure IV. 3). This increase can be related to the impurity states coming from oxygen vacancies at the surface of the material.

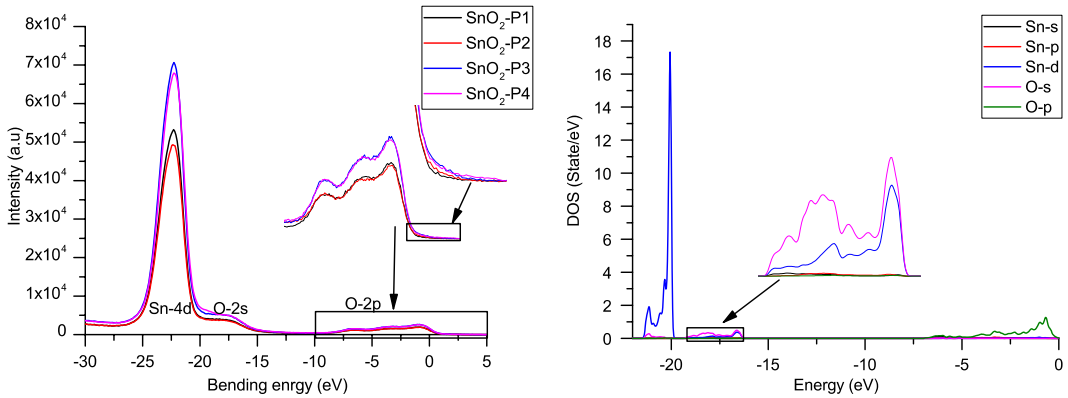

Figure IV. 3: Global valence band XPs spectrum of the obtained samples (left) and DOS graph including Sn-4d states (right).

To confirm the above discussed results, a series of first-principles calculations were done. In Figure IV. 4, the XPS data and the density of states obtained theoretically by means of DFT calculations is illustrated. The appearance of the new states in the forbidden band gap region can be seen clearly from the DOS graph and it corresponds to the creation of oxygen vacancies [124]. In addition, the increased intensity of the bands in the band gap region observed in the XPS analysis (inset in Figure IV. 4) can be attributed to the increase in the concentration of oxygen vacancies. From DFT calculations of reduced SnO_2, a broadening of the VB and a shift of its top (insets of Figure IV. 4) were obtained, which can be observed also in our XPS spectra where the calculated width of the VBs for the samples SnO_2-P1 and SnO_2-P4 were about 10.17 and 10.57 eV, respectively. Another observation from the theoretical point of view is the narrowing of the band gap due to impurity states created by oxygen vacancies.

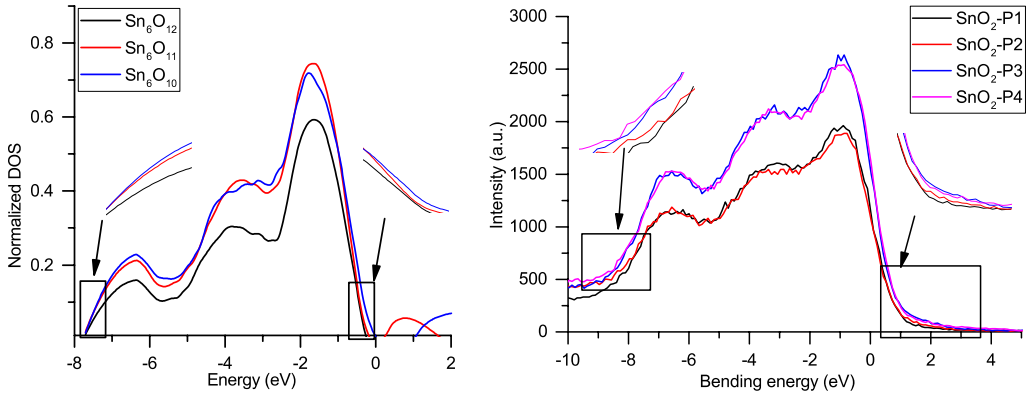

Figure IV. 4: XPS valence band (right) compared to theoretical DOS valence band (left).

The UV-visible analysis was carried out to experimentally evaluate the band gap of the P1-P4 samples. The absorption spectra of the three samples are shown in Figure IV. 5. It can be seen from Figure IV. 5 that going from a heat treatment in air to a reducing atmosphere and by increasing the temperature of the reducing treatment, the absorption edges of SnO_2 are redshifted from the oxidized SnO_2, which is attributed to the replacement of Sn^{4+} by Sn^{2+} in the lattice of the reduced material [190]. The formation of oxygen vacancies involved an excitation of electrons, which led to a single or double ionization of the same oxygen vacancies [165]. These electrons can be captured by different host sites and the most probable sites, in this case, may be the Sn^{4+} that will be reduced to Sn^{2+} [124]. Tauc plots were used for the determination of the band gap energies. The values of the bandgaps of SnO_2-P1, SnO_2-P3, and SnO_2-P4 were about 3.22, 3.04, 2.86 and 2.74 eV, respectively. This decrease in the band gap values can be expected and explained: the new states created by the formation of oxygen vacancies result in a broadening of the VB and a narrowing of the band gap in reduced samples [124]. An important point to be noted is that DFT studies suggest that impurity level formation is responsible for the increase of the VBM and possibly narrowing of the band gap in oxygen-deficient metal oxide semiconductors [164] [163]. This makes the results obtained by UV visible analysis in accordance with the XPS and DFT calculations.

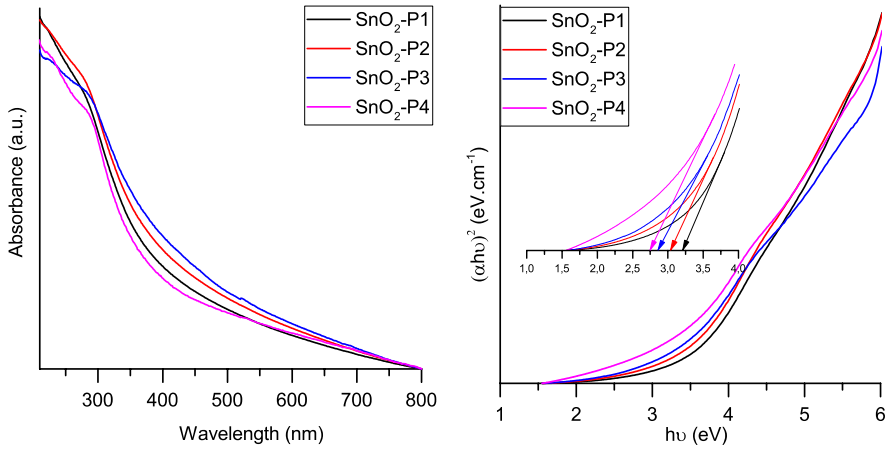

Figure IV. 5: UV–Vis spectra of the obtained samples: (left) absorbance spectra and (right) Tauc plots for band-gap energy calculations.

Figure IV. 6 shows the typical XRD pattern of the prepared SnO_2 samples. The oxidized sample (SnO_2-P1) exhibited a tetragonal crystal structure of cassiterite SnO_2 (s.g. P42/mnm PDF: 01-071-0652). The cassiterite crystal phase of SnO_2 remained unchanged for samples SnO_2-P1-P2 and P3, as shown in Figure IV. 6. However, new peaks appear at about 30.5, 32.0, 44.0 and 45.0 °2θ upon heat treatment in the H_2 atmosphere at 600°C (Figure IV. 6, fuchsia graph). These peaks are attributed to Sn (s.g. I41/amd PDF: 03-065-0296) [191]. This can confirm the observed presence of metallic tin using the XPS analysis (see Figure IV. 2-a). We were unable to find any significant differences between the lattice parameters and particle sizes for the different samples with our XRD measurements. Basically, the same intensities and theta values were recorded, indicating the structural equivalence of the samples with the exception of SnO_2-P4. The obtained lattice constants for the oxidized sample were $a=b=0.473804\pm 0.000019$ *nm* and $c=0.318606\pm0.000016$ *nm*. Each Sn is sixfold coordinated with O while each O atom is threefold coordinated with Sn.

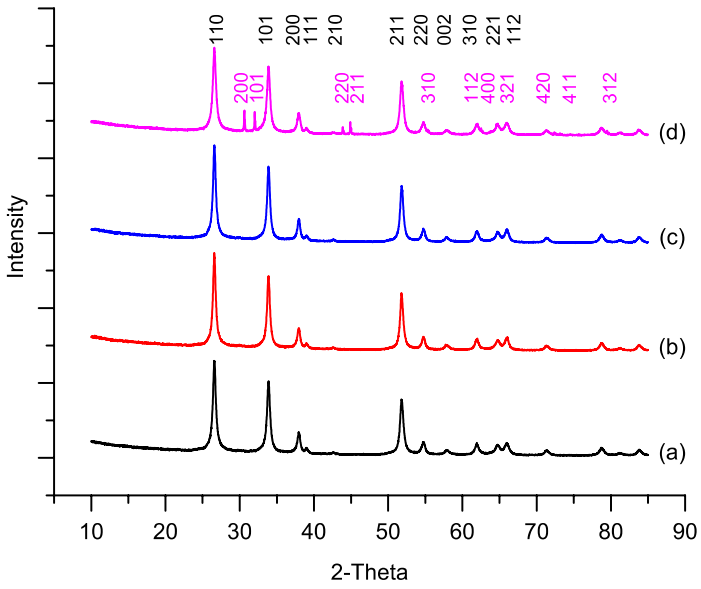

Figure IV. 6: XRD patterns of the SnO_2 samples: (a) SnO_2-P1, (b) SnO_2-P2, (c) SnO_2-P3 and (d) SnO_2-P4.

4.2.2. Sensing performance

The electrical characterization of the sensors produced based on the synthesized materials were carried out to study the sensing performance of the devices. The survey was done in 40 % of relative humidity. The results obtained are shown in Figure IV. 7. First the optimization of the operating temperature was carried out by exposing the sensors to 0.5 ppm of NO_2 at three different working temperatures (70, 130 and 180 °C). Indeed, the working temperature is one of the main characteristics of a gas sensor, since it has an important impact on the gas sensing properties, due to its great impact on the adsorption-desorption process. As it can be seen from Figure IV. 7, all the samples showed the highest sensitivity at 130 °C apart from the oxidized sample (SnO_2-P1), which showed an increase of the sensing response by

increasing the working temperature. This behavior can be expected since the stoichiometric SnO_2 sensor works usually at high temperatures (about 300-400°C °C). As a result, 130 °C was set to be the optimum temperature for NO_2 detection by using the reduced SnO_2 samples. It is well known that MOXS-based gas sensors are the most used and studied material for this application since they present important advantages meanwhile one of the most important disadvantages is the high working temperature. From the previous analyses, the reduction of the samples (the creation of oxygen vacancies) may mitigate one of the most disadvantages of MOXS gas sensors can be concluded, which is the high working temperature. In Figure IV. 7 the dynamical response of the devices towards different concentrations of NO_2 (0.1, 0.2, 0.5 and 1 ppm) at the optimized operating temperature (130 °C) is reported. It is clear that the sensors show an increase in the sensor response with the increase in the gas concentration (Figure IV. 7). The change in the gas sensor response with respect to the gas concentration is reported in Figure IV. 7, from where it can be seen that the behavior of the response versus the gas concentration is almost linear. The response to 0.5 ppm of NO_2 of the device based on the most reduced sample was about 31 which is 10 times the response recorded for the device produced based on the oxidized sample (about 3). In addition, it can be seen from that Figure that as much as the concentration of oxygen vacancies increases as much as the sensing response of the sensor increases. To conclude, the oxygen vacancies enhanced the sensitivity of SnO_2 based gas sensors toward low concentration of NO_2 (0.5 ppm) and overcame the most drawback presented by MOXS-based gas sensors, i.e. the high working temperature. However, it worth mentioning that the sensing response does not reach a steady state (see figure) which means that the sensor response/recovery time are quite high in this case.

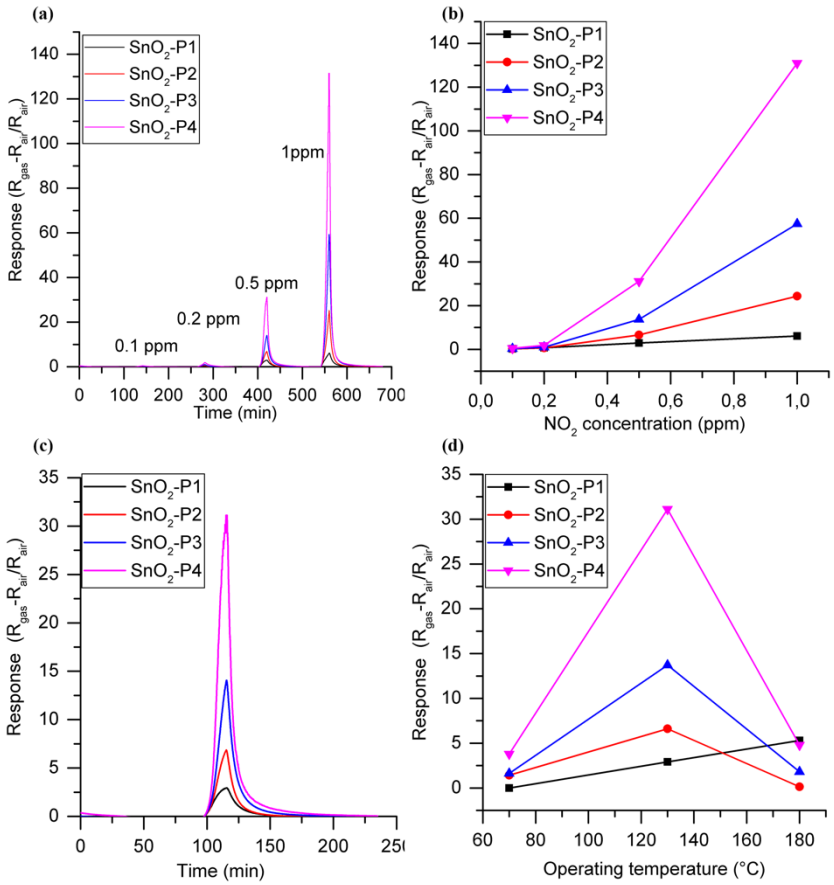

Figure IV. 7: (a) Dynamic response curves of different concentrations of NO_2 (0.1-1 ppm) at 130 °C of the sensors based on oxidized SnO_2 (SnO_2-P1) and reduced samples (SnO_2-P2-P4). (b) Calibration curves of all sensors. (c) Response behaviors towards 0.5 ppm NO_2 at 130 °C. (d) Gas response of all sensors at different operating temperatures to 0.5 ppm NO_2. All measurement were carried out in 40 % of relative humidity.

4.3. Conclusions

In this part of the work, reduced samples of SnO_2 were synthesized using an easy and low-cost method, i.e., sol-gel method combined with thermal treatments in reducing atmosphere. The resulting samples were characterized using SEM, XPS, XRD, and UV-visible techniques. The experimental results were compared and confirmed using first-principles study, i.e., DFT calculations. The results showed a broadening of the VB and a narrowing of the band gap region, this may conduct to an enhancement surface reactivity of the sensing material, i.e., the narrowing of the band gap make it easy for electrons to jump from the donor level to the CB and then participate in the reactions at the surface of the sensing layer. Indeed, the sensing performance of the devices produced showed an enhancement of the sensitivity and decrease of the working temperature to detect low concentration of NO_2. To summarize, the oxygen vacancies enhanced of the reactions at the surface of the active element, and this resulted in an improvement of the sensitivity of the gas sensor and also it reduced the temperature that the sensor needs to be thermoactivated, which is a reduction of the sensor working temperature involving a decrease of the device power consumption.

5. Study of the SnO_2 surface

To understand the mechanism of chemical sensors, a wide range of research has been conducted on the physico-chemical interactions between the surfaces of MOX used as a sensing layer and gas molecules. The operating principle of gas sensors is based on the change in the oxidation/reduction of the surface due to chemisorption. This change, which depends strongly on the oxidizing or reducing nature of the gas as well as on the composition of the MOX (stoichiometric or deficient), leads to a variation in the doping of the semiconductors and thus to the modification of the electrical conductivity. During this process, a charge transfer can be established between the adsorbate (the gas) and the adsorbent (the surface) due to the chemical reaction at the surface.

In general, SnO_2 gas sensors are exposed to the atmosphere before the target gas is introduced (Figure V. 1). When the sensor is exposed to a reducing (oxidizing) gas, the gas molecules interact with chemisorbed oxygen species from the surrounding atmosphere and decrease (increase) the resistance of an n-type gas sensor (e.g. SnO_2), and vice versa for a p-type semiconductor. This change in resistance is due to the exchange of electrons between the material surface and the gas molecules.

Our DFT calculations, at this stage, concerns the study of the first part of this mechanism going from the possibility of the interaction between stoichiometric SnO_2 surface and oxygen molecules from the surrounding atmosphere. Thus, an investigation on the formation of surface oxygen vacancies and then a study of the interaction between the reduced surface and oxygen molecules has been done.

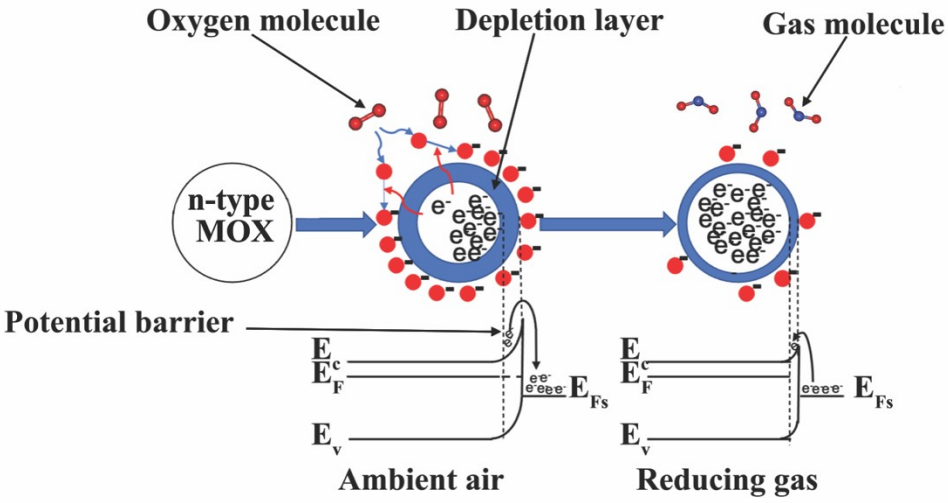

Figure V. 1: representation of the two main steps for gas detection.

5.1. Computational details

In this section, the structural and electronic properties of SnO_2 crystals and surfaces have been studied using DFT calculations. The pseudopotential plane waves approach was used, which is based on atomic pseudopotentials and a basis set of plane waves as implemented in the quantum espresso package [192]. This approach has been used because it is very efficient for dealing with extended periodic systems. In this case, calculations were performed using the generalized gradient approximation with two different settings for the exchange and correlation function: the Perdew Burkc- Ernzerhof for solids (GGA-PBEsol) for structural properties calculations and the Perdew Burkc- Ernzerhof (GGA-PBE) for relaxation and electronic properties calculations. Ultrasoft pseudopotentials were used to represent the ionic cores of tin and oxygen atoms. Different calculation schemes converge and give comparable results when all the main parameters are carefully defined. In the present case, by considering the value for which the total energy converges, the sampling of the first Brillouin zone and the energy cut-off for the wave functions (Figure V. 2) were verified. A cut-off threshold of 48 Ry for the wave functions and 432 Ry for the charge density were used, respectively. The need to use a higher value of the charge density cutoff is due to the fact that an accurate estimation of the electrostatic potentials is needed.

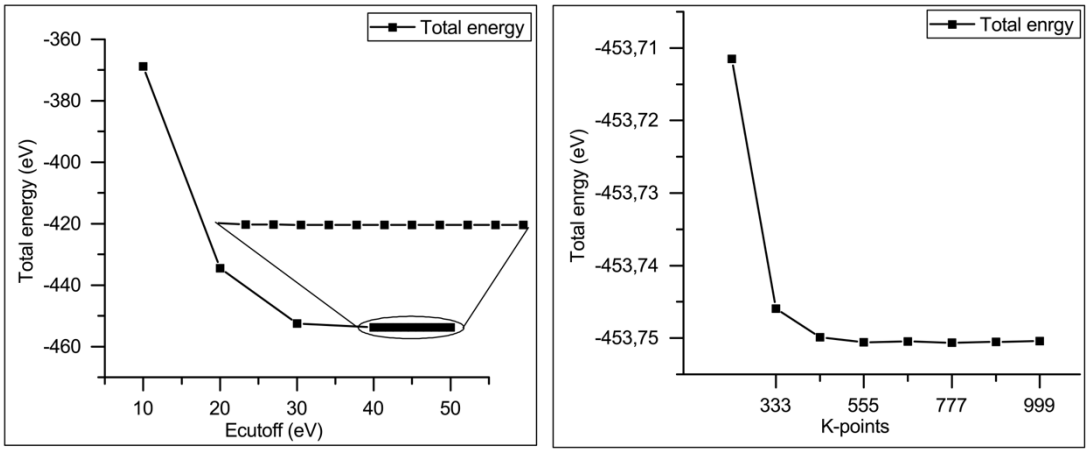

Figure V. 2: optimization of the number of K-points and the Energy cut-off.

The rutile unit cell of *SnO_2* (Figure V. 3-a) optimized in section 3 has been used for calculations in this section. In the first step, the bulk unit cell was optimized using PWPP method, in order to compare both full and pseudo potentials methods. The optimized unit cell has been used to create a 3 layers slab model for SnO_2 (110) surface (Figure V. 3-b). The slab has been studied as a three-dimensional supercell in this part of the work. A vacuum width of 10 A has been used to avoid interaction between periodic images, value that is large enough for this purpose.

For the sampling of the Brillouin zone, a 5*5*5 Monkhorst mesh was used for geometrical optimization of the bulk unit cell and 15*15*15 for the band structure and density of states calculations. Instead, a 2*2*1 Monkhorst mesh was used for geometrical optimization

of the surface models (6*6*3 for the band structure and density of states calculations). It was checked that finer meshes do not change the results.

The defective surfaces were obtained by removing the oxygen atoms at different locations. The furthest atomic plane of the stoichiometric SnO_2 (110) surface in Figure V. 3-b is described by rows of oxygen in bridging sites between paired tin atoms. Immediately beneath it, the atomic plane consists of alternating rows of oxygen and tin atoms. The subsequent plane consists only of oxygen, which is arranged in rows as well. The oxygen atoms in the three atomic planes mentioned above will be respectively called "bridging", "in-plane" and " subsurface" oxygens. The bridging oxygen atoms, in the plane and subsurface together constitute a primitive structural unit along the direction perpendicular to the surface, which will be called in the following a surface layer. Stoichiometric SnO_2 (110) surfaces are always preferred to other types of reconstructions when samples are prepared in an oxygen-rich atmosphere. In the present work, the scope is the analysis of how oxygen vacancies modify the properties of a stoichiometric surface and how they can influence the adsorption phenomena of oxygen species on the surface of SnO_2. The equation (Eq. V. 1) was used to calculate the formation energy of an oxygen vacancy.

$$E_{form}^{vac} = E_{slab+vac} + \frac{1}{2} E_{O_2} - E_{slab} \quad Eq.\ V.\ 1$$

where

$E_{slab+vac}$: Total energy of defective surface

E_{slab}: Total energy of stoichiometric surface

E_{O_2}: Total energy of spin polarized O_2.

The geometries of all the systems considered in this work were optimized by fully relaxing the atomic positions until the residual forces were less than 10^{-3} Ry / Bohr. And the convergence criteria for the total energy was set to 10^{-4} Ry.

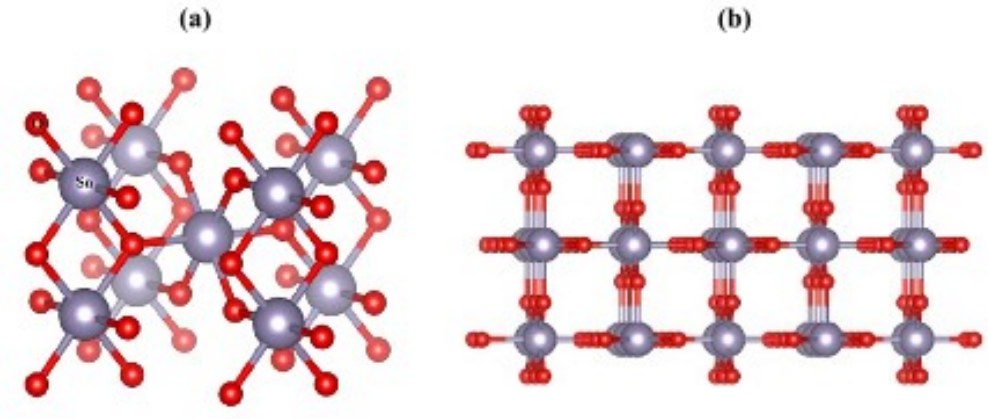

Figure V. 3: (a) Rutile unit cell of SnO2 and (b) 3 layers slab model for SnO2 (110) surface.

5.2. Results & discussion

5.2.1. Bulk SnO_2

- **Structural properties**

After the optimization of the parameters necessary for the calculations, the structure was relaxed and the cell parameters were further optimized using the plane wave method with pseudo-potentials. The relaxation method used in this case was the Broyden Fletcher Goldfarb Shanno (BFGS) algorithm. Table V. 1 presents the results obtained in this section compared to those calculated using the FP-LAPW method implemented in the Wien2k code. The same approximation for the exchange and correlation potential was used, which is the GGA-PBEsol, as this approximation gave good results for the calculation of the lattice parameters. In addition, the GGA-PBE was used to compare the two methods as well as two different approximations.

As it can be seen from Table V. 1, in general and applying the FP-LAPW method using the GGA approximation with PBEsol for the exchange and correlation potential, the calculated structural properties are in good agreement with the literature and close to the experimental observed results. Discussing the details of the obtained results reported in this table, it is possible to claim that FP-LAPW method gave more accurate results for the lattice parameters *a* and *c* (deviations from the experimental values were about 0.56 and 0.84 % for *a* and *c* respectively). The following more closed values to the experimental ones for the lattice parameters were obtained using PWPP approach by applying the GGA_PBEsol approximation (deviations from the experimental values in this case were 0.9 and 1.23 % for *a* and *c* respectively) while using PWPP method and applying the GGA_PBE approximation we obtained a deviation of 1.9 and 1.94 % for *a* and *c* respectively were obtained. Whereas, for the internal parameter *u* the most accurate value using the PWPP approach with GGA_PBE approximation (a deviation from the experimental value of about 0.1 % was obtained), while using FP-LAPW and PWPP methods and applying the GGA_PBEsol approximation the deviation from the experimental value was about 0.49 and 0.19 % respectively.

Table V. 1: Calculated structural properties obtained in this section compared to those calculated using the FP-LAPW method and to those identified in literature.

		a (Å)	*c (Å)*	*c/a*	*u*
Present work	FP-LAPW (GGA-PBEsol)	4.7636	3.2126	0.674	0.3055
	PWPP (GGA-PBEsol)	4.7797	3.2253	0.675	0.3064
	PWPP (GGA-PBE)	4.8284	3.2473	0.672	0.3067

Literature	Literature (LDA) [143]	4.699	3.165	0.674	0.340
	Exp. [139]	4.7367	3.1855	0.672	0.3070

- **Electronic band structure & DOS**

In Figure V. 4-a, the band structure of the bulk SnO_2 unit cell is illustrated. As it is known, SnO_2 is a direct band gap semiconductor, with the lowest electron-hole transition taking place at the Gamma point. It is worth reviewing the current results and comparing them with previous calculations of the band structure.

A comparison with the calculations performed in the reference [193] using the density functional theory with the GGA approximation yielded valuable results. Maki-Jaskari and Rantala [193] reported in their paper that ultra-soft pseudopotentials (USP) give more accurate results than norm-conserving pseudopotentials in the energy range near the top of the VB. Our results support their conclusion because the current band structure shape (see Figure V. 4-a) is in good agreement with the USP calculation across the entire VB spectrum. Besides, the PWPP method yields a VB width of 8.14 eV, which is consistent with the experimental and data previous first principles calculations reported in [194] and [193] using the norm-conserving and ultra-soft pseudopotential, respectively. From the graph of the band structure, a clear underestimation of the value of the band gap is evident (about 1 eV), due to the use of GGA_PBE. The DOS graph (Figure V. 4-b) obtained by the PWPP method is in good agreement with our previous calculations performed with the FP-LAPW method and with the XPS experimental analysis presented in section 4.

To conclude this part, we can consider that the FP-LAPW method using GGA_PBE combined with TB_mBJ approximations gave accurate results concerning the electronic properties of bulk SnO_2 in general, and in particular for the band gap value.

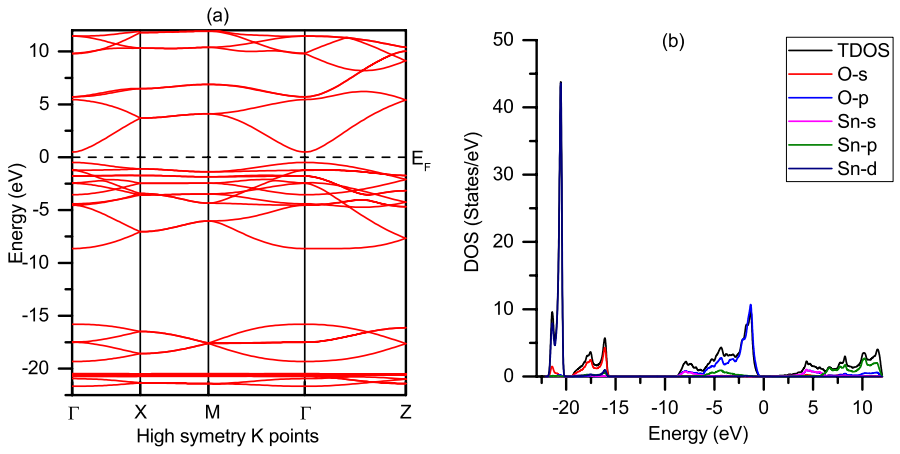

Figure V. 4: (a) band structure and (b) DOS graph of bulk SnO2 unit cell.

5.2.2. SnO_2 (110) surface

5.2.2.1. Stochiometric SnO_2 (110) surface

Among the crystalline faces of SnO_2, the stoichiometric surface (110) is the most thermodynamically stable. It is made up of layers of O-(Sn2O2)-O. Bridging, in-plane, and subsurface oxygens are the three types of oxygen on this surface. The removal of the bridging oxygen atom, the oxygen atom in the Sn2O2 last plane, or the oxygen atom in the subsurface results in the formation of a bridging, in-plane, or subsurface oxygen vacancy, respectively. When one oxygen atom is removed to create an oxygen vacancy, two electrons remain. As a result, tin is reduced from the six-coordinate Sn^{4+} to the four-coordinate Sn^{2+} ion.

Figure V. 5 shows the unrelaxed (a) and the relaxed (b) SnO_2 (110) surface. During the relaxation process, for the surface model, only atoms in the top layer were allowed to be relaxed, meanwhile the shaded layers in Figure V. 5 were kept fixed.

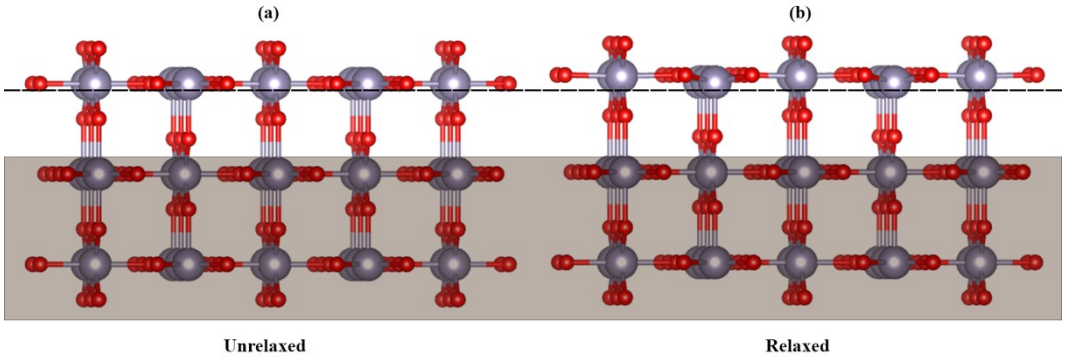

Figure V. 5: Slab model of the 3 layers SnO2 (110) surface using during this investigation.

- **Electronic band structure & DOS**

Figure V. 6-a depicts the band structure of a stoichiometric (undetected) SnO_2 surface. Surface bands appear inside the forbidden band gap, as evidenced by the comparison with the bulk SnO_2 band structure (see Figure V. 6-b). The projection of DOS (PDOS) onto atomic orbitals (Figure V. 6-c) reveals that the top VB is dominated by p states localized on the outer bridging oxygen atoms. The lower part of the CB is dominated by 5s orbitals on in-plane tin atoms, with a delicate hybridization with O-2p states on in-plane oxygen atoms. A surface band gap much smaller than the bulk one has been found due to the creation of the intragap surface states. According to our calculations, the stoichiometric surface has approximately 0.41 eV as a band gap located at the Gamma point. Figure V. 6 is qualitatively consistent with previous theoretical calculations, with the exception that the current method underestimates the band gap value. According to the literature, the Fermi level is just under the bottom of the CB (SnO_2 acts as an n-type semiconductor), and thus the agreement with the current calculations is satisfactory.

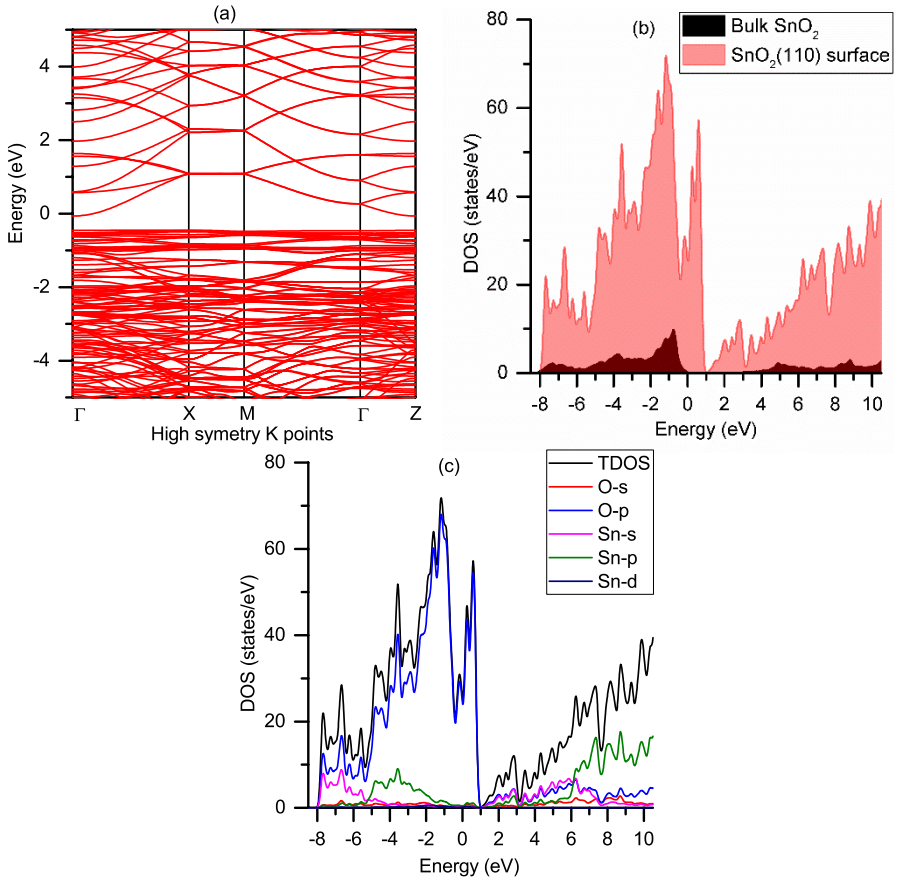

Figure V. 6: (a) band structure of stochiometric SnO2 (110) surface, (b) comparison between surface and bulk DOS and (c) total and parial DOS of the stoichiometric surface.

5.2.2.2. Adsorption on stochiometric SnO_2 (110) surface

The experimental results cited in [195] [196] indicate that before the gas target is introduced, oxygen species such as O_2^- or O^- are adsorbed on the surface of SnO_2 and attract electrons from SnO_2, resulting in surface resistance increase. The following section investigates the possible adsorption modes for oxygen molecules on the surface of SnO_2 (110). It was demonstrated first that, rather than the stoichiometric surface, oxygen molecules can be adsorbed on the SnO_2 (110) surface with oxygen vacancies. Different modes for the adsorption of oxygen molecule O_2 on the stoichiometric SnO_2 (110) surface have been simulated, and optimized results are shown in Figure V. 7. For the S1 model, meanwhile molecular adsorption at the Sn site was supposed, S2 model proposed the possibility for an adsorption in a bridging oxygen site. In S3 and S4 models, it is suggested a horizontal adsorption on the Sn site with two different orientations.

The sign and value of the adsorption energy can be used to determine the possibility of an adsorption mode to be occurred. The following equation was used to express the adsorption energy:

$$E_{ads} = E_{slab} + E_{mol} - E_{slab+mol} \qquad Eq.\ V.\ 2$$

where $E_{slab+mol}$ is the total energy of the relaxed system containing the surface and the molecule, E_{slab} and E_{mol} are the energy of the relaxed surface and the relaxed isolated molecule, respectively.

Positive adsorption energy, according to this equation, indicates that the adsorption process is exothermic, and the adsorption system is thermodynamically stable. A negative value, on the other hand, indicates an endothermic and unstable adsorption.

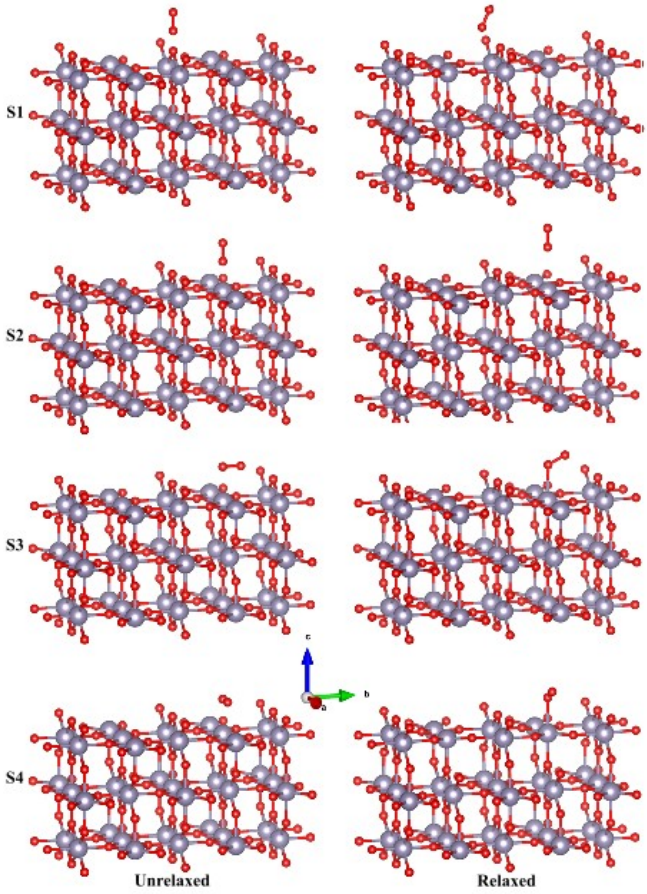

Figure V. 7: Models used for the study of the adsorption of oxgyn molecules on the stoichiometric SnO2 (110) surface.

The isolated oxygen molecule has been simulated in a cube of 20Å, size big enough to isolate the molecule to avoid simulating a periodic system. The adsorption energies calculated for modes S1, S2, S3, and S4 are -1.452, -0.384, -0.150 and -0. eV, respectively (Table V. 2). For the adsorption of oxygen molecules (O_2) on the stoichiometric SnO_2 (110) surface, all calculated adsorption energies are negative. Because of these negative adsorption energies, oxygen molecules O_2 cannot be adsorbed on the stoichiometric SnO_2 (110) surface, as above mentioned because the adsorption process in this case is endothermic and the system is thermodynamically unstable. Our calculations based on PWPP with GGA produce comparable results to those based on VASP with GGA [197]. The experimental results show that SnO_2 performs well as a gas sensor. It is expected that oxygen adsorption on the surface of SnO_2 is related with the reduction of the surface by creating oxygen vacancies. Experimental

works revealed that the SnO_2 surfaces were expected to be slightly reduced [198]. Then, a study concerning the formation of surface oxygen vacancies is needed. In the next section, the most probable models for the formation of oxygen vacancies at the surface of SnO_2 were investigated in order to study the interaction of oxygens with the reduced surface created by removing one oxygen atom from the stoichiometric SnO_2.

Table V. 2: Calculated total and adsorption energies for the relaxed systems considered for the study of the adsorption of oxygen molecules on the stoichiometric SnO_2 (110) surface.

Model	Et (eV)	Ead(eV)
S1	-74938.82642	-1.451939983
S2	-74939.89389	-0.384461757
S3	-74940.12836	-0.149997727
S4	-74940.15709	-0.121270739

5.2.2.3. Formation of surface oxygen vacancies

Three oxygen vacancy sites (Figure V. 8) were taken into consideration to create modes to optimize defected SnO_2 (110) surfaces. The V1 mode is built by removing one bridging oxygen atom, the V2 and V3 have been created by removing an in-plane oxygen atom or a subsurface one, respectively.

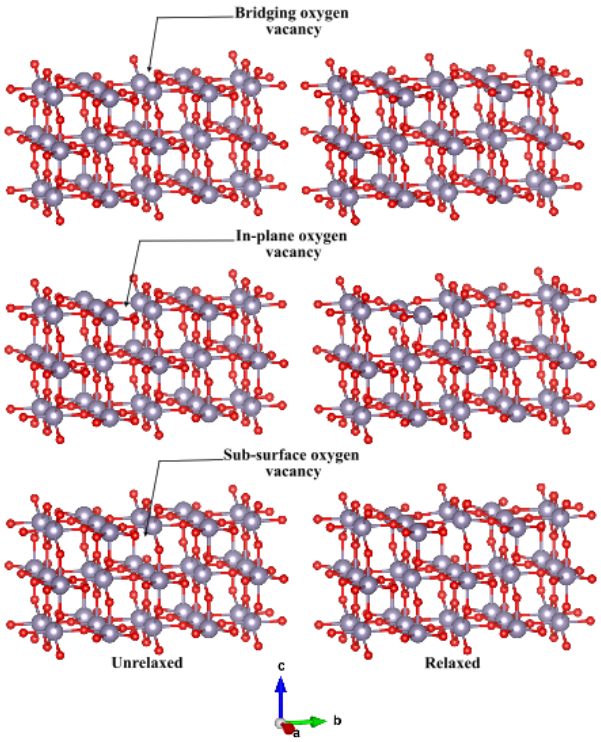

Figure V. 8: Models used for the study of the formation of surface oxygen vacancies.

The formation energies for the three modes V1, V2 and V3 were calculated following the equation below:

The oxygen vacancy formation energies of V1, V2 and V3 modes are 3.093, 3.402 and 4.297 eV respectively, as reported in Table V. 3. These values suggest that the oxygen vacancy formation energies in the topmost layer (modes V1, V2) are much lower than the subsurface one (mode V3). Thus, the formation of oxygen vacancies in the topmost layer is more probable than the formation of vacancies in the subsurface. It is obvious that the vacancy formation energy of bridging oxygen (V1 mode) is the lowest. Then, the V1 mode was considered in the next adsorption step, i.e. adsorption of oxygen species on defected SnO_2 surface.

Figure V. 9 (left) depicts the band structure of a stoichiometric SnO_2 (110) surface (a1) and the defected surface with a bridging (b1), in-plane (c1), or subsurface (d1) oxygen atom removed. There are significant differences with respect to the stoichiometric surface, particularly with regard to the intragap states. The removal of the most exposed bridging oxygen atoms results in the formation of a dispersed band within the forbidden gap (see Figure V. 9 (b1)). The observed trend is consistent with the experimental literature, which reports that when a stoichiometric surface is reduced, energy levels extend from the top bulk VB below the CBM [199]. When the vacancy is in the in-plane positions, a different picture was observed. In this case, the levels within the gap are more similar to those of bulk SnO_2, with a small, dispersed band above the top bulk VB, as shown in Figure V. 9 (c1). Considering the case of subsurface oxygen vacancy, the new dispersed band inside the forbidden gap is similar to the one observed in the case of the bridging oxygen vacancy, but in this case the band is becoming closer to the CBM (Figure V. 9 (d1)). It is worthy to remind that the GGA-PBE approximation that is used in this work underestimates the band gap value and the exact position of the highest occupied and lowest unoccupied levels. Thus, the new band created due to the impurity state is overlapping with the CBM.

In Figure V. 9 (right) it is reported the Total Density Of States (TDOS) and the contribution of each atom on the different orbitals presented by the partial/Projected DOS (PDOS) for both the stoichiometric SnO_2 (110) surface (a2) and the defected surface with a bridging (b2), in-plane (c2), or subsurface (d2) oxygen atom removed. Surface reduction, as previously stated, results in the formation of intragap surface states [199] [194], but the oxidized (stoichiometric) surface also exhibits surface states (see Figure V. 9 (a2)). This explains why the annealing process in air does not completely remove the intragap states. The stoichiometric surface is characterized by occupied intragap states above the top bulk VB at about 1eV, according to our findings. This corresponds to previous calculations [200] [193] and experiments [194]. Experimentally, when the surface is reduced, a continuum of occupied states covering a wide energy range inside the bulk band gap is observed [199], which is

evident from Figure V. 9. The main peak on top of the bulk VB has a smaller value than the associated stoichiometric surface peak. Meanwhile, the occupied states cover a wider energy range inside the bulk gap region. The decrease in the band gap energy due to the creation of the vacancy is clearly visible from Figure V. 9 and Figure V. 11. In the last, is shown the trend of the formation and the Fermi energies as a function of vacancy type. The PBE approximation can be trusted investigating qualitatively the electronic band structure of semiconductors. It can be seen from Figure V. 10, as much as the vacancy is deeper as much as the Fermi energy goes close to the CB. This behavior seems very promising for technological applications in general, and for gas sensing in particular since oxygen vacancies may enhance the sensing performance of SnO_2 by facilitating the charge transfer occurring at the surface of the material and then lowering the temperature that the sensor needs to be thermo activated. Nevertheless, as it can be seen also from Figure V. 10, the deeper the vacancy the higher is the energy needed to create it, which means that even the subsurface oxygen vacancies seem promising for technological application, they need more power to be created. Hence, it can be said that oxygen vacancies in the bridge are the best candidates for real application because they require less energy to be formed and they give a specific impact on the electronic structure of the semiconductors.

Table V. 3: calculated total and formation energies for the models representing the defected surface.

Model	Et (eV)	Efor (eV)
V1 (Br)	-73640.96197	3.092718625
V2 (Pl)	-73640.65254	3.402153291
V3 (Ss)	-73639.75788	4.296815519

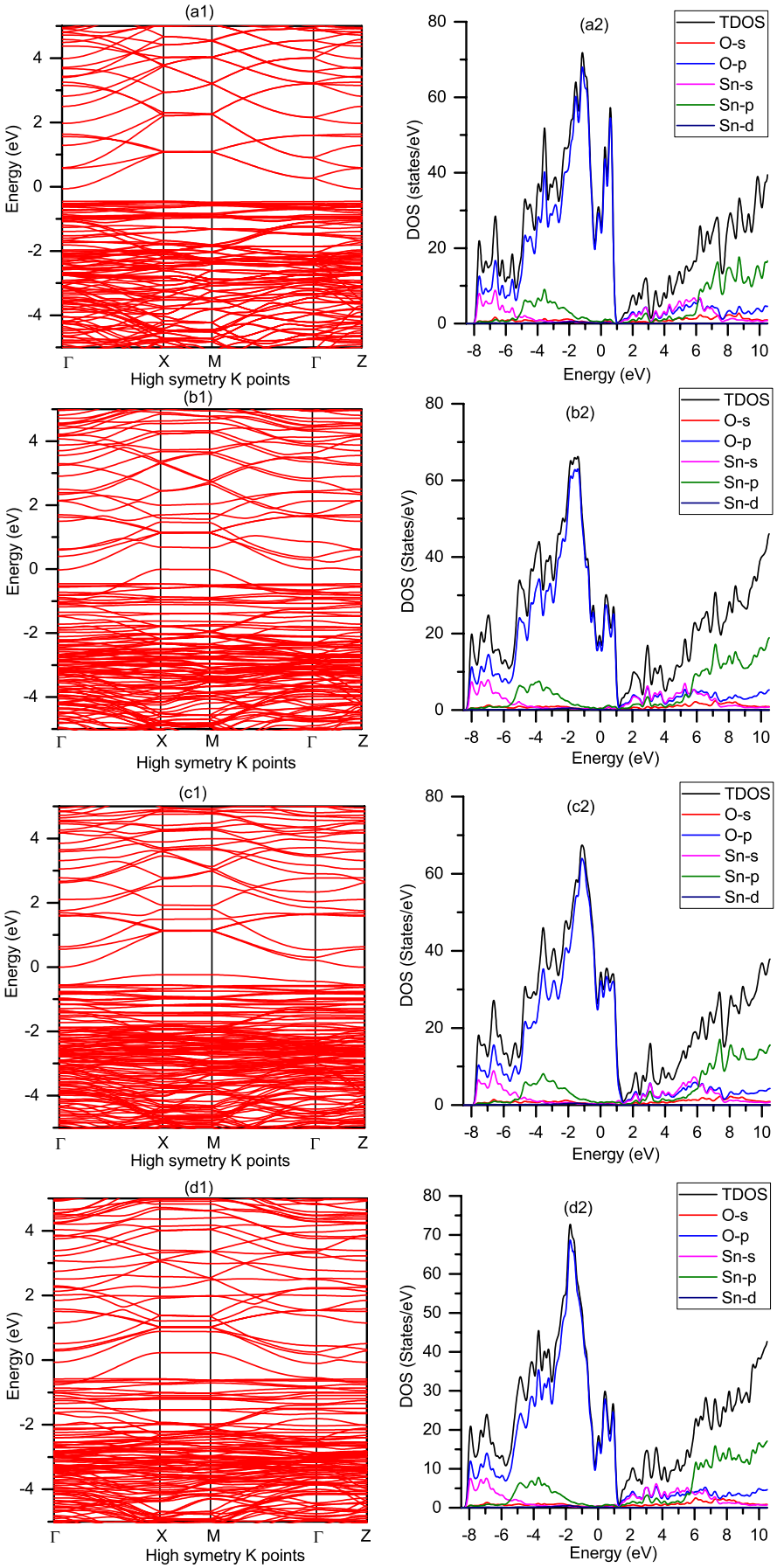

Figure V. 9: (left) band structures of the stoichiometric and defected SnO2 (110) surface. (right) the corresponding total and partial DOS.

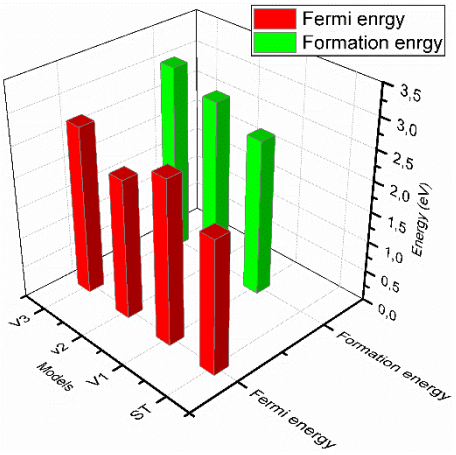

Figure V. 10: Variation of the formation and the Fermi energies in the different models.

5.2.2.4. Adsorption of oxygen molecules on defective SnO_2 (110) surface

The adsorption of oxygen molecules on defected SnO_2 (110) surface (V1 mode) was studied using four geometries: (D1) O_2 molecular adsorption at the Sn site adjacent to the bridging oxygen vacancy, (D2) insertion of an O_2 molecule into the vacancy, (D3) and (D4) straddled adsorption on the vacancy with two different orientations. Figure V. 11 depicts the optimized geometries of stable adsorption after the relaxation of the systems. Adsorption energies calculated, in this case, for D1, D2, D3, and D4 modes were 2.562, 1.956, 2.561and 2.561 eV, respectively. It can be noticed that the adsorption energies of the systems containing both surface and oxygen molecules in the case of D1, D3 and D4 modes are the highest, implying that the total energy is always greater than the sum of the isolated O_2 molecule and the relaxed V1 mode. Therefore, the oxygen gas molecules need higher energy to be exothermically adsorbed on the defected surface by the mode D2, Because of its lowest-positive adsorption energies. While they can be easily exothermically adsorbed on the defective surface SnO2 with D1, D3 and D4 modes.

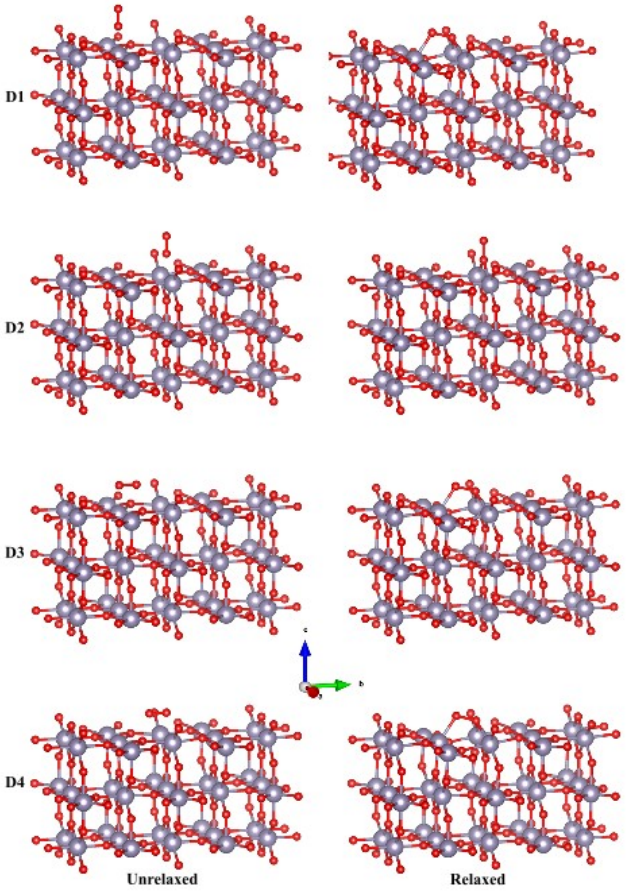

Figure V. 11: Models used for the study of the adsorption of oxygen molecules on the defected surface.

Table V. 4: total and adsorption energies for the relaxed systems.

Model	Et (eV)	Ead(eV)
D1	-74507.673	2.56190885
D2	-74507.068	1.95647941
D3	-74507.672	2.56123643
D4	-74507.672	2.56082596

5.3. Conclusions

In this section, it was carried out an investigation on how surface oxygen vacancies can enhance the sensing performance of SnO_2, by using first principles calculations. In the first step, it was proved that the stoichiometric SnO_2 (110) surface cannot interact with oxygen molecules from the surrounding atmosphere, then the possible models for the formation of oxygen vacancies on the surface of SnO_2 were investigated. It was demonstrated that the oxygen atoms in the bridge are the easier one to be created, while creating subsurface oxygen vacancies gave a significant shift of the Fermi level towards the CBM. For sensing application, the subsurface oxygen vacancies are more useful, but since the aim of the work is to enhance the sensing performance of the device as well as providing a simple and low-cost method for oxygen vacancies formation, it can be concluded that the bridging are the most accurate for such a technological application. The energy needed to create them is the lowest one between

the models studied here, and the Fermi energy is closer to the CB with respect to the stoichiometric surface and to the model containing the in-plane oxygen vacancies. This may enhance the adsorption process of oxygen molecules from air resulting in an enhancement of the surface reactivity and the charge transfer occurring at the surface during the interaction with the analyte.

6. Nickel loaded phosphorene

Since its discovery [201, 202], graphene is widely studied by many researchers [203] due to its excellent electronic, optical and mechanical properties. Since then, many kinds of two-dimensional (2D) materials attracting attentions. The quantum confinement effect, high specific surface area and excellent flexibility of two-dimensional materials cause them exhibit unique functions which are difficult for other dimensional materials. Because of the high surface to volume ratio and low electrical noise they have a great potential in gas sensors applications. However, the gapless characteristic of graphene limits its applications, this inspired more researches of other two-dimension materials which have similar properties with a suitable band gap. Black phosphorus (bP) was regarded as the most stable allotrope among the group including red, white and violet phosphorus. The successful fabrication of the exfoliated bP and evaluation of its outstanding performance in field-effect transistors has been reported in 2014 [204, 205]. Generally, this method is widely for the fabrication of 2D materials such as graphene, MoS_2, BN and could be classified into two aspects, top-down and bottom-up. The most popular top-down methods are cleavage with tape, liquid-phase exfoliation, and plasma-assisted fabrication. The principle of these methods is to remove the weak Vander-Waals interactions between the different materials layers. The bottom-up methods include chemical vapor deposition and hydrothermal synthesis. Compared with bottom-up methods, top- down methods have been reported for successful fabrication of phosphorene [206, 207]. The band gap, electronic structures, reaction activities of phosphorene could vary, which corresponds to the layer numbers, surface defects, doping and configurations of phosphorene. All these parameters could be directly related to the phosphorus and to the fabrication methods. DFT calculations show that the band gap and electronic properties could be tuned by adatoms doping including transition metallic and nonmetallic atoms, such as S, Si, O, Ge. Compared with theoretical studies, very few works have been published relating to gas molecule adsorption on phosphorene, and the majority of those have focused on pristine phosphorene [208, 209]. Small molecules such as CO, H_2, H_2O, NH_3, NO, and NO_2 are physisorbed on phosphorene. There are also some theoretical studies of interactions between doped phosphorene and small molecules. Lalitha et al. [210] studied the interactions between small molecules and Ca-doped phosphorene. The authors demonstrated that Ca could help improve the affinity of gas molecules on phosphorene. Li et al. [211] studied the adsorption of H_2 on Li-doped phosphorene and reached a similar conclusion. The same trend was deduced in earlier graphene-related studies. Caporali et al. [212] demonstrated a stability and functionality improvement of nickel-decorated Phosphorene (Ni/bP) films. In our group, it is proved the same enhancement in the stability and functionality using a simple, reproducible and affordable deposition technique, highlighting good performance of Ni decorated phosphorene used as sensing element to detect NO_2 in sub-ppm concentrations [213, 214]. Looking in literature, experimental investigations

on Ni loaded phosphorene were done, but very few theoretical studies on how nickel influences the physical-chemical properties of monolayer black phosphorus for gas sensing application are available. Therefore, in the present work, first principles study in the framework of DFT was carried out in order to deeply understand the sensing mechanism of Ni decorated phosphorene towards NO_2 gas.

6.1. Computational details

In this part of the work, the plane wave with pseudo-potential (PWPP) approach has been adopted for the solution of the Kohn-Sham equations. It is based on atomic pseudo-potentials and a set of plane wave basis as implemented in the quantum-espresso code. This approach was used because it is very efficient for dealing with extended periodic systems. In this case, spin polarized calculations were performed using generalized gradient approximation (GGA) with Perdew-Burkc-Ernzerhof (PBE) parameterization for the exchange-correlation function and ultrasoft pseudo-potentials to represent the ion nuclei. The cut-off energies for the wave functions and charge density were optimized for the minimum total energy of the system and the optimized values were set to 37 and 333 Ry respectively. The need to use a higher value of the charge density cut-off is due to the fact that we need an accurate estimation of the electrostatic potential. For the number of K-points in the first Brillouin zone and since the lattice parameters *a, b* and *c* are very different it is supposed that optimizing one by one will give more accurate results. The optimization in this case has been done by fixing the number of K-points in two directions and changing the third one and the optimized combination was set to 6*1*4, this combination has been used for Self-Consistent Field (SCF) cycles while for density of states calculations it was increased it to 18*3*12. The convergence criteria have been fixed for all calculations in this section, and it is set to 10^{-6} Ry for the total energy of the system and 1mRy/Bohr for the total force acting on atoms. In addition, and in order to treat the van der Waals interactions, the van der Waals DFT (vdW-DF) with the optB88 (optB88-vdW) [215, 216] was adopted for the exchange functional during the relaxation of the systems considered in this section.

6.2. Results and discussion

6.2.1. Bulk black phosphorus

- **Structural optimization**

Before studying the impact of the decoration of phosphorene with nickel, one needs to optimize the bulk black phosphorus that will be used to create phosphorene monolayer and then decorate it with nickel. For this purpose, the initial structure used was the orthorhombic phase published in [217]. Individual atomic layers are stacked together by Van der Waals interactions to form the layered black phosphorus (Figure VI. 1-a). Each phosphorus atom, in a single layer, is covalently bonded with three adjacent phosphorus atoms, as shown in Figure

VI. 1-a. Bulk black phosphorus can be exfoliated to produce few-layers phosphorene. The bulk black phosphorus has Cmce (No. 64) space group with a= 3.31645 Å b=10.4843 Å c=4.37935 Å. These parameters have been used to create our model and then the later has been relaxed using the plane wave basis with pseudo-potentials method. The relaxation method used in this case was the Broyden_Fletcher_Goldfarb_Shanno (BFGS) algorithm, and the atomic positions were allowed to fully relax until the internal residual forces acting on each atom were less than 1 mRy/ Bohr (Figure VI. 1-b.

In Table VI. 1, it is reported the calculated structural parameters of bulk black phosphorus presented in Figure VI. 1-a using PWPP method in this work, and those identified in literature both experimental and theoretical results. It can be seen from this table that our relaxed structural properties using the van der Waals DFT are in good agreement with experimental reported values [217] as well as with other theoretical calculations using GGA-PBE approximation implemented in the VASP code [218]. This confirms the approach and the optimized parameters used i.e., $E_{cut\text{-}off}$ and K-points used in our calculations.

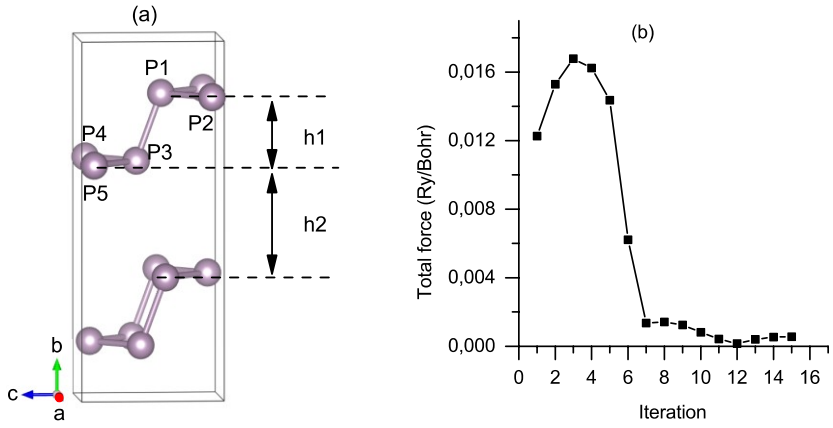

Figure VI. 1: crystal structure of bulk black phosphorus (left) and variation of the total forces acting on atoms during relaxation of the system (right).

Table VI. 1: Calculated structural parameters of bulk black phosphorus in this work compared to the experimental and theoretical results reported in literature. $\theta_1 = (\widehat{P_1P_3P_5})$, $\theta_2 = (\widehat{P_4P_3P_5})$, $d_1 = (P_1 - P_2)$, $d_2 = (P_1 - P_3)$. **Data converted to Cmce for better comparison.*

	a (Å)	*b (Å)*	*c (Å)*	*θ_1 (°)*	*θ_2 (°)*	*h1 (Å)*	*h2 (Å)*	*d1 (Å)*	*d2 (Å)*
This work	3.310	11.308	4.567	103.51	95.86	2.122	3.530	2.229	2.265
Calc. [218]	3.308	11.099	4.536	N/A	N/A	N/A	N/A	N/A	N/A
Exp. [217]*	3.316	10.484	4.379	102.11	96.38	N/A	N/A	2.224	2.245

The calculated density of states (DOS) and band structure of bulk black phosphorus are presented in Figure VI. 2 showing that black phosphorus is a semiconductor material with a direct band gap of 0.14 eV calculated using GGA_PBE, consistent with recent GGA-PBE studies [219], while it is underestimated with respect to the reported experimental value (0.3

eV [205]), which is a common conclusion for GGA_PBE approximation, i.e., underestimation of band gap value. The VBM and the CBM are both located at Γ point that make the material a direct band gap semiconductor. Looking at the DOS graph and at the partial density of states (PDOS) for *s* and *p* orbitals of phosphorus atom, it can be said that the dominant character in both VB and CB of black phosphorus is the *p* character.

❖ **Electronic structure**

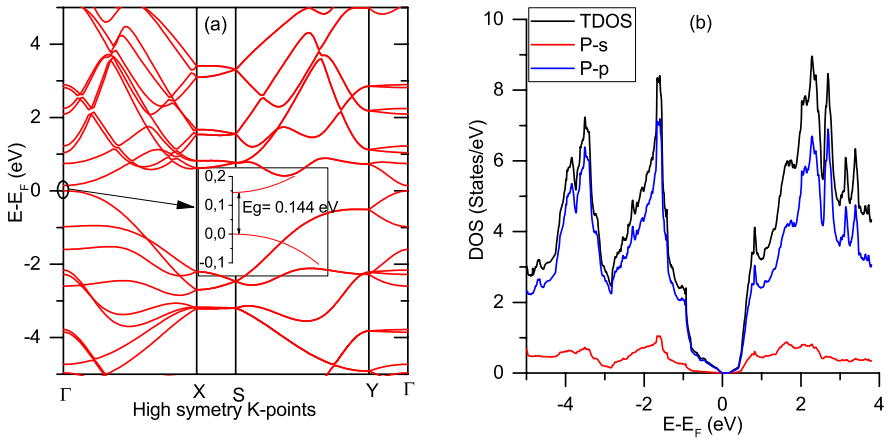

Figure VI. 2: calculated electronic band structure (left) and the density of states (right) for the bulk black phosphorus.

6.2.2. Monolayer Black phosphorus

❖ **Structural optimization**

The single layer of black phosphorus was cleaved from the previously optimized bulk structure, Figure VI. 3 shows the side and top view of phosphorene. In contrast to flat shaped graphene, the top and side views of phosphorene reveal that the material is made up of repeating puckered hexagonal structures due to the sp^3 hybridization. A (2*1*2) supercell was used that gave us 16 phosphorus atoms. In order to avoid the interactions between periodic images a vacuum of 20 Å has been used, this value is large enough for this purpose. The structure optimization method is critical for performing a significant calculation. Here, two approaches are used, the first is an all-electrons method (FP-LAPW) implemented in Wien2k code and the second is a pseudo-potential with plane waves method using the quantum espresso package. In the case of the Wien2k code, the GGA_PBEsol approximation was used for the relaxation of the system while in the other case (using quantum espresso) the vdW-DFT was used. The calculated structural properties using both methods and those identified in literature are reported in Table VI. 2. The bond length of *P-P* in our simulation model of pure phosphorene is d1=2.23 Å in the zigzag direction and d2=2.26 Å in the armchair direction. The difference between the phosphorus atoms in the top and the bottom of the layer is approximately h1=2.12 Å. Li et al. [211] reported 2.23 Å and 2.26 Å for the corresponding *P-P* bond lengths in the zigzag and armchair directions, respectively, as well as 2.21 Å for the layer width. Lalitha et al. [210] found 2.21 Å and 2.26 Å for the corresponding *P-P* bond

lengths in the zigzag and armchair directions, respectively. Our findings are in line with reported results in literature.

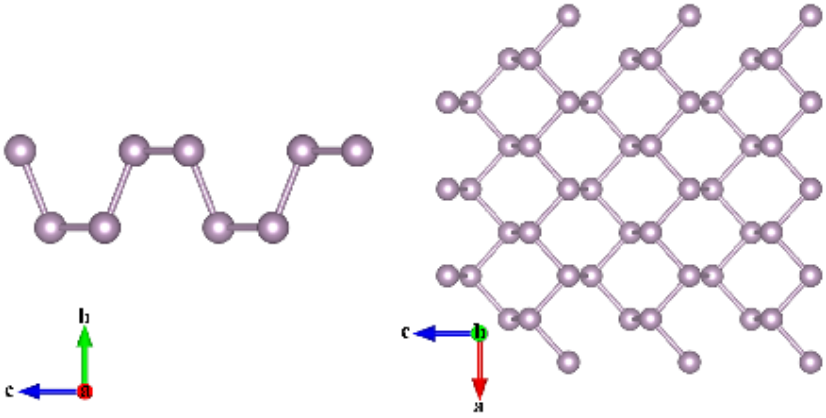

Figure VI. 3: Side and top view of phosphorene of phosphorene.

*Table VI. 2: Calculated structural parameters of phosphorene in this work compared to the experimental and theoretical results reported in literature. *Data converted to Cmne for better comparison.*

		This work		Literature	
		PWPP	FP-LAPW	Calc. [218]	Exp. [217]
Lattice parameters	*a (Å)*	3.310	3.316	3.298	3.316
	c (Å)	4.57	4.38	4.627	4.38
Bond angle & length	θ_1 (°)	104.07	103.50	104.1	102.11
	θ_2 (°)	95.85	98.38	95.9	96.38
	d_1 (Å)	2.23	2.12	2.22	2.22
	d_2 (Å)	2.26	2.22	2.26	2.24
	h_1(Å)	2.12	2.09	2.51	

❖ **Electronic structure**

As mentioned earlier, the black phosphorus band gap is a layer dependent material which goes from 0.3 eV for bulk to 1.51 eV for monolayer [219]. Our DFT calculations are in good agreement with this trend even if the band gap values obtained are underestimated due to the approximation that is adopted (i.e., GGA_PBE). As shown in Figure VI. 4-a, the phosphorene still possesses a direct band gap with the reduction of the number layers down to the monolayer. The band gap is located at the Γ point with a value of about 0.9 eV using the GGA_PBE approximation within the PWPP method, this value is comparable to other

calculated values using GGA_PBE approximation [219]. In other words, our calculations are in agreement with the layer dependency of the band gap value (i.e., the band gap energy increased from 0.14 eV in the case of the bulk to 0.9 eV in the case of monolayer).

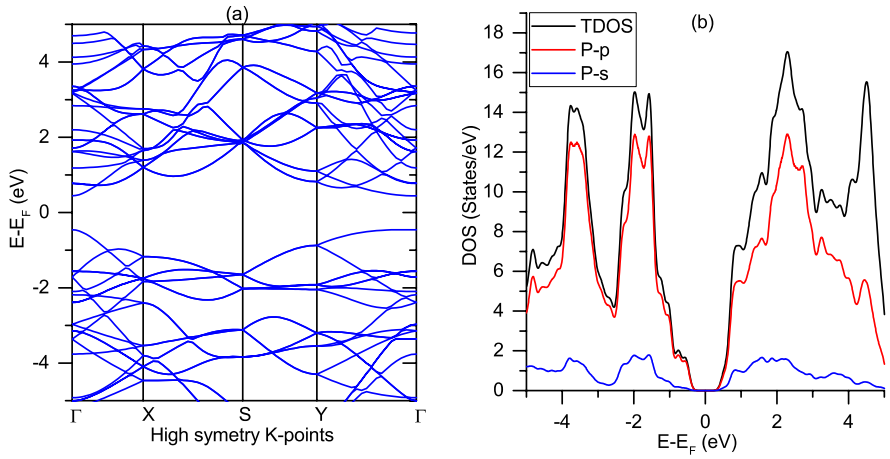

Figure VI. 4: calculated electronic band structure (left) and the density of states (right) for the monolayer black phosphorus.

6.2.3. Nickel decorated phosphorene

To study the impact of Ni atom on the physical chemical properties of phosphorene, the Ni atom was placed in the hollow (H) site at h=1.01Å as a vertical high of the adatom from the phosphorene layer (Figure VI. 5). H site was chosen since it is the most stable adsorption site for Ni, and the distance between Ni adatom and phosphorene layer has been chosen based on previous study by Hu T. et al. [207]. After the relaxation of the system, the calculated vertical high of the nickel atom with respect to the closer phosphorus atom was found to be 0.999 Å which is very close to the identified one in literature (i.e., 1.01 Å).

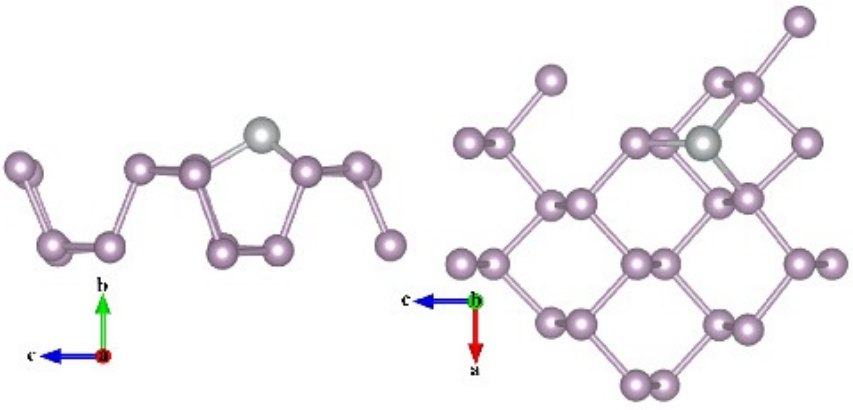

Figure VI. 5: Position of nickel atom on the phosphorene layer.

❖ **Impact of nickel adatom on the electronic structure of phosphorene**

After relaxing our system, GGA_PBE approximation was adopted to calculate the band structure and DOS of nickel decorated phosphorene. Figure VI. 6 illustrates the band structure and the corresponding DOS graphs. Before discussing these graphs, it is worthwhile

to recall the principle of doping in semiconductors: A semiconductor doped with ionized impurities (meaning that the atoms of the impurity have donated or accepted electrons) will therefore contain free carriers. Shallow impurities require little energy, (i.e. typically around the thermal energy *KT* or less) to be ionized. Deep impurities require much greater energies to be ionized, that only a fraction of the impurities in the semiconductor contribute to the free carriers. Deep impurities, which are more than five times the thermal energy away from either band edge, have very little chance of being ionized. In other words, on one hand, if the impurity states appear close to the top of the VB (bottom of the CB) they are called shallow acceptor level (shallow donor level). On the other hand, they are called deep acceptor (donor) levels if they appear close to the middle of the forbidden band gap. It is clear from the band structure graph that with the introduction of the nickel atom, a new band appears to be created in the band gap region just below the Fermi level. This new energy level is corresponding to the shallow acceptor level since it lies between the top of the VB and the just below the Fermi level (Figure VI. 6-b-c). The band gap calculated in this case was an indirect band gap with a value of about 0.68 eV (Figure VI. 6-a). The electronic configuration of phosphorus is *[Ne]* $3s^2 3p^3$ while the nickel one is *[Ar]* $3d^8$ $4s^2$. From the DOS graph (Figure VI. 6-b), the corresponding peak of the new band created due to nickel can be clearly seen. Before the introduction of the nickel atom both top of the VB and bottom of the CB are mainly composed of states coming from the *p* orbitals of the phosphorus atoms. Introducing the nickel atom it can be clearly seen the hybridization of *p* orbitals from phosphorus atoms and *d* orbitals from nickel atoms. The shallow acceptor level in this case can facilitate the electrons exchange between the top of the VB and the target gas. Thus, increasing the holes concentration on the VB may enhance the reactivity of the material surface.

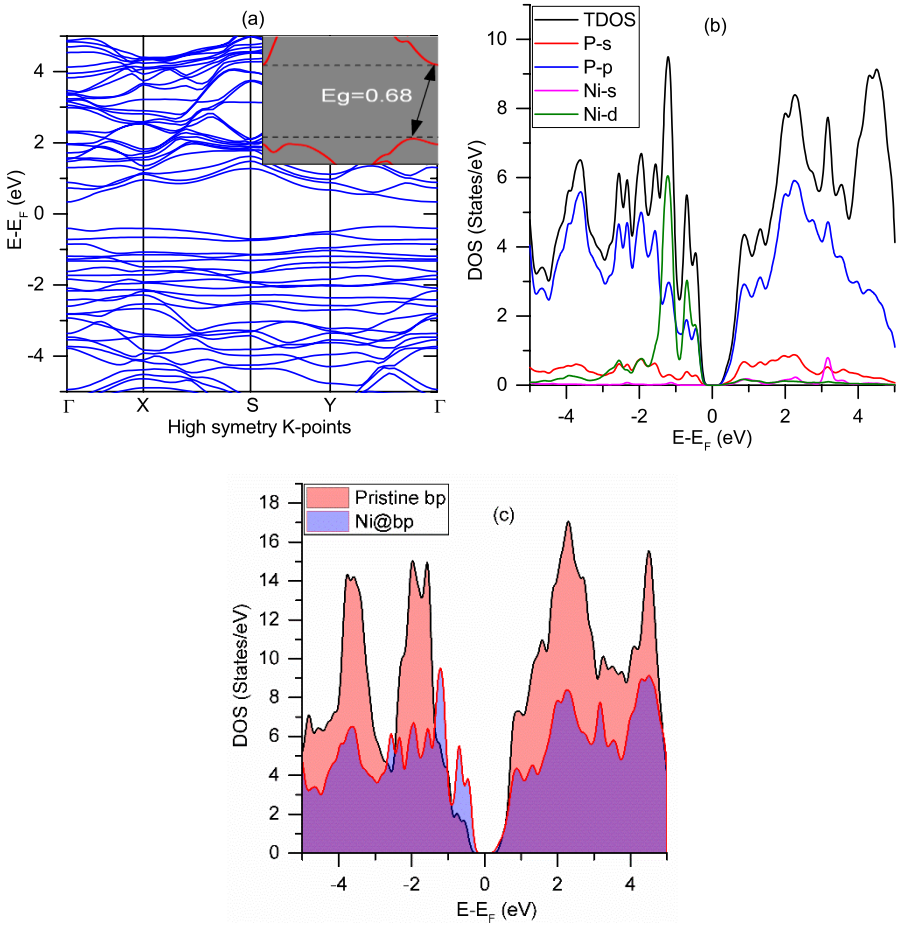

Figure VI. 6: (a) calculated electronic band structure and (b) total and projected density of states of nickel loaded phosphorene. (c) comparison of TDOS of the pristine and nickel decorated phosphorene.

The minimum energy needed for an electron to go from the surface to the vacuum is defined as the work function (Φ), which can be expressed as $\Phi = V_{vac} - E_F$, where V_{vac} is the electrostatic potential in the vacuum region, and E_F is the electrostatic potential at Fermi level. The work function values were calculated for pristine and nickel decorated phosphorene in order to understand the stability (i.e. non degradation of the material) of the sensor device produced using nickel decorated phosphorene as a sensing element. The calculated work functions of pristine monolayer black phosphorus and nickel decorated phosphorene were about 4.59 and 4.49 eV, respectively. The obtained value in the case of pristine phosphorene is in good agreement with other reported values using the same approximation (i.e. GGA_PBE) [220] (i.e. 4.50 eV) even if these values are underestimated but the trend in the change can be trusted using GGA_PBE approximation. Based on the study reported in [221], the monolayer phosphorene can produce excitons under ambient light due to its large band gap (i.e. about 1.5 eV). In other words, because of the position of the redox potential of O_2/O_2^- (located inside the forbidden band gap region in the case of monolayer bP), the photo-generated electrons will pass from the phosphorene CB to the O_2 on the surface, generating O_2^- that is likely to irreversibly react with the p-doped phosphorene. Thus, causing the degradation of the material forming oxidized phosphorus species (POx), fundamentally

altering the electronic properties of the material. However, in their study Zhou *et al.* are reporting also by increasing the number of layers the band gap decreases and both VBM and CBM move close to each other until the CBM overlaps/becomes under the redox potential of O_2/O_2^- which can make the material more stable. In our case, since the trend of band gap and work function (comparing pristine and nickel decorated phosphorene) is similar to the study reported in [221], it is assumed that by introducing the nickel atom the CBM is shifting towards the redox potential of O_2/O_2^- as it is schematized in Figure VI. 7. Indeed, in our calculated DOS reported in Figure VI. 6, the movement of the top of the VB towards high energies is very clear and also the CBM has been slightly shifted down to low energies. Considering the approximation applied, this movement of the bands can be taken in consideration even if it consists in a small shift. The overall conclusion from these analyses can be translated in the stability of the sensors fabricated using nickel loaded phosphorene rather than the one based on pristine phosphorene.

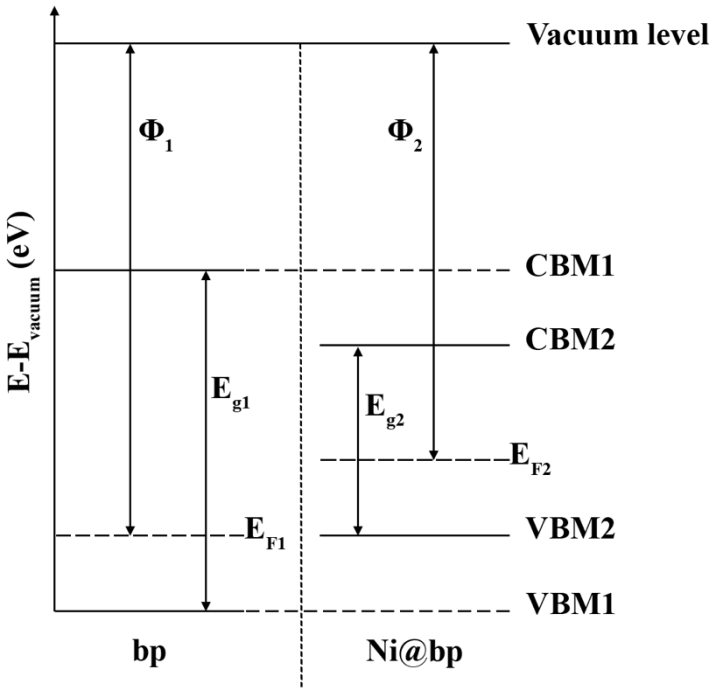

Figure VI. 7: Schema illustrating the movement of bands level when introducing nickel atom.

6.2.4. Sensing mechanism of nickel decorated phosphorene toward NO_2

In general, gas sensors are exposed to ambient atmosphere before interacting with the target gas is introduced. Firstly, oxygen molecules from the surrounding atmosphere can be adsorbed on the surface of the active layer, these adsorbed oxygen molecules will react with the electrons located at the surface of the material become activated oxygen ions (O^-), this results in a creation of a depletion layer by decreasing the electron density. When the target gas is introduced (NO_2), the analyte molecules react with nickel atoms on the surface of the

layer resulting in an increase of holes density, since the electrons participating in this reaction are coming from the phosphorus layer, and finally results in an increase of conductance. The reactions summarizing these processes are reported in the first chapter.

Moreover, possible adsorption processes on pristine and on nickel decorated phosphorene were theoretically studied by means of DFT calculations. In addition, the charge transfer process that occurs during the reactions was considered at both stages, the adsorption of oxygen molecules from the surrounding atmosphere and the interaction of NO_2 gas molecules with the pre-adsorbed oxygens. In Figure VI. 8 the adsorption sites that will be considered are reported.

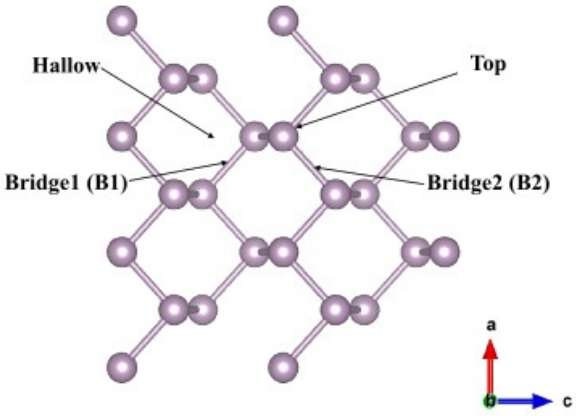

Figure VI. 8: Adsorption sites considered in this work.

6.2.4.1. Adsorption of oxygen species

In this part, results obtained for the adsorption of oxygen molecules on both pristine and nickel decorated phosphorene are reported.

Firstly, eight models were considered in order to simulate the possible interaction between oxygen molecules and the surface of pristine phosphorene, (i.e. O1…O8). Parallel adsorption of the O_2 molecule on the layer of phosphorene in the T, H, B1 and B2 sites are illustrated in Figure VI. 8 (O1, O2, O3 and O4 models, respectively) then, perpendicular adsorption in the same sites (O5 to O8) was considered. Figure VI. 9 shows the initial and the final state of the systems after the relaxation. Table VI. 3 summarizes the calculated adsorption energies for each model. The resulting negative adsorption energy means that the proposed reaction cannot happen, i.e., the adsorption process is endothermic and the adsorption system is thermodynamically unstable (case of O2, O3, O6, O7 and O8). On the contrary, the calculated adsorption energies for models O1, O4 and O5 were positive values, specifically 3.76, 3.9 and 3.76 eV. In these cases, the system is thermodynamically stable and adsorption process is exothermic or extremely exothermic, releasing about 4 eV of energy per O_2 molecule. In addition, the results showed that O_2 molecules physisorption state is only a metastable state, and that O_2 forms two dissociated O^- atoms on the monolayer black phosphorus surface through dissociative adsorption. One can also observe that the adsorption

energies for models O1 and O5 are equal, which means that the oxygen molecule is adsorbed and the related energy is not affected by the orientation of the O_2 molecule. On the contrary, the adsorption site clearly impacts on the adsorption energy i.e., the O_2 molecules cannot be adsorbed in the H and B1 sites while they prefer the B2 and T sites and more precisely the B2 site with an adsorption energy about 3.9 eV. Such a high adsorption energy may allow the oxidation of phosphorene at low temperature.

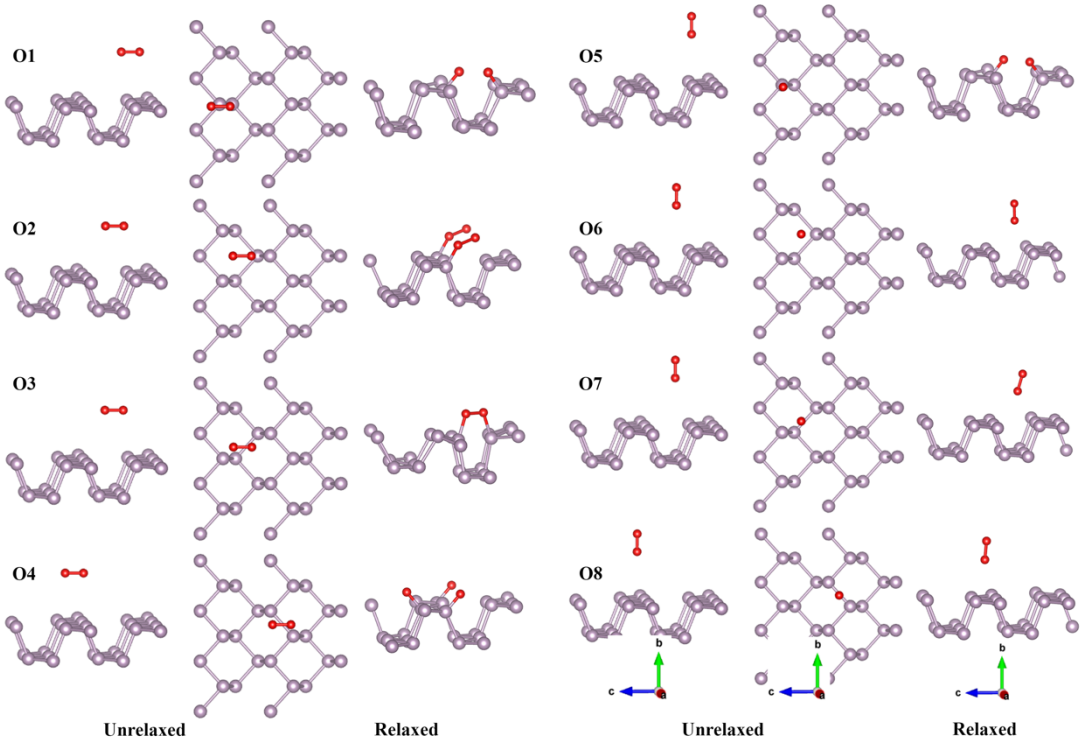

Figure VI. 9: Models used to simulate the interaction between oxygen molecules and the pristine phosphorene.

Table VI. 3: Adsorption energies for models reported in Figure VI. 9

Model	O1	O2	O3	O4	O5	O6	O7	O8
E_{ads} (eV)	3.76	-0.53	-0.18	3.9	3.76	-1.07	-1.08	-1.09

For nickel decorated phosphorene, eight models were taken into account in order to investigate the adsorption of oxygen molecules on its surface (Figure VI. 10). First, perpendicular adsorptions of O_2 molecule on the Ni atom, B2, H and T sites were considered (case of N1, N2, N3 and N4). Then parallel adsorptions with one atom of oxygen molecule coordinated to the same sites, as for the perpendicular adsorption, were considered (case of N5, N6, N7 and N8). Positive adsorption energies were obtained for all proposed models, this means that the systems are thermodynamically stable and the adsorption processes are exothermic. Investigating the values obtained for each model, it can be seen that in the case of adsorption using models N1, N2, N5, N6 and N8 the related energies are lower than the other

cases and the oxygen molecule does not dissociate and it reacts only with the nickel atoms decorating the layer. Using N3, N4 and N7 i.e., perpendicular adsorption on H, T and parallel adsorption with one oxygen atom coordinated to the H site, the adsorption energies are higher and the oxygen molecule dissociates where one oxygen atom reacts with the nickel on the surface and the other one reacts with the phosphorus atoms from the layer. This may explain the stability and non-degradation of nickel decorated black phosphorene in ambient air. Indeed, introducing nickel some of oxygen molecules from the surrounding atmosphere adsorb on the Ni atoms slowering the oxidation process with respect to pristine phosphorene where all oxygens from the environment dissociate and react with phosphorus atoms (case of adsorption on pristine phosphorene reported in the previous paragraph). The relaxed structures are shown in Figure VI. 10, while the adsorption energies for each model are reported in Table VI. 4.

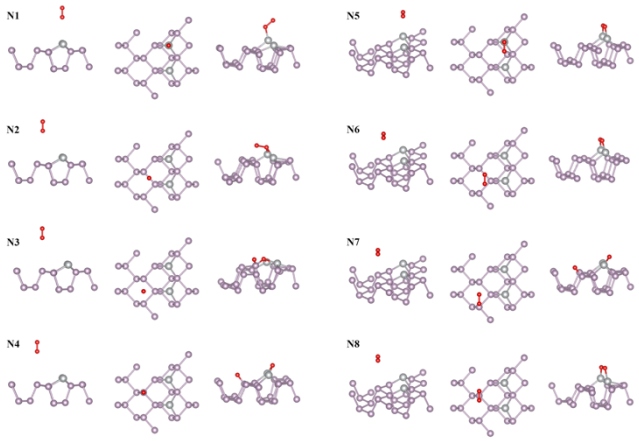

Figure VI. 10: Models used to simulate the adsorption of oxygen molecules on the nickel loaded phosphorene.

Table VI. 4: Calculated adsorption energies of models reported in Figure VI. 10

Model	N1	N2	N3	N4	N5	N6	N7	N8
E_{ads}	0.43	0.73	3.26	3.34	1.46	1.46	3.34	1.42

6.2.4.2. Adsorption of NO_2 gas molecules

To study the second stage of the sensing mechanism of Ni/bP towards NO_2 gas, two possibilities were investigated. First, the adsorption of NO_2 molecules on the layer containing the pre-adsorbed oxygen (model N7) was studied. Then, adsorption on the layer without pre-adsorbed oxygen was investigated. The second case was considered since it was proposed that the NO_2 molecule may react with the free nickels on the surface rather than the pre-adsorbed oxygens. Then, twelve models for each case were considered (M1-M12 and S1-S12 for the first and the second case, respectively). In M1, M2, M3 and M4 an adsorption of the NO_2 molecule in the Ni, B2, H and T sites with one oxygen atom coordinated to the considered adsorption site. Then, two other orientations of the NO_2 molecule were proposed, i.e. M5-M8

and M9-M12 adsorption in the same sites with N and oxygen atoms constituting the NO_2 molecule are facing the layer, respectively. The same reasoning was adopted for the second case with only removing the preadsorbed oxygens. The NO_2 molecule was placed in all cases at a distance about 2.6 Å from the layer. Figure VI. 11 displays the systems considered for the first case before and after relaxation and the corresponding adsorption energies are summarized in Table VI. 5. All calculated adsorption energies were positive that means the NO_2 molecule can be adsorbed on Ni/bP layer with the pre-adsorbed oxygen from the atmosphere. Analyzing the calculated adsorption energies, one can easily conclude that the NO_2 molecule prefers the M5, M7, M10 and M11 modes for its adsorption with 2.27, 1.77, 1.55 and 1.51 eV as adsorption energy for each model, respectively. From Figure VI. 11, it can be also seen that using M5, M7, M10 and M11, an interaction is created between the NO_2 molecule and the layer. For the rest of the models, the NO_2 can be physisorbed on the layer without making any bonds and the adsorption energies in these cases were quite low, ranging from 0.25 to 0.48 eV. Another point to stress from Figure VI. 11 is how the NO_2 molecule makes its bonds on the layer in the four most probable models, wherever the NO_2 molecule was placed on the layer it always create its bonds with the nickel atom. Here, the need to study the adsorption of NO_2 on the layer without the pre-adsorbed oxygens. As mentioned before, S1-S12 reported in Figure VI. 12 were adopted for this purpose. The calculated adsorption energies are summarized in Table VI. 6. It is clear that in this case the calculated adsorption energies are much higher than in M models, and for the most probable case (i.e. S9 model) the calculated value is about 3 eV, which makes the process extremely exothermic and the system more stable. Here, one can confirm the hypothesis of the interaction of NO_2 with the free nickel at the surface of the material rather than with the pre-adsorbed oxygen.

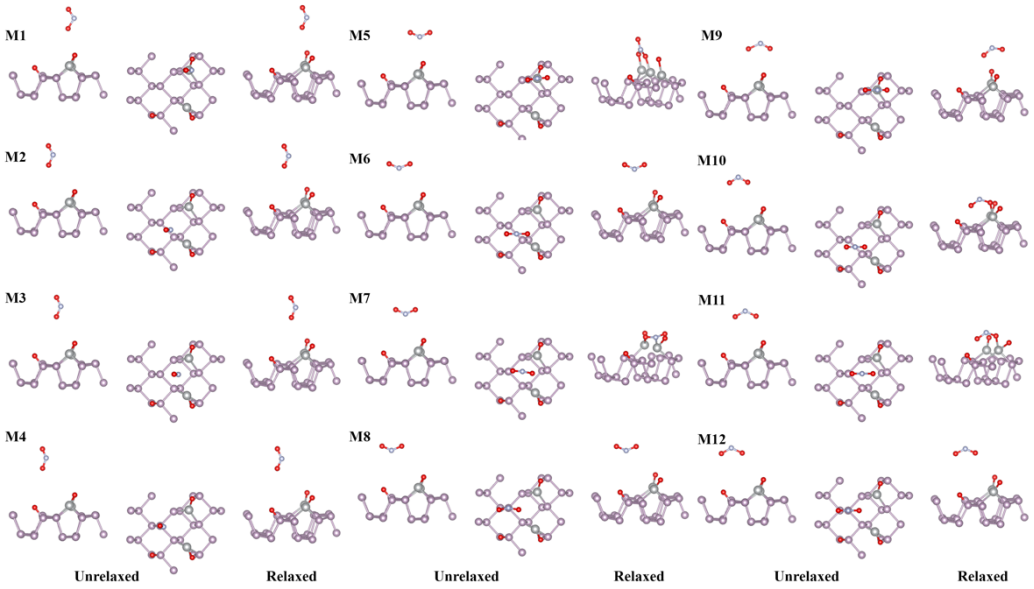

Figure VI. 11: Models used to simulate the adsorption of NO_2 molecule on the nickel loaded phosphorene with pre-adsorbed oxygen.

Table VI. 5: Calculated adsorption energies of models reported in Figure VI. 11

Model	M1	M2	M3	M4	M5	M6	M7	M8	M9	M10	M11	M12
E_{ads}	0.26	0.28	0.28	0.27	2.28	0.27	1.77	0.26	0.49	1.56	1.517	0.277

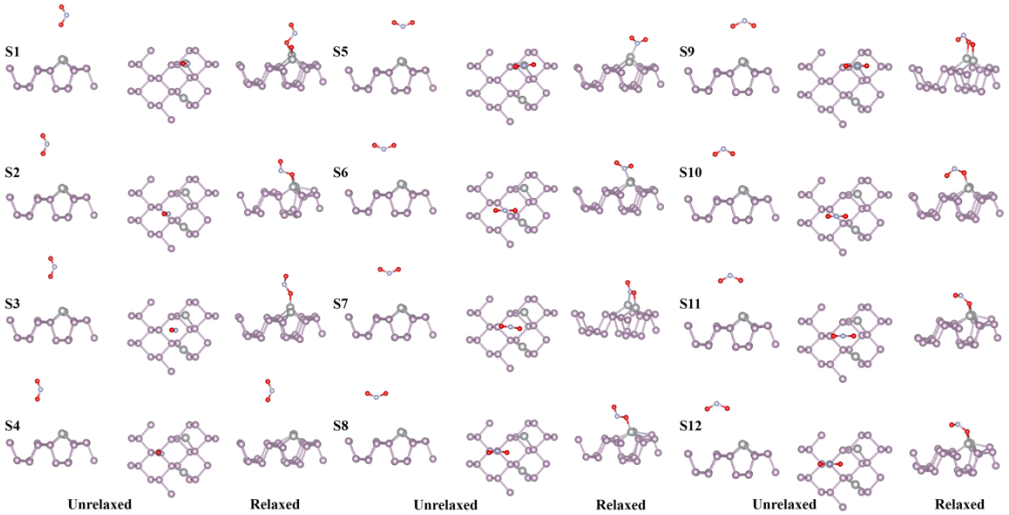

Figure VI. 12: Models used to simulate the adsorption of NO_2 molecule on the nickel loaded phosphorene without pre-adsorbed oxygen.

Table VI. 6: Calculated adsorption energies of models reported in Figure VI. 13

Model	S1	S2	S3	S4	S5	S6	S7	S8	S9	S10	S11	S12
E_{ads}	1.94	2.03	1.73	0.37	2.07	2.04	2.84	1.89	2.86	1.99	2.25	2.23

❖ Charge transfer analysis

As mentioned before, based on an experimental investigation, our group proposed that the sensing mechanism of Ni decorated phosphorene is mainly divided into two main steps. Firstly, oxygen molecules from the surrounding atmosphere can be chemisorbed on the Ni surface. At room temperature (RT), the chemisorbed O_2 molecules can react with electrons at the surface and turn into activated oxygen ions (O^-), lowering the electron density and forming a depletion layer. When NO_2 is fluxed, being a heavy oxidizing gas with a higher electron affinity than activated oxygen, it pulls electrons from the surface and chemisorbs as well. It is believed that Ni nanoparticles on the surface of phosphorene serve as a reaction center for the detection of NO_2 molecules. Ni nanoparticles, in this case, act as receptors for NO_2 molecules, while the phosphorene layer act as transducer converting this interaction into an electrical conductance variation. The reactions involved in both stages are the following:

$$O_{2\,(ads)} + 2e^- \rightarrow 2O^-_{(ads)}$$

$$NO_{2\,(gas)} + e^- \rightarrow NO^-_{2\,(ads)}$$

In this paragraph, Lowdin charge analyses are used to study the charge transfer occurring at the surface of the sensing film. Projecting the density of states on the atomic

orbitals (more precisely, on angular momentum channels which are present in the corresponding pseudopotentials), the Lowdin charges can be calculated only on the valence charge density. Hence, by using the Lowdin charges one can obtain differences between the charge values of atoms composing the system, which generally correspond to the correct trends of charge transfer. In other words, relative trends are usually physically sensitive for most methods and systems including the Lowdin one, that can only qualitatively estimate what is happening to the interacting molecules, and the trend is generally in agreement with experiments. In the presented case, when oxygen molecule is adsorbed on the surface layer (Model N7), it withdraws electrons from the nickel atom gaining 1.64 |e|, meanwhile the nickel atoms and the phosphorus layer loose 0.66 |e| and 1.0749 |e|, respectively. The quantity of electrons lost from the surface was transferred to the adsorbed oxygen molecule, confirming that the proposed reaction for the first stage of the sensing mechanism of nickel loaded phosphorene can happen. Indeed, before the interaction with the molecule the total charge of phosphorus and nickel atoms constituting the layer were 79.1 |e| and 19.4 |e|, respectively. While after the interaction the total charge of phosphorus and Ni atoms were 78.02 |e| and 18.74 |e|, respectively. The electrons participating in these reactions are accumulated on the surface and their density is decreased in the layer, resulting in the creation of a depletion zone. By studying the charge transfer occurring during the interaction reported in the model S9, the proposed reaction for the second stage can be confirmed. In fact, during the interaction, the NO_2 molecule gains 0.57 |e|, which is coming from the Ni atoms since the latter is losing 0.38 |e|. Meanwhile, the phosphorus atoms composing the layer lost 0.16 |e|.

6.3. Conclusions

DFT calculations were carried out to understand how nickel influences the electronic properties of phosphorene since the decoration with nickel showed experimentally better stability of the sensor and high response towards NO_2 at room temperature. The theoretical results explained this behavior by studying the adsorption of oxygen molecules on pristine and nickel loaded phosphorene. The DFT calculations highlight that oxygen molecules dissociate on the layer of pristine phosphorene and react with phosphorus atoms (oxidation of the material) while, in the case of decorated phosphorene, nickel atoms play the role of acceptors and interact with the oxygen molecules. Finally, the sensing mechanism towards NO_2 was investigated theoretically by studying the charge transfer occurring at the surface of the material during the adsorption process. For the first stage of the sensing mechanism, the layer loses charges that are captured by the oxygen from the surrounding atmosphere. In the second step, when the NO_2 molecule is introduced, it takes charges from the adsorbed oxygen molecule.

Summary & Conclusions

This PhD work, which is a combined theoretical DFT and experimental investigations, has been carried out at the University of Ferrara (UNIFE) in the Department of Physics and Earth Sciences in the Sensors and Semiconductors Laboratory (SSL) in collaboration with Micro-Nano Facilities group of the Bruno Kessler Foundation (FBK). It was focused on:

- the synthesis, material and electrical characterizations combined with theoretical ab-initio calculations within the framework of DFT of reduced SnO_2,
- theoretical DFT investigation concerning an innovative 2D material, i.e. nickel decorated phosphorene, and its sensing mechanism Vs. NO_2.

Concerning the experimental part, a simple and low-cost sol-gel method was used to synthesize SnO_2 samples.The obtained powder was calcined in air to obtain stoichiometric SnO_2, then the later was undergone several treatment in H_2 at different temperature to create oxygen vacancies and to stabilize them a vacuum treatment was used. The obtained samples were characterized using XPS, XRD, UV visible and SEM techniques. The results showed a broadening of the VB and a narrowing of the band gap region, this may conduct to an enhancement of the reactions occurring on the surface reactivity of the sensing element, i.e., the narrowing of the band gap make it easy for electrons to jump from the donor level to the CB and then participate in the reactions at the surface of the sensing layer. This enhancement of the surface reactivity of the active element may result in an improvement of the sensitivity of the gas sensor (charge transfer) and it may reduce the temperature that the sensor needs to be thermo-activated, which results in a decrease of the device power consumption. Indeed, the gas sensor electrical characterization showed a high response of the sensors towards low concentrations of NO_2 (500 ppb) at 130 °C instead of 450 °C, which is the best working temperature for the stoichiometric SnO_2.

The DFT theoretical investigations were carried out on both SnO_2 and nickel-decorated phosphorene, to study the influence of oxygen vacancies on the MOX used as a sensing layer for chemoresistive gas sensors, and to investigate the impact of nickel on the physical chemical properties of phosphorene. Two different approaches were used, i.e. the Full Potential Linearized Augmented Plane Wave (FP-LAPW) and the Pseudopotential Plane Waves approach, which is based on atomic pseudopotentials and a basis set of plane waves as implemented in the Wien2k and Quantum Espresso codes, respectively. Different approximations were used for each kind of calculation. Generalized Gradient Approximations (GGA) parameterized PBE (Perdew-Burke-Ernzerhof) was used for the relaxation of the structures, GGA_PBE for solids (GGA-PBEsol) was used for the optimization of structural properties, and modified Becke-Johnson exchange potential model of Tran-Blaha (TB-mBJ) was applied for electronic band gap calculations. Concerning nickel-decorated phosphorene,

the van der Waals DFT (vdW-DF) with the optB88 (optB88-vdW) for the exchange functional was used for the optimization of the structure to treat the van der Waals interactions.

As far as SnO_2 is concerned, the bulk study results showed that increasing the concentration of oxygen vacancies inside SnO_2 causes impurity states to approach the CB, increasing the probability that electrons promote the transition process from the donor level to the CB. This results in an increase of the semiconductor electrical conductivity , and, more importantly for sensing properties, it increases the availability of electrons to participate in reactions at the active material surface, with a positive impact on SnO_2 catalytic performance. The overall effect is a decrease in the temperature required for thermal activation, which is followed by a lower working temperature, and then less energy consumption of the device. Similar results were found investigating the SnO_2 (110) surface, where the possible adsorption modes for oxygen molecules on both clean and defected SnO_2 (110) surface were studied. The results of this part of the work showed that rather than the stoichiometric surface, oxygen molecules can be adsorbed on the SnO_2 (110) surface with oxygen vacancies. Then the possible modes for the creation of surface oxygen vacancies were studied, from which it is found out that the bridging oxygen atoms are the easiest to be created, and that by removing oxygens from subsurface positions, the Fermi energy moves closer to the bottom of the CB. This means that the subsurface oxygen vacancies are effectively functional for sensing applications. However, since the scope of this investigation is to enhance the sensing performance of the device by using a simple and low-cost method for the sensing material preparation, we can conclude that the bridging oxygen vacancies are the most suitable for such technological application. Indeed, the energy required to create them is the lowest among the structural models investigated here, and the Fermi energy is closest to the CB with respect to the stoichiometric surface and the model containing the in-plane oxygen vacancies. Finally, by utilizing oxygen vacancies, one of the main limiting factors of MOX gas sensors can be mitigated: the high working temperature and the resulting high energy consumption.

Concerning nickel-decorated phosphorene, the influence of nickel on the physical-chemical properties of phosphorene was studied by means of DFT. The results showed that, by introducing the Ni atoms, the material band gap value decreased due to the new energy level created in the band gap region just below the Fermi level. This new energy level is corresponding to the shallow acceptor level since it is located between the top of the VB and the Fermi level. This decrease in the band gap may enhance the sensitivity and the response time of sensors produced. In addition, a proposed explanation of the stability of the material was given, i.e. decreasing the band gap and the work function of the material may lead to a drop of the CBM bellow the redox potential of O_2/O_2^-, making it difficult for the material to produce excitons under ambient light. The overall conclusion is the stability and non-degradation of the material. Furthermore, the sensing mechanism of Ni-decorated phosphorene was studied theoretically.

This page intentionally left blank

Appendix A: Simulation of gas molecules

The simulations of oxygen and nitrogen dioxide molecules were performed with the Quantum espresso code, employing the GGA functional approximation. Spin polarized calculations were carried out for both molecules. A cube of 20 Å was used for this purpose to isolate the molecules, i.e., make the code break the periodicity of the system. The relaxed atomic structures (Figure Ap. 1) are obtained using BFGS method and when the atomic forces are lower than 1mRy, the van der Waals DFT (vdW-DF) with the optB88 (optB88-vdW) was used during relaxation of the systems. The cut-off energies for the wave functions and charge density used for oxygen were set to 54 and 486 Ry, respectively while for nitrogen dioxide they were set to 59 and 531 Ry, respectively. Bond lengths and angles of both oxygen and nitrogen dioxide were calculated after the relaxation of the molecules to be compared with those identified in literature and to prove the models used for the simulations. The obtained results are reported in Figure Ap. 1. The calculated bond lengths and angle (for NO_2) are in good agreement with literature.

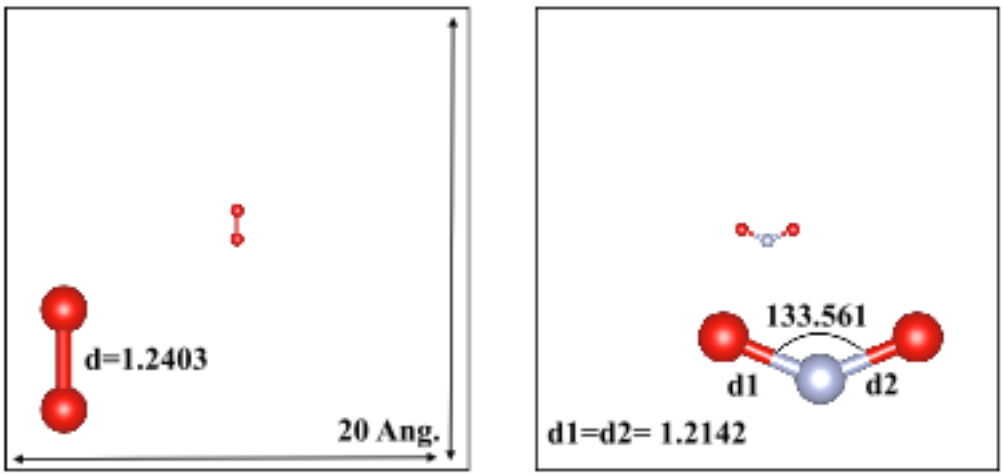

Figure Ap. 1: Relaxed systems for oxygen and nitrogen dioxide molecules. The bond lengths and angles are reported in figure.

This page intentionally left blank

References

[1] I. Kortidis, K. Moschovis, F. A. Mahmoud and G. Kiriakidis, "Structural analysis of aerosol spray pyrolysis ZnO films exhibiting ultra low ozone detection limits at room temperature," *Thin Solid Films,* vol. 518, p. 1208–1213, 2009.

[2] B. Fabbri, S. Gherardi, A. Giberti, V. Guidi and C. Malagù, "Sensing of gaseous malodors characteristic of landfills and waste treatment plants," *Journal of Sensors and Sensor Systems,* vol. 3, p. 61–67, 2014.

[3] B. Fabbri, M. Valt, C. Parretta, S. Gherardi, A. Gaiardo, C. Malagù, F. Mantovani, V. Strati and V. Guidi, "Correlation of gaseous emissions to water stress in tomato and maize crops: From field to laboratory and back," *Sensors and Actuators B: Chemical,* vol. 303, p. 127227, 2020.

[4] A. Gaiardo, G. Zonta, S. Gherardi, C. Malagù, B. Fabbri, M. Valt, L. Vanzetti, N. Landini, D. Casotti, G. Cruciani and others, "Nanostructured SmFeO3 Gas Sensors: Investigation of the Gas Sensing Performance Reproducibility for Colorectal Cancer Screening," *Sensors,* vol. 20, p. 5910, 2020.

[5] N. Landini, G. Anania, B. Fabbri, A. Gaiardo, S. Gherardi, V. Guidi, G. Rispoli, L. Scagliarini, G. Zonta and C. Malagù, "Neoplasms and metastasis detection in human blood exhalations with a device composed by nanostructured sensors," *Sensors and Actuators B: Chemical,* vol. 271, p. 203–214, 2018.

[6] V. Guidi, M. C. Carotta, B. Fabbri, S. Gherardi, A. Giberti and C. Malagù, "Array of sensors for detection of gaseous malodors in organic decomposition products," *Sensors and Actuators B: Chemical,* vol. 174, p. 349–354, 2012.

[7] A. Giberti, M. C. Carotta, B. Fabbri, S. Gherardi, V. Guidi and C. Malagù, "High-sensitivity detection of acetaldehyde," *Sensors and Actuators B: Chemical,* vol. 174, p. 402–405, 2012.

[8] M. C. Carotta, G. Martinelli, L. Crema, C. Malagù, M. Merli, G. Ghiotti and E. Traversa, "Nanostructured thick-film gas sensors for atmospheric pollutant monitoring: quantitative analysis on field tests," *Sensors and Actuators B: Chemical,* vol. 76, p. 336–342, 2001.

[9] M. C. Carotta, A. Cervi, A. Giberti, V. Guidi, C. Malagù, G. Martinelli and D. Puzzovio, "Ethanol interference in light alkane sensing by metal-oxide solid solutions," *Sensors and Actuators B: Chemical,* vol. 136, p. 405–409, 2009.

[10] C. Malagù, B. Fabbri, S. Gherardi, A. Giberti, V. Guidi, N. Landini and G. Zonta, "Chemoresistive gas sensors for the detection of colorectal cancer biomarkers," *Sensors,* vol. 14, p. 18982–18992, 2014.

[11] [Online]. Available: https://www.co2meter.com/.

[12] V. Guidi, C. Malagù, M. C. Carotta and B. Vendemiati, "Printed semiconducting gas sensors," in *Printed Films*, Elsevier, 2012, p. 278–334.

[13] M. Valt, M. Caporali, B. Fabbri, A. Gaiardo, C. Malagù, M. Serrano-Ruiz, M. Peruzzini and V. Guidi, "Nickel-Decorated Black Phosphorus for Room Temperature NO2 detection," in *ECS Meeting Abstracts*, 2020.

[14] G. Korotcenkov, "Metal oxides for solid-state gas sensors: What determines our choice?," *Materials Science and Engineering: B,* vol. 139, pp. 1-23, 2007.

[15] T. Seiyama, A. Kato, K. Fujiishi and M. Nagatani, "A New Detector for Gaseous Components Using Semiconductive Thin Films.," *Analytical Chemistry,* vol. 34, pp. 1502-1503, 1962.

[16] N. Taguchi, "A metal oxide gas sensor," *Japanese patent,* vol. 4538200, 1962.

[17] T. Kind and O. Fiehn, "Advances in structure elucidation of small molecules using mass spectrometry," *Bioanalytical reviews,* vol. 2, p. 23–60, 2010.

[18] F. Dincer, M. Odabasi and A. Muezzinoglu, "Chemical characterization of odorous gases at a landfill site by gas chromatography–mass spectrometry," *Journal of chromatography A,* vol. 1122, p. 222–229, 2006.

[19] J. de Gouw and C. Warneke, "Measurements of volatile organic compounds in the earth's atmosphere using proton-transfer-reaction mass spectrometry," *Mass spectrometry reviews,* vol. 26, p. 223–257, 2007.

[20] N. Yamazoe and K. Shimanoe, "Receptor function and response of semiconductor gas sensor," *Journal of Sensors,* vol. 2009, 2009.

[21] J. Polleux, A. Gurlo, N. Barsan, U. Weimar, M. Antonietti and M. Niederberger, "Template-free synthesis and assembly of single-crystalline tungsten oxide nanowires and their gas-sensing properties," *Angewandte Chemie - International Edition,* vol. 45, pp. 261-265, 2005.

[22] F. Ménil, "Modélisation des temps de réponse des capteurs chimiques," *Comptes Rendus de l'Académie des Sciences - Series IIC - Chemistry,* vol. 4, pp. 899-904, 2001.

[23] M. J. Madou and S. R. Morrison, Chemical sensing with solid state devices, Elsevier, 2012.

[24] B. Fabbri, A. Gaiardo, A. Giberti, V. Guidi, C. Malagù, A. Martucci, M. Sturaro, G. Zonta, S. Gherardi and P. Bernardoni, "Chemoresistive properties of photo-activated thin and thick ZnO films," *Sensors and Actuators B: Chemical,* vol. 222, p. 1251–1256, 2016.

[25] N. Barsan, D. Koziej and U. Weimar, "Metal oxide-based gas sensor research: How to?," *Sensors and Actuators B: Chemical,* vol. 121, p. 18–35, 2007.

[26] N. Yamazoe, G. Sakai and K. Shimanoe, "Oxide semiconductor gas sensors," *Catalysis Surveys from Asia,* vol. 7, p. 63–75, 2003.

[27] V. Guidi, C. Malagù, M. C. Carotta and B. Vendemiati, "Printed semiconducting gas sensors," in *Printed Films*, Elsevier, 2012, p. 278–334.

[28] A. Gaiardo, B. Fabbri, A. Giberti, V. Guidi, P. Bellutti, C. Malagù, M. Valt, G. Pepponi, S. Gherardi, G. Zonta and others, "ZnO and Au/ZnO thin films: Room-temperature chemoresistive properties for gas sensing applications," *Sensors and Actuators B: Chemical,* vol. 237, p. 1085–1094, 2016.

[29] E. Comini, G. Faglia, G. Sberveglieri, Z. Pan and Z. L. Wang, "Stable and highly sensitive gas sensors based on semiconducting oxide nanobelts," *Applied Physics Letters,* vol. 81, pp. 1869-1871, 2002.

[30] A. Kolmakov, Y. Zhang, G. Cheng and M. Moskovits, "Detection of CO and O2 using tin oxide nanowire sensors," *Advanced materials,* vol. 15, p. 997–1000, 2003.

[31] C. Li, D. Zhang, X. Liu, S. Han, T. Tang, J. Han and C. Zhou, "In 2 O 3 nanowires as chemical sensors," *Applied Physics Letters,* vol. 82, p. 1613–1615, 2003.

[32] T. Gao and T. H. Wang, "Synthesis and properties of multipod-shaped ZnO nanorods for gas-sensor applications," *Applied Physics A: Materials Science and Processing,* vol. 80, pp. 1451-1454, 2005.

[33] Z. Bai, C. Xie, S. Zhang, L. Zhang, Q. Zhang, W. Xu and J. Xu, "Microstructure and gas sensing properties of the ZnO thick film treated by hydrothermal method," *Sensors and Actuators, B: Chemical,* vol. 151, pp. 107-113, 2010.

[34] M. C. Carotta, S. Gherardi, V. Guidi, C. Malagu, G. Martinelli, B. Vendemiati, M. Sacerdoti, G. Ghiotti, S. Morandi, A. Bismuto and others, "(Ti, Sn) O2 binary solid solutions for gas sensing: spectroscopic, optical and transport properties," *Sensors and Actuators B: Chemical,* vol. 130, p. 38–45, 2008.

[35] X. He, J. Li, X. Gao and L. Wang, "NO2 sensing characteristics of WO3 thin film microgas sensor," *Sensors and Actuators B: Chemical,* vol. 93, p. 463–467, 2003.

[36] V. Srivastava and K. Jain, "Highly sensitive NH3 sensor using Pt catalyzed silica coating over WO3 thick films," *Sensors and Actuators, B: Chemical,* vol. 133, pp. 46-52, 2008.

References

[37] H. Dong, Z. Li, Z. Ding, H. Pan, X. Wang and X. Fu, "Nanoplates of α-SnWO4 and SnW3O9 prepared via a facile hydrothermal method and their gas-sensing property," *Sensors and Actuators, B: Chemical,* vol. 140, pp. 623-628, 2009.

[38] K. Mukherjee and S. B. Majumder, "Synthesis of embedded and isolated Mg0. 5Zn0. 5Fe2O4 nano-tubes and investigation on their anomalous gas sensing characteristics," *Sensors and Actuators B: Chemical,* vol. 177, p. 55–63, 2013.

[39] A. Oprea, D. Degler, N. Barsan, A. Hemeryck and J. Rebholz, "3 - Basics of semiconducting metal oxide–based gas sensors," in *Gas Sensors Based on Conducting Metal Oxides*, N. Barsan and K. Schierbaum, Eds., Elsevier, 2019, pp. 61-165.

[40] N. Barsan and U. Weimar, "Understanding the fundamental principles of metal oxide based gas sensors; the example of CO sensing with SnO2 sensors in the presence of humidity," *Journal of Physics: Condensed Matter,* vol. 15, p. R813, 2003.

[41] D. Puzzovio, "Surface interaction mechanisms in metal-oxide semiconductors for alkane detection," 2009.

[42] C. Ge, C. Xie and S. Cai, "Preparation and gas-sensing properties of Ce-doped ZnO thin-film sensors by dip-coating," *Materials Science and Engineering: B,* vol. 137, p. 53–58, 2007.

[43] Z.-P. Sun, L. Liu, L. Zhang and D.-Z. Jia, "Rapid synthesis of ZnO nano-rods by one-step, room-temperature, solid-state reaction and their gas-sensing properties," *Nanotechnology,* vol. 17, pp. 2266-2270, 2006.

[44] T.-J. Hsueh, Y.-W. Chen, S.-J. Chang, S.-F. Wang, C.-L. Hsu, Y.-R. Lin, T.-S. Lin and I.-C. Chen, "ZnO nanowire-based CO sensors prepared on patterned ZnO:Ga/SiO2/Si templates," *Sensors and Actuators, B: Chemical,* vol. 125, pp. 498-503, 2007.

[45] N. le Hung, E. Ahn, H. Jung, H. Kim and D. Kim, "Synthesis and gas sensing properties of ZnO nanostructures," *Journal of the Korean Physical Society,* vol. 57, pp. 1784-1788, 2010.

[46] S. Santra, P. K. Guha, S. Z. Ali, P. Hiralal, H. E. Unalan, J. A. Covington, G. A. J. Amaratunga, W. I. Milne, J. W. Gardner and F. Udrea, "ZnO nanowires grown on SOI CMOS substrate for ethanol sensing," *Sensors and Actuators, B: Chemical,* vol. 146, pp. 559-565, 2010.

[47] B. Shouli, C. Liangyuan, L. Dianqing, Y. Wensheng, Y. Pengcheng, L. Zhiyong, C. Aifan and C. C. Liu, "Different morphologies of ZnO nanorods and their sensing property," *Sensors and Actuators, B: Chemical,* vol. 146, pp. 129-137, 2010.

[48] J. F. McAleer, P. T. Moseley, J. O. W. Norris and D. E. Williams, "Tin dioxide gas sensors. Part 1. - Aspects of the surface chemistry revealed by electrical conductance variations," *Journal of the Chemical Society, Faraday Transactions 1: Physical Chemistry in Condensed Phases,* vol. 83, pp. 1323-1346, 1987.

[49] Q. Kuang, C. Lao, Z. L. Wang, Z. Xie and L. Zheng, "High-sensitivity humidity sensor based on a single SnO2 nanowire," *Journal of the American Chemical Society,* vol. 129, p. 6070–6071, 2007.

[50] K. Watanabe, T. Ohgaki, N. Saito, S. Hishita, I. Sakaguchi, H. Haneda and N. Ohashi, "P2. 0.9 Interaction of Water Vapor with SnO2," *Proceedings IMCS 2012,* p. 1285–1288, 2012.

[51] Y. Zeng, T. Zhang, M. Yuan, M. Kang, G. Lu, R. Wang, H. Fan, Y. He and H. Yang, "Growth and selective acetone detection based on ZnO nanorod arrays," *Sensors and Actuators B: Chemical,* vol. 143, p. 93–98, 2009.

[52] C. Li, D. Zhang, X. Liu, S. Han, T. Tang, J. Han and C. Zhou, "In2O3 nanowires as chemical sensors," *Applied Physics Letters,* vol. 82, pp. 1613-1615, 2003.

[53] B. Geng, J. Liu and C. Wang, "Multi-layer ZnO architectures: Polymer induced synthesis and their application as gas sensors," *Sensors and Actuators B: Chemical,* vol. 150, p. 742–748, 2010.

[54] Y. Chen, C. L. Zhu and G. Xiao, "Reduced-temperature ethanol sensing characteristics of flower-like ZnO nanorods synthesized by a sonochemical method," *Nanotechnology,* vol. 17, p. 4537, 2006.

[55] N. Yamazoe, "New approaches for improving semiconductor gas sensors," *Sensors and actuators B: Chemical,* vol. 5, p. 7–19, 1991.

[56] N. Van Duy, N. Van Hieu, P. T. Huy, N. D. Chien, M. Thamilselvan and J. Yi, "Mixed SnO2/TiO2 included with carbon nanotubes for gas-sensing application," *Physica E: Low-dimensional Systems and Nanostructures,* vol. 41, p. 258–263, 2008.

[57] Z. Essalhi, S. Krik, B. Hartiti, A. Gaiardo, A. Lfakir, M. Valt, S. Fadili, B. Fabbri, M. Siadat and V. Guidi, "Elaboration and Characterization of SnO2 Doped TiO2 Gas Sensors Deposited through Dip and Spin Coating Methods," *Multidisciplinary Digital Publishing Institute Proceedings,* vol. 14, p. 23, 2019.

[58] S. Wei, Y. Zhang and M. Zhou, "Toluene sensing properties of SnO2–ZnO hollow nanofibers fabricated from single capillary electrospinning," *Solid state communications,* vol. 151, p. 895–899, 2011.

[59] M. S. Wagh, G. H. Jain, D. R. Patil, S. A. Patil and L. A. Patil, "Modified zinc oxide thick film resistors as NH3 gas sensor," *Sensors and Actuators B: Chemical,* vol. 115, p. 128–133, 2006.

[60] X. Jia, H. Fan, M. Afzaal, X. Wu and P. O'Brien, "Solid state synthesis of tin-doped ZnO at room temperature: characterization and its enhanced gas sensing and photocatalytic properties," *Journal of hazardous materials,* vol. 193, p. 194–199, 2011.

[61] X. Wang, J. Zhang, Z. Zhu and J. Zhu, "Effect of Pd2+ doping on ZnO nanotetrapods ammonia sensor," *Colloids and Surfaces A: Physicochemical and Engineering Aspects,* vol. 276, p. 59–64, 2006.

[62] X.-Y. Xue, Z.-H. Chen, L.-L. Xing, C.-H. Ma, Y.-J. Chen and T.-H. Wang, "Enhanced optical and sensing properties of one-step synthesized Pt- ZnO nanoflowers," *The Journal of Physical Chemistry C,* vol. 114, p. 18607–18611, 2010.

[63] K. Zheng, L. Gu, D. Sun, X. Mo and G. Chen, "The properties of ethanol gas sensor based on Ti doped ZnO nanotetrapods," *Materials Science and Engineering: B,* vol. 166, p. 104–107, 2010.

[64] H. Ahn, Y. Wang, S. H. Jee, M. Park, Y. S. Yoon and D.-J. Kim, "Enhanced UV activation of electrochemically doped Ni in ZnO nanorods for room temperature acetone sensing," *Chemical Physics Letters,* vol. 511, p. 331–335, 2011.

[65] C. S. Prajapati and P. P. Sahay, "Influence of In doping on the structural, optical and acetone sensing properties of ZnO nanoparticulate thin films," *Materials science in semiconductor processing,* vol. 16, p. 200–210, 2013.

[66] S.-J. Chang, T.-J. Hsueh, I.-C. Chen, S.-F. Hsieh, S.-P. Chang, C.-L. Hsu, Y.-R. Lin and B.-R. Huang, "Highly sensitive ZnO nanowire acetone vapor sensor with Au adsorption," *IEEE transactions on nanotechnology,* vol. 7, p. 754–759, 2008.

[67] Y.-J. Li, K.-M. Li, C.-Y. Wang, C.-I. Kuo and L.-J. Chen, "Low-temperature electrodeposited Co-doped ZnO nanorods with enhanced ethanol and CO sensing properties," *Sensors and Actuators B: Chemical,* vol. 161, p. 734–739, 2012.

[68] J. F. Chang, H. H. Kuo, I. C. Leu and M. H. Hon, "The effects of thickness and operation temperature on ZnO: Al thin film CO gas sensor," *Sensors and actuators B: Chemical,* vol. 84, p. 258–264, 2002.

[69] P. P. Sahay and R. K. Nath, "Al-doped zinc oxide thin films for liquid petroleum gas (LPG) sensors," *Sensors and Actuators B: Chemical,* vol. 133, p. 222–227, 2008.

[70] H. Y. Bae and G. M. Choi, "Electrical and reducing gas sensing properties of ZnO and ZnO–CuO thin films fabricated by spin coating method," *Sensors and Actuators B: Chemical,* vol. 55, p. 47–54, 1999.

[71] M. Zhao, X. Wang, L. Ning, J. Jia, X. Li and L. Cao, "Electrospun Cu-doped ZnO nanofibers for H2S sensing," *Sensors and Actuators B: Chemical,* vol. 156, p. 588–592, 2011.

References

[72] Y. Zeng, T. Zhang, L. Wang, M. Kang, H. Fan, R. Wang and Y. He, "Enhanced toluene sensing characteristics of TiO2-doped flowerlike ZnO nanostructures," *Sensors and Actuators B: Chemical,* vol. 140, p. 73–78, 2009.

[73] M. C. Carotta, A. Cervi, A. Fioravanti, S. Gherardi, A. Giberti, B. Vendemiati, D. Vincenzi and M. Sacerdoti, "A novel ozone detection at room temperature through UV-LED-assisted ZnO thick film sensors," *Thin Solid Films,* vol. 520, p. 939–946, 2011.

[74] A. L. Linsebigler, G. Lu and J. T. Yates Jr, "Photocatalysis on TiO2 surfaces: principles, mechanisms, and selected results," *Chemical reviews,* vol. 95, p. 735–758, 1995.

[75] J. M. Herrmann, "Environmental photocatalysis: perspectives for China," *Science China Chemistry,* vol. 53, p. 1831–1843, 2010.

[76] A. Mills and S. Le Hunte, "An overview of semiconductor photocatalysis," *Journal of photochemistry and photobiology A: Chemistry,* vol. 108, p. 1–35, 1997.

[77] S. Das and V. Jayaraman, "SnO2: A comprehensive review on structures and gas sensors," *Progress in Materials Science,* vol. 66, p. 112–255, 2014.

[78] R. J. Cernik, "X-ray Powder Diffractometry. An Introduction.(Serie: Chemical Analysis, Vol. 138.) Von R. Jenkins und RL Snyder. John Wiley & Sons, New York, 1996. 391 S., geb. 87.95£.—ISBN 0–471–51339–3," *Angewandte Chemie,* vol. 109, p. 1417–1418, 1997.

[79] I. Jimenez, J. Arbiol, G. Dezanneau, A. Cornet and J. R. Morante, "Crystalline structure, defects and gas sensor response to NO2 and H2S of tungsten trioxide nanopowders," *Sensors and Actuators B: Chemical,* vol. 93, p. 475–485, 2003.

[80] P. Van der Heide, X-ray photoelectron spectroscopy: an introduction to principles and practices, John Wiley & Sons, 2011.

[81] A. Cabot, A. Dieguez, A. Romano-Rodrıguez, J. R. Morante and N. Barsan, "Influence of the catalytic introduction procedure on the nano-SnO2 gas sensor performances: where and how stay the catalytic atoms?," *Sensors and Actuators B: Chemical,* vol. 79, p. 98–106, 2001.

[82] [Online]. Available: https://fmps.fbk.eu/x-ray-photoelectron-spectroscopy-xps.

[83] L. Reimer, *Scanning electron microscopy: physics of image formation and microanalysis,* IOP Publishing, 2000.

[84] D. B. Wiiliams and C. B. Carter, *Transmission Electron Microscopy: A Textbook for Materials Science,* Springer Science+ Business Media, 2009.

[85] M. Born and R. Oppenheimer, "Zur quantentheorie der molekeln," *Annalen der physik,* vol. 389, p. 457–484, 1927.

[86] D. R. Hartree, "The wave mechanics of an atom with a non-Coulomb central field Part 1. Theory and methods," *Сборник статей к мультимедийному электронному учебно-методическому комплексу по дисциплине \guillemotleftфизика атома и атомных явлений\guillemotright/отв. ред. Шундалов МБ; БГУ, Физический факультет,* 1928.

[87] V. Fock, "Näherungsmethode zur Lösung des quantenmechanischen Mehrkörperproblems," *Zeitschrift für Physik,* vol. 61, p. 126–148, 1930.

[88] P. Hohenberg and W. Kohn, "Density functional theory (DFT)," *Phys. Rev,* vol. 136, p. B864, 1964.

[89] P. Hohenberg and W. Kohn, "Inhomogeneous electron gas," *Physical review,* vol. 136, p. B864, 1964.

[90] W. Kohn and L. J. Sham, "Self-consistent equations including exchange and correlation effects," *Physical review,* vol. 140, p. A1133, 1965.

[91] J. P. Perdew and Y. Wang, "Accurate and simple analytic representation of the electron-gas correlation energy," *Physical review B,* vol. 45, p. 13244, 1992.

[92] R. O. Jones and O. Gunnarsson, "The density functional formalism, its applications and prospects," *Reviews of Modern Physics,* vol. 61, p. 689, 1989.

[93] D. C. Langreth and M. J. Mehl, "Beyond the local-density approximation in calculations of ground-state electronic properties," *Physical Review B,* vol. 28, p. 1809, 1983.

[94] J. A. White and D. M. Bird, "Implementation of gradient-corrected exchange-correlation potentials in Car-Parrinello total-energy calculations," *Physical Review B,* vol. 50, p. 4954, 1994.

[95] B. G. Johnson, P. M. W. Gill and J. A. Pople, "The performance of a family of density functional methods," *The Journal of chemical physics,* vol. 98, p. 5612–5626, 1993.

[96] A. García, C. Elsässer, J. Zhu, S. G. Louie and M. L. Cohen, "Use of gradient-corrected functionals in total-energy calculations for solids," *Physical Review B,* vol. 46, p. 9829, 1992.

[97] A. Zupan, P. Blaha, K. Schwarz and J. P. Perdew, "Pressure-induced phase transitions in solid Si, SiO 2, and Fe: Performance of local-spin-density and generalized-gradient-approximation density functionals," *Physical Review B,* vol. 58, p. 11266, 1998.

[98] J. P. Perdew, J. A. Chevary, S. H. Vosko, K. A. Jackson, M. R. Pederson, D. J. Singh and C. Fiolhais, "Atoms, molecules, solids, and surfaces: Applications of the generalized gradient approximation for exchange and correlation," *Phys. Rev. B,* vol. 46, no. 11, p. 6671–6687, 9 1992.

[99] J. P. Perdew, K. Burke and M. Ernzerhof, "Generalized Gradient Approximation Made Simple," *Phys. Rev. Lett.,* vol. 77, no. 18, p. 3865–3868, 10 1996.

[100] A. D. Becke, "Density-functional exchange-energy approximation with correct asymptotic behavior," *Physical review A,* vol. 38, p. 3098, 1988.

[101] J. P. Perdew, K. Burke and Y. Wang, "Generalized gradient approximation for the exchange-correlation hole of a many-electron system," *Physical Review B,* vol. 54, p. 16533, 1996.

[102] C. Adamo and V. Barone, "Exchange functionals with improved long-range behavior and adiabatic connection methods without adjustable parameters: The m PW and m PW1PW models," *The Journal of chemical physics,* vol. 108, p. 664–675, 1998.

[103] J. P. Perdew and W. Yue, "Accurate and simple density functional for the electronic exchange energy: Generalized gradient approximation," *Physical review B,* vol. 33, p. 8800, 1986.

[104] D. M. Ceperley and B. J. Alder, "Ground state of the electron gas by a stochastic method," *Physical Review Letters,* vol. 45, p. 566, 1980.

[105] J. P. Perdew, S. Burke and M. Ernzerhof, "The exchange-correlation potential in the GGA approximation," *Phys. Rev. Lett,* vol. 77, p. 3865–3868, 1996.

[106] m. F. Bloch, "Bemerkung zur Elektronentheorie des Ferromagnetismus und der elektrischen Leitfähigkeit," *Zeitschrift für Physik,* vol. 57, p. 545–555, 1929.

[107] J. C. Slater and J. C. Phillips, "Quantum theory of molecules and solids Vol. 4: the self-consistent field for molecules and solids," *PhT,* vol. 27, p. 49, 1974.

[108] C. Herring, "A new method for calculating wave functions in crystals," *Physical Review,* vol. 57, p. 1169, 1940.

[109] J. C. Slater, "Wave functions in a periodic potential," *Physical Review,* vol. 51, p. 846, 1937.

[110] J. Korringa, "On the calculation of the energy of a Bloch wave in a metal," *Physica,* vol. 13, p. 392–400, 1947.

[111] F. S. Ham and B. Segall, "Energy bands in periodic lattices—Green's function method," *Physical Review,* vol. 124, p. 1786, 1961.

[112] O. K. Andersen, "Linear methods in band theory," *Physical Review B,* vol. 12, p. 3060, 1975.

References

[113] J. C. Slater, "Energy band calculations by the augmented plane wave method," in *Advances in quantum chemistry*, vol. 1, Elsevier, 1964, p. 35–58.

[114] E. Wimmer, H. Krakauer, M. Weinert and A. J. Freeman, "Full-potential self-consistent linearized-augmented-plane-wave method for calculating the electronic structure of molecules and surfaces: O 2 molecule," *Physical Review B,* vol. 24, p. 864, 1981.

[115] D. D. Koelling and G. O. Arbman, "Use of energy derivative of the radial solution in an augmented plane wave method: application to copper," *Journal of Physics F: Metal Physics,* vol. 5, p. 2041, 1975.

[116] T. Takeda and J. Kubler, "Linear augmented plane wave method for self-consistent calculations," *Journal of Physics F: Metal Physics,* vol. 9, p. 661, 1979.

[117] D. Singh and H. Krakauer, "H-point phonon in molybdenum: Superlinearized augmented-plane-wave calculations," *Physical Review B,* vol. 43, p. 1441, 1991.

[118] P. Blaha, K. Schwarz, F. Tran, R. Laskowski, G. K. H. Madsen and L. D. Marks, "WIEN2k: An APW+ lo program for calculating the properties of solids," *The Journal of Chemical Physics,* vol. 152, p. 074101, 2020.

[119] P. Giannozzi, O. Baseggio, P. Bonfà, D. Brunato, R. Car, I. Carnimeo, C. Cavazzoni, S. De Gironcoli, P. Delugas, F. Ferrari Ruffino and others, "Quantum ESPRESSO toward the exascale," *The Journal of chemical physics,* vol. 152, p. 154105, 2020.

[120] G. Kresse and J. Furthmüller, "Efficient iterative schemes for ab initio total-energy calculations using a plane-wave basis set," *Physical review B,* vol. 54, p. 11169, 1996.

[121] G. Kresse and D. Joubert, "From ultrasoft pseudopotentials to the projector augmented-wave method," *Physical review b,* vol. 59, p. 1758, 1999.

[122] "Wien2k," [Online]. Available: http://susi.theochem.tuwien.ac.at/.

[123] E. Artacho, E. Anglada, O. Diéguez, J. D. Gale, A. García, J. Junquera, R. M. Martin, P. Ordejón, J. M. Pruneda, D. Sánchez-Portal and others, "The SIESTA method; developments and applicability," *Journal of Physics: Condensed Matter,* vol. 20, p. 064208, 2008.

[124] S. Krik, A. Gaiardo, M. Valt, B. Fabbri, C. Malagù, G. Pepponi, P. Bellutti and V. Guidi, "First-Principles Study of Electronic Conductivity, Structural and Electronic Properties of Oxygen-Vacancy-Defected SnO2," *Journal of Nanoscience and Nanotechnology,* vol. 21, p. 2633–2640, 2021.

[125] S. O. Kucheyev, T. F. Baumann, P. A. Sterne, Y. M. Wang, T. Van Buuren, A. V. Hamza, L. J. Terminello and T. M. Willey, "Surface electronic states in three-dimensional SnO 2 nanostructures," *Physical Review B,* vol. 72, p. 035404, 2005.

[126] K. Nomura, H. Ohta, A. Takagi, T. Kamiya, M. Hirano and H. Hosono, "Room-temperature fabrication of transparent flexible thin-film transistors using amorphous oxide semiconductors," *nature,* vol. 432, p. 488–492, 2004.

[127] S. Gürakar, T. Serin and N. Serin, "Electrical and microstructural properties of (Cu, Al, In)-doped SnO2 films deposited by spray pyrolysis," *Adv. Mat. Lett,* vol. 5, p. 309–314, 2014.

[128] S. B. Ogale, R. J. Choudhary, J. P. Buban, S. E. Lofland, S. R. Shinde, S. N. Kale, V. N. Kulkarni, J. Higgins, C. Lanci, J. R. Simpson and others, "High Temperature Ferromagnetism with a Giant Magnetic Moment in Transparent Co-doped S n O 2- δ," *Physical Review Letters,* vol. 91, p. 077205, 2003.

[129] C. Wang, L. Yin, L. Zhang, D. Xiang and R. Gao, "Metal oxide gas sensors: sensitivity and influencing factors," *sensors,* vol. 10, p. 2088–2106, 2010.

[130] J. P. Perdew, A. Ruzsinszky, G. I. Csonka, O. A. Vydrov, G. E. Scuseria, L. A. Constantin, X. Zhou and K. Burke, "Restoring the density-gradient expansion for exchange in solids and surfaces," *Physical review letters,* vol. 100, p. 136406, 2008.

[131] P. Dufek, P. Blaha and K. Schwarz, "Applications of Engel and Vosko's generalized gradient approximation in solids," *Physical Review B,* vol. 50, p. 7279, 1994.

[132] J. Heyd, J. E. Peralta, G. E. Scuseria and R. L. Martin, "Energy band gaps and lattice parameters evaluated with the Heyd-Scuseria-Ernzerhof screened hybrid functional," *The Journal of chemical physics,* vol. 123, p. 174101, 2005.

[133] F. Tran and P. Blaha, "Accurate band gaps of semiconductors and insulators with a semilocal exchange-correlation potential," *Physical review letters,* vol. 102, p. 226401, 2009.

[134] D. Koller, F. Tran and P. Blaha, "Merits and limits of the modified Becke-Johnson exchange potential," *Physical Review B,* vol. 83, p. 195134, 2011.

[135] K. Schwarz, "DFT calculations of solids with LAPW and WIEN2k," *Journal of Solid State Chemistry,* vol. 176, p. 319–328, 2003.

[136] D. J. Singh and L. Nordstrom, Planewaves, Pseudopotentials, and the LAPW method, Springer Science & Business Media, 2006.

[137] J. R. Chelikowsky and S. G. Louie, Quantum theory of real materials, vol. 348, Springer Science & Business Media, 1996.

[138] G. K. H. Madsen, J. Carrete and M. J. Verstraete, "BoltzTraP2, a program for interpolating band structures and calculating semi-classical transport coefficients," *Computer Physics Communications,* vol. 231, p. 140–145, 2018.

[139] J. Haines and J. M. Léger, "X-ray diffraction study of the phase transitions and structural evolution of tin dioxide at high pressure: ffRelationships between structure types and implications for other rutile-type dioxides," *Physical Review B,* vol. 55, p. 11144, 1997.

[140] H. J. Monkhorst and J. D. Pack, "Special points for Brillouin-zone integrations," *Physical review B,* vol. 13, p. 5188, 1976.

[141] F. D. Murnaghan, "The compressibility of media under extreme pressures," *Proceedings of the national academy of sciences of the United States of America,* vol. 30, p. 244, 1944.

[142] P. Chetri and A. Choudhury, "Investigation of optical properties of SnO2 nanoparticles," *Physica E: Low-dimensional Systems and Nanostructures,* vol. 47, p. 257–263, 2013.

[143] B. Zhu, C.-M. Liu, M.-B. Lv, X.-R. Chen, J. Zhu and G.-F. Ji, "Structures, phase transition, elastic properties of SnO2 from first-principles analysis," *Physica B: Condensed Matter,* vol. 406, p. 3508–3513, 2011.

[144] A. Zupan and M. Causà, "Density functional lcao calculations for solids: Comparison among Hartree–Fock, dft local density approximation, and dft generalized gradient approximation structural properties," *International Journal of Quantum Chemistry,* vol. 56, p. 337–344, 1995.

[145] M. Calatayud, J. Andrés and A. Beltrán, "A theoretical analysis of adsorption and dissociation of CH3OH on the stoichiometric SnO2 (110) surface," *Surface science,* vol. 430, p. 213–222, 1999.

[146] E. P. y Blancá, A. Svane, N. E. Christensen, C. O. Rodriguez, O. M. Cappannini and M. S. Moreno, "Calculated static and dynamic properties of β-Sn and Sn-O compounds," *Physical Review B,* vol. 48, p. 15712, 1993.

[147] X. Pan, M.-Q. Yang, X. Fu, N. Zhang and Y.-J. Xu, "Defective TiO 2 with oxygen vacancies: synthesis, properties and photocatalytic applications," *Nanoscale,* vol. 5, p. 3601–3614, 2013.

[148] L. S. Roman, R. Valaski, C. D. Canestraro, E. C. S. Magalhaes, C. Persson, R. Ahuja, E. F. da Silva Jr, I. Pepe and A. F. da Silva, "Optical band-edge absorption of oxide compound SnO2," *Applied Surface Science,* vol. 252, p. 5361–5364, 2006.

[149] K. Zakrzewska, "Mixed oxides as gas sensors," *Thin solid films,* vol. 391, p. 229–238, 2001.

[150] Z. Wen and L. Tian-Mo, "Gas-sensing properties of SnO2–TiO2-based sensor for volatile organic compound gas and its sensing mechanism," *Physica B: Condensed Matter,* vol. 405, p. 1345–1348, 2010.

References

[151] M. Al-Hashem, S. Akbar and P. Morris, "Role of oxygen vacancies in nanostructured metal-oxide gas sensors: a review," *Sensors and Actuators B: Chemical,* vol. 301, p. 126845, 2019.

[152] F. Mehmood, R. Pachter, N. R. Murphy, W. E. Johnson and C. V. Ramana, "Effect of oxygen vacancies on the electronic and optical properties of tungsten oxide from first principles calculations," *Journal of Applied Physics,* vol. 120, p. 233105, 2016.

[153] M. A. K. Purbayanto, E. Nurfani, O. Chichvarina, J. Ding, A. Rusydi and Y. Darma, "Oxygen vacancy enhancement promoting strong green emission through surface modification in ZnO thin film," *Applied Surface Science,* vol. 462, p. 466–470, 2018.

[154] Y. Wang, J. Cai, M. Wu, J. Chen, W. Zhao, Y. Tian, T. Ding, J. Zhang, Z. Jiang and X. Li, "Rational construction of oxygen vacancies onto tungsten trioxide to improve visible light photocatalytic water oxidation reaction," *Applied Catalysis B: Environmental,* vol. 239, p. 398–407, 2018.

[155] J. Kaur, K. Anand, A. Kaur and R. C. Singh, "Sensitive and selective acetone sensor based on Gd doped WO3/reduced graphene oxide nanocomposite," *Sensors and Actuators B: Chemical,* vol. 258, p. 1022–1035, 2018.

[156] Y. Ge, Z. Wei, Y. Li, J. Qu, B. Zu and X. Dou, "Highly sensitive and rapid chemiresistive sensor towards trace nitro-explosive vapors based on oxygen vacancy-rich and defective crystallized In-doped ZnO," *Sensors and Actuators B: Chemical,* vol. 244, p. 983–991, 2017.

[157] W. Zhou, Y. Liu, Y. Yang and P. Wu, "Band gap engineering of SnO2 by epitaxial strain: experimental and theoretical investigations," *The Journal of Physical Chemistry C,* vol. 118, p. 6448–6453, 2014.

[158] F. E. H. Hassan, S. Moussawi, W. Noun, C. Salameh and A. V. Postnikov, "Theoretical calculations of the high-pressure phases of SnO2," *Computational materials science,* vol. 72, p. 86–92, 2013.

[159] M. Behtash, P. H. Joo, S. Nazir and K. Yang, "Electronic structures and formation energies of pentavalent-ion-doped SnO2: first-principles hybrid functional calculations," *Journal of Applied Physics,* vol. 117, p. 175101, 2015.

[160] B. A. Hamad, "First-principle calculations of structural and electronic properties of rutile-phase dioxides (MO 2), M= Ti, V, Ru, Ir and Sn," *The European Physical Journal B,* vol. 70, p. 163–169, 2009.

[161] V. M. Zainullina, "Electronic structure, chemical bonding and properties of Sn1-xMxO2, M= As, Sb, Bi, V, Nb, Ta (0.0⩽ x⩽ 0.25)," *Physica B: Condensed Matter,* vol. 391, p. 280–285, 2007.

[162] V. B. Kamble and A. M. Umarji, "Defect induced optical bandgap narrowing in undoped SnO2 nanocrystals," *AIP Advances,* vol. 3, p. 082120, 2013.

[163] A. M. Ganose and D. O. Scanlon, "Band gap and work function tailoring of SnO 2 for improved transparent conducting ability in photovoltaics," *Journal of Materials Chemistry C,* vol. 4, p. 1467–1475, 2016.

[164] J. Wang, Z. Wang, B. Huang, Y. Ma, Y. Liu, X. Qin, X. Zhang and Y. Dai, "Oxygen vacancy induced band-gap narrowing and enhanced visible light photocatalytic activity of ZnO," *ACS applied materials & interfaces,* vol. 4, p. 4024–4030, 2012.

[165] C. Pijolat, "Étude des propriétés physico-chimiques et des propriétés électriques du dioxyde d'étain en fonction de l'atmosphère gazeuse environnante. Application à la détection sélective des gaz.," 1986.

[166] T. Lin, X. Lv, Z. Hu, A. Xu and C. Feng, "Semiconductor metal oxides as chemoresistive sensors for detecting volatile organic compounds," *Sensors,* vol. 19, p. 233, 2019.

[167] T. G. G. Maffeis, G. T. Owen, S. P. Wilks, C. MALAGÙ, G. MARTINELLI, M. K. Kennedy and F. E. Kruis, "ROOM TEMPERATURE AND ELEVATED TEMPERATURE CHARACTERIZATION OF NANOCRYSTALLINE SnO 2

SURFACES BY SCANNING TUNNELING MICROSCOPY AND SPECTROSCOPY," *International Journal of Nanoscience,* vol. 3, p. 519–524, 2004.

[168] N. Bonini, M. C. Carotta, A. Chiorino, V. Guidi, C. Malagù, G. Martinelli, L. Paglialonga and M. Sacerdoti, "Doping of a nanostructured titania thick film: structural and electrical investigations," *Sensors and Actuators B: Chemical,* vol. 68, p. 274–280, 2000.

[169] C. Malagù, V. Guidi, M. C. Carotta and G. Martinelli, "Unpinning of Fermi level in nanocrystalline semiconductors," *Applied Physics Letters,* vol. 84, p. 4158–4160, 2004.

[170] A. Pan and X. Zhu, "Optoelectronic properties of semiconductor nanowires," in *Semiconductor Nanowires*, Elsevier, 2015, p. 327–363.

[171] F. Yakuphanoglu, "Electrical conductivity, Seebeck coefficient and optical properties of SnO2 film deposited on ITO by dip coating," *Journal of Alloys and Compounds,* vol. 470, p. 55–59, 2009.

[172] H. Ji, W. Zeng and Y. Li, "Gas sensing mechanisms of metal oxide semiconductors: a focus review," *Nanoscale,* vol. 11, p. 22664–22684, 2019.

[173] S.-C. Lee, J.-H. Lee, T.-S. Oh and Y.-H. Kim, "Fabrication of tin oxide film by sol–gel method for photovoltaic solar cell system," *Solar energy materials and solar cells,* vol. 75, p. 481–487, 2003.

[174] R. S. Hiratsuka, S. H. Pulcinelli and C. V. Santilli, "Formation of SnO2 gels from dispersed sols in aqueous colloidal solutions," *Journal of non-crystalline solids,* vol. 121, p. 76–83, 1990.

[175] P. G. Harrison and A. Guest, "Tin oxide surfaces. Part 17.—An infrared and thermogravimetric analysis of the thermal dehydration of tin (IV) oxide gel," *Journal of the Chemical Society, Faraday Transactions 1: Physical Chemistry in Condensed Phases,* vol. 83, p. 3383–3397, 1987.

[176] A. Hassanzadeh, B. Moazzez, H. Haghgooie, M. Nasseri, M. M. Golzan and H. Sedghi, "Synthesis of SnO 2 nanopowders by a sol-gel process using propanol-isopropanol mixture," *Central European Journal of Chemistry,* vol. 6, p. 651–656, 2008.

[177] B. Orel, U. Lavrenčič-Štankgar, Z. Crnjak-Orel, P. Bukovec and M. Kosec, "Structural and FTIR spectroscopic studies of gel-xerogel-oxide transitions of SnO2 and SnO2: Sb powders and dip-coated films prepared via inorganic sol-gel route," *Journal of non-crystalline solids,* vol. 167, p. 272–288, 1994.

[178] A. Maddalena, R. Dal Maschio, S. Dire and A. Raccanelli, "Electrical conductivity of tin oxide films prepared by the sol-gel method," *Journal of Non-Crystalline Solids,* vol. 121, p. 365–369, 1990.

[179] J. P. Chatelon, C. Terrier, E. Bernstein, R. Berjoan and J. A. Roger, "Morphology of SnO2 thin films obtaibed by the sol-gel technique," *Thin solid films,* vol. 247, p. 162–168, 1994.

[180] W. Dazhi, W. Shulin, C. Jun, Z. Suyuan and L. Fangqing, "Microstructure of SnO 2," *Physical Review B,* vol. 49, p. 14282, 1994.

[181] D. M. Mattox, "Sol-gel derived, air-baked indium and tin oxide films," *Thin Solid Films,* vol. 204, p. 25–32, 1991.

[182] J. C. Giuntini, W. Granier, J. V. Zanchetta and A. Taha, "Sol-gel preparation and transport properties of a tin oxide," *Journal of materials science letters,* vol. 9, p. 1383–1388, 1990.

[183] C. D. Feng, Y. Shimizu and M. Egashira, "Effect of Gas Diffusion Process on Sensing Properties of SnO2 Thin Film Sensors in a SiO2/SnO2 Layer-Built Structure Fabricated by Sol-Gel Process," *Journal of the Electrochemical Society,* vol. 141, p. 220, 1994.

[184] A. Chiorino, G. Ghiotti, F. Prinetto, M. C. Carotta, D. Gnani and G. Martinelli, "Preparation and characterization of SnO2 and MoOx–SnO2 nanosized powders for thick film gas sensors," *Sensors and Actuators B: Chemical,* vol. 58, p. 338–349, 1999.

References

[185] X. Zheng, F. Ren, S. Zhang, X. Zhang, H. Wu, X. Zhang, Z. Xing, W. Qin, Y. Liu and C. Jiang, "A general method for large-scale fabrication of semiconducting oxides with high SERS sensitivity," *ACS applied materials & interfaces,* vol. 9, p. 14534–14544, 2017.

[186] S. S. Kalanur, I.-H. Yoo, I.-S. Cho and H. Seo, "Effect of oxygen vacancies on the band edge properties of WO3 producing enhanced photocurrents," *Electrochimica Acta,* vol. 296, p. 517–527, 2019.

[187] M. Shao, J. Liu, W. Ding, J. Wang, F. Dong and J. Zhang, "Oxygen vacancy engineering of self-doped SnO 2- x nanocrystals for ultrasensitive NO 2 detection," *Journal of Materials Chemistry C,* vol. 8, p. 487–494, 2020.

[188] M. Kwoka and M. Krzywiecki, "Impact of air exposure and annealing on the chemical and electronic properties of the surface of SnO2 nanolayers deposited by rheotaxial growth and vacuum oxidation," *Beilstein journal of nanotechnology,* vol. 8, p. 514–521, 2017.

[189] P. Cheyssac, N. Laidani and M. Anderle, "Optical absorption in ZrO2–x-C nanocomposite films on polymer substrates: application of an effective medium theory," *physica status solidi c,* vol. 5, p. 3376–3382, 2008.

[190] N. Li, K. Du, G. Liu, Y. Xie, G. Zhou, J. Zhu, F. Li and H.-M. Cheng, "Effects of oxygen vacancies on the electrochemical performance of tin oxide," *Journal of Materials Chemistry A,* vol. 1, p. 1536–1539, 2013.

[191] F. Lawson, "Tin oxide—Sn 3 O 4," *Nature,* vol. 215, p. 955–956, 1967.

[192] P. Giannozzi, O. Baseggio, P. Bonfà, D. Brunato, R. Car, I. Carnimeo, C. Cavazzoni, S. De Gironcoli, P. Delugas, F. Ferrari Ruffino and others, "Quantum ESPRESSO toward the exascale," *The Journal of chemical physics,* vol. 152, p. 154105, 2020.

[193] M. A. Mäki-Jaskari and T. T. Rantala, "Band structure and optical parameters of the SnO 2 (110) surface," *Physical Review B,* vol. 64, p. 075407, 2001.

[194] J. M. Themlin, R. Sporken, J. Darville, R. Caudano, J. M. Gilles and R. L. Johnson, "Resonant-photoemission study of SnO 2: cationic origin of the defect band-gap states," *Physical Review B,* vol. 42, p. 11914, 1990.

[195] N. Barsan, M. Schweizer-Berberich and W. Göpel, "Fundamental and practical aspects in the design of nanoscaled SnO2 gas sensors: a status report," *Fresenius' journal of analytical chemistry,* vol. 365, p. 287–304, 1999.

[196] D. E. Williams, "Semiconducting oxides as gas-sensitive resistors," *Sensors and Actuators B: Chemical,* vol. 57, p. 1–16, 1999.

[197] J. Oviedo and M. J. Gillan, "First-principles study of the interaction of oxygen with the SnO2 (1 1 0) surface," *Surface Science,* vol. 490, p. 221–236, 2001.

[198] J. P. Joly, L. Gonzalez-Cruz and Y. Arnaud, "Désorption à température programmée de l'oxygène labile de SnO2," *Bulletin de la Société chimique de France,* p. 11–17, 1986.

[199] D. F. Cox, T. B. Fryberger and S. Semancik, "Oxygen vacancies and defect electronic states on the SnO 2 (110)-1× 1 surface," *Physical Review B,* vol. 38, p. 2072, 1988.

[200] I. Manassidis, J. Goniakowski, L. N. Kantorovich and M. J. Gillan, "The structure of the stoichiometric and reduced SnO2 (110) surface," *Surface Science,* vol. 339, p. 258–271, 1995.

[201] Y. Zhang, T.-T. Tang, C. Girit, Z. Hao, M. C. Martin, A. Zettl, M. F. Crommie, Y. R. Shen and F. Wang, "Direct observation of a widely tunable bandgap in bilayer graphene," *Nature,* vol. 459, p. 820–823, 2009.

[202] C. N. R. Rao, H. R. Matte and K. S. Subrahmanyam, "Synthesis and selected properties of graphene and graphene mimics," *Accounts of chemical research,* vol. 46, p. 149–159, 2013.

[203] W. Li, B. Chen, C. Meng, W. Fang, Y. Xiao, X. Li, Z. Hu, Y. Xu, L. Tong, H. Wang and others, "Ultrafast all-optical graphene modulator," *Nano letters,* vol. 14, p. 955–959, 2014.

[204] L. Li, Y. Yu, G. J. Ye, Q. Ge, X. Ou, H. Wu, D. Feng, X. H. Chen and Y. Zhang, "Black phosphorus field-effect transistors," *Nature nanotechnology,* vol. 9, p. 372, 2014.

[205] H. Liu, A. T. Neal, Z. Zhu, Z. Luo, X. Xu, D. Tománek and P. D. Ye, "Phosphorene: an unexplored 2D semiconductor with a high hole mobility," *ACS nano,* vol. 8, p. 4033–4041, 2014.

[206] L. Kou, C. Chen and S. C. Smith, "Phosphorene: fabrication, properties, and applications," *The journal of physical chemistry letters,* vol. 6, p. 2794–2805, 2015.

[207] T. Hu and J. Hong, "First-principles study of metal adatom adsorption on black phosphorene," *The Journal of Physical Chemistry C,* vol. 119, p. 8199–8207, 2015.

[208] J. Zhang, Y. Hong, M. Liu, Y. Yue, Q. Xiong and G. Lorenzini, "Molecular dynamics simulation of the interfacial thermal resistance between phosphorene and silicon substrate," *International Journal of Heat and Mass Transfer,* vol. 104, p. 871–877, 2017.

[209] X. Chen, Y. Wu, Z. Wu, Y. Han, S. Xu, L. Wang, W. Ye, T. Han, Y. He, Y. Cai and others, "High-quality sandwiched black phosphorus heterostructure and its quantum oscillations," *Nature communications,* vol. 6, p. 1–6, 2015.

[210] M. Lalitha, Y. Nataraj and S. Lakshmipathi, "Calcium decorated and doped phosphorene for gas adsorption," *Applied Surface Science,* vol. 377, p. 311–323, 2016.

[211] Q.-F. Li, X. G. Wan, C.-G. Duan and J.-L. Kuo, "Theoretical prediction of hydrogen storage on Li-decorated monolayer black phosphorus," *Journal of Physics D: Applied Physics,* vol. 47, p. 465302, 2014.

[212] M. Caporali, M. Serrano-Ruiz, F. Telesio, S. Heun, A. Verdini, A. Cossaro, M. Dalmiglio, A. Goldoni and M. Peruzzini, "Enhanced ambient stability of exfoliated black phosphorus by passivation with nickel nanoparticles," *Nanotechnology,* vol. 31, p. 275708, 2020.

[213] M. Valt, M. Caporali, B. Fabbri, A. Gaiardo, C. Malagù, M. Serrano-Ruiz, M. Peruzzini and V. Guidi, "Nickel-Decorated Black Phosphorus for Room Temperature NO2 detection," in *ECS Meeting Abstracts*, 2020.

[214] C. Maria, M. Valt, B. Fabbri, A. Gaiardo, C. Malagu, S.-R. Manuel, V. Guidi, P. Maurizio and others, "Nickel-decorated black phosphorus for sub-ppm NO2 detection at room temperature," in *The 8th GOSPEL Workshop. Gas sensors based on semiconducting metal oxides: basic understanding & application fields*, 2019.

[215] J. Klimeš, D. R. Bowler and A. Michaelides, "Van der Waals density functionals applied to solids," *Physical Review B,* vol. 83, p. 195131, 2011.

[216] J. Klimeš, D. R. Bowler and A. Michaelides, "Chemical accuracy for the van der Waals density functional," *Journal of Physics: Condensed Matter,* vol. 22, p. 022201, 2009.

[217] S. Lange, P. Schmidt and T. Nilges, "Au3SnP7@ black phosphorus: an easy access to black phosphorus," *Inorganic chemistry,* vol. 46, p. 4028–4035, 2007.

[218] Q. Wei and X. Peng, "Superior mechanical flexibility of phosphorene and few-layer black phosphorus," *Applied Physics Letters,* vol. 104, p. 251915, 2014.

[219] J. Qiao, X. Kong, Z.-X. Hu, F. Yang and W. Ji, "High-mobility transport anisotropy and linear dichroism in few-layer black phosphorus," *Nature communications,* vol. 5, p. 1–7, 2014.

[220] Y. Cai, G. Zhang and Y.-W. Zhang, "Layer-dependent band alignment and work function of few-layer phosphorene," *Scientific reports,* vol. 4, p. 1–6, 2014.

[221] Q. Zhou, Q. Chen, Y. Tong and J. Wang, "Light-induced ambient degradation of few-layer black phosphorus: mechanism and protection," *Angewandte Chemie International Edition,* vol. 55, p. 11437–11441, 2016.